Stephen F. Austin State University

SFA ScholarWorks

Summer 8-4-2022

GEOCHEMICAL CHARACTERIZATION OF THE BONE SPRING FORMATION, DELAWARE BASIN, USING CHEMOSTRATIGRAPHY AND INTEGRATED PETROPHYSICS

David Tonner
davidtonner@hotmail.com

GEOCHEMICAL CHARACTERIZATION OF THE BONE SPRING FORMATION, DELAWARE BASIN, USING CHEMOSTRATIGRAPHY AND INTEGRATED PETROPHYSICS

GEOCHEMICAL CHARACTERIZATION OF
THE BONE SPRING FORMATION, DELAWARE BASIN, USING CHEMOSTRATIGRAPHY
AND INTEGRATED PETROPHYSICS

By

DAVID J. TONNER, Bachelor of Science

Presented to the Faculty of the Graduate School of

Stephen F. Austin State University

In Partial Fulfillment

Of the Requirements

For the Degree of Master of Science, Geology

STEPHEN F. AUSTIN STATE UNIVERSITY

August 2022

GEOCHEMICAL CHARACTERIZATION OF
THE BONE SPRING FORMATION, DELAWARE BASIN, USING CHEMOSTRATIGRAPHY
AND INTEGRATED PETROPHYSICS

By

DAVID J. TONNER, Bachelor of Science

APPROVED:

_____
Dr. Julie Bloxson, Thesis Director

_____
Dr. Liane M. Stevens, Committee Member

_____
Dr. Robert Friedfeld, Committee Member

_____
Dr. Mindy Faulkner, Committee Member

_____
Freddie Avant, Ph.D.
Interim Dean of Research and Graduate Studies

ABSTRACT

The Delaware Basin forms part of West Texas's and New Mexico's famous petroleum-generating Permian Basin. The Bone Spring Formation is a prolific hydrocarbon producer within this basin, creating one of the world's richest oil shales. This formation has lithological sequences that are characterized by repeating carbonate and siliciclastic intervals of a third-order cycle which can largely be correlated to highstand and lowstand systems tracts, respectively. Lithological complexity and facies change are manifested by debris flows, turbidites, and slumps. In addition to glacio-eustasy, both tectonism and broader Milankovitch cycles have influenced the depositional history.

Previous investigations have utilized cores and wireline logs to provide high-resolution chemo-facies segregation, which can be correlated with reservoir and rock properties; however,core and wireline logs are sporadically collected, whereas drill cuttings are available from most wells. For this study, XRF elemental data derived from drill cuttings collected at 30 – 60ft (9 – 18m) intervals have been compared to wireline well logs. XRF measurements were categorized using hierarchical cluster and principal component analysis based on chemical facies. Chemostratigraphic units and packages were applied to generate cross-sections and facies maps to understand depositional cyclicity, terrigenous influence, grain size,

mineralogy, organic content and rock property distribution. These data sets can be used to high-grade acreage for resource identification and storage to optimize drilling performance, completion designs and as a geosteering input.

ACKNOWLEDGMENTS

TABLE OF CONTENTS

TABLE OF FIGURES

LIST OF TABLES

LIST OF EQUATIONS

(1.) INTRODUCTION

The Greater Permian Basin is a global leader in hydrocarbon production, with estimated remaining proven reserves in excess of 5 billion barrels of oil and 19.1 trillion cubic feet of natural gas, making it one of the largest hydrocarbon-producing basins in the United States and the world (EIA, 2017). It includes the Delaware Basin and Diablo platform to the west, the Central Basin Platform to the east, and the rocks of the Ancestral Rocky Mountains and the Northwest Shelf to the north-northwest (Figure 1.) (Hatcher et al., 1989). A thick section of up to 4,000 feet (1,000 m) of siliciclastic, carbonate, and evaporite sediments accumulated during the Pennsylvanian in a deep-water depositional setting, depositing the Leonardian Bone Spring Formation from 268-283 Ma, (Ewing, 1991, 2014). This formation is one of the most prolific hydrocarbon-producing unconventional reservoirs in the basin, and prior to 2010 was a prolific conventional reservoir in the sandstone intervals, consisting of heterogenous interbedded carbonates, mudstones, and sandstones, (Carr, 2019). Eustatic and tectonic controls over Permian Basin evolution have resulted in the complex lithologies and structure of the Bone Spring Formation. This stratigraphic interval is characterized by a repeating third-order cycle of carbonate and siliciclastic intervals, which can largely be correlated to highstand and lowstand systems tracts, respectively (Carr, 2019). Furthermore, extensive debris flows caused by tectonic pulses and/or high frequency sea level fluctuations are found

throughout the basin, which resulted in increased vertical and lateral facies variability

(Loucks and Ruppel, 2007; Driskell, 2018). Establishing relationships between the

depositional cyclicity, terrigenous influence, grain size, mineralogy, and rock properties,

and their geochemical elemental facies could provide a greater understanding of both the

genesis and occurrence of these formations.
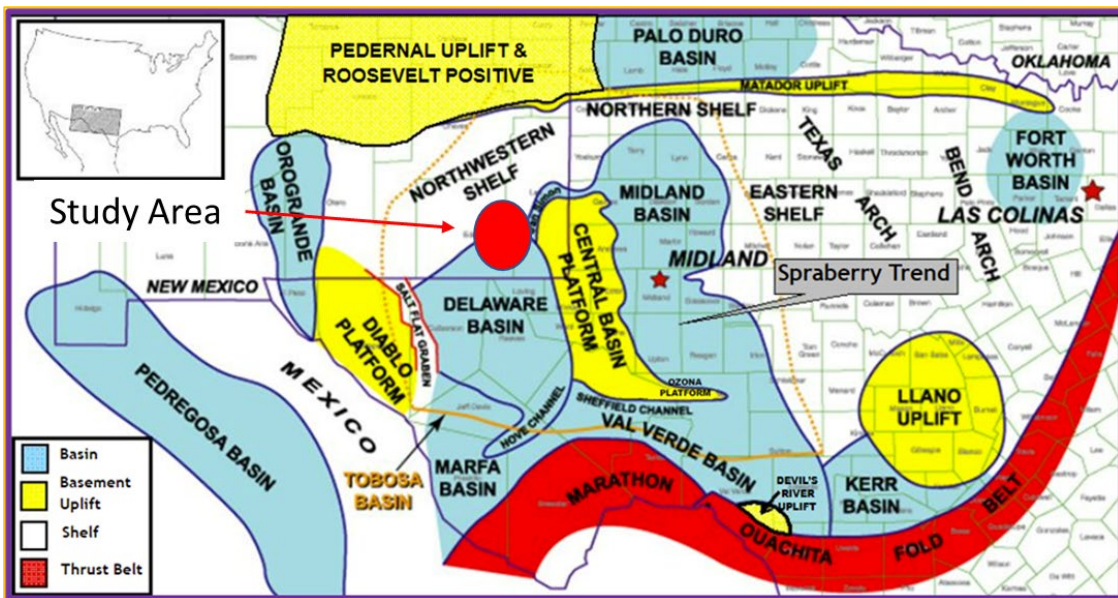
Figure 1, Regional structural features in West Texas and New Mexico. The study area is marked by the red dot. The Greater Permian Basin includes the Delaware Basin, Central Basin Platform, Midland Basin and Val Verde Basin. The study area is on the northern edge of the Delaware Basin. Modified from Pioneer Natural Resources (2013).

One method for analysis of mudstones is chemostratigraphy. Chemostratigraphy is a

reservoir correlation technique utilizing geochemical data for characterization and

correlation of sedimentary rocks. It is widely used in paleoclimatology and

paleoceanography (Rothwell and Croudace, 2015a, 2015b; Algeo and Maynard, 2004;

2

Ratcliffe et al., 2004; Pearce et al., 1999), and has proven well suited to the study of fine-grained mudrock systems and tight reservoirs Craigie, 2021). On first appearance, mudstones can appear to be homogenous; however, they can contain significant geochemical variability that is as a result of depositional influences (Figure 2.) (Algeo and Maynard, 2004). Chemical proxies have been developed regarding several sediment properties including source, clay content, dolomitization, anoxia, organic richness, and terrigenous input (Algeo and Maynard, 2004; Ratcliffe et al., 2004; Pearce et al., 1999;
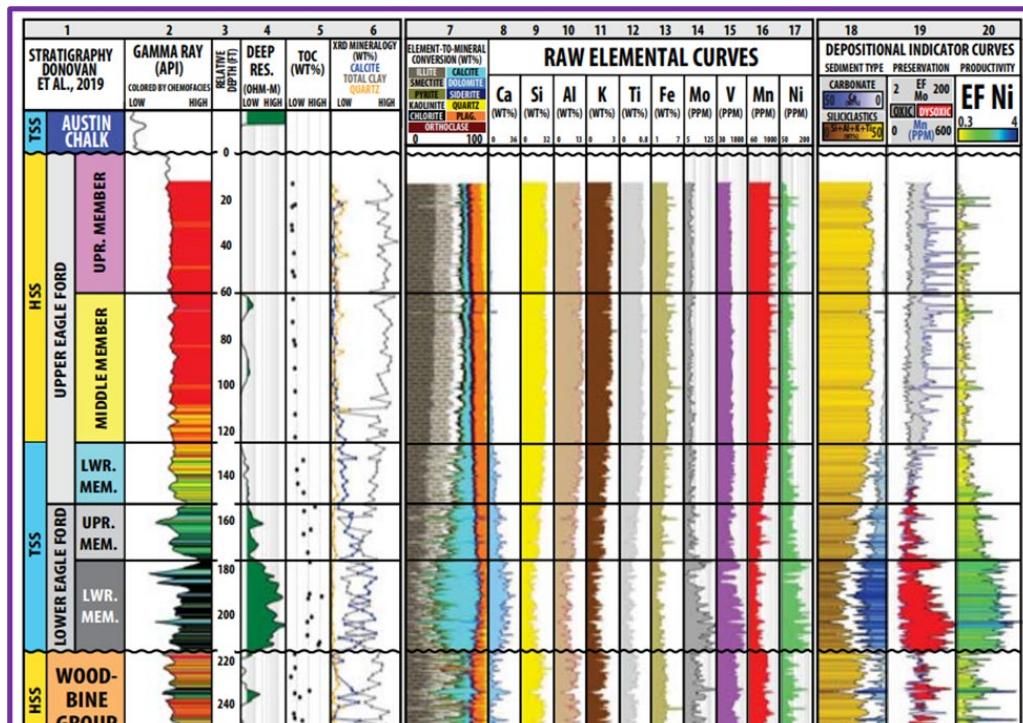
Figure 2, Geochemical data from the Buda, Woodbine Group, and Eagle Ford Formation. The elemental data can be interpreted as minerals, either by themselves or as ratios with other elements. In conjunction with X-ray diffraction measurements (XRD) as a calibration for minerals present. Oftentimes, the elemental data is also correlated to TOC to aid in interpretation of depositional setting. These can then be used to infer sediment type (Track 18), preservation potential (oxic vs. dysoxic conditions; Track 19), and productivity (EF Ni; Track 20). Track 18 consisting of carbonate vs. siliciclastics is a key signal in understanding Leonardian Permian depositional systems in this study. From Meyers (2019).

Tribovillard, 2006, 2010; Ratcliffe et al., 2010; Wright et al., 2010; Turner et al., 2015; Driskill et al., 2018). For example, while the increased solubility of redox-sensitive trace metals in oxic environments leads to trace metal depletion, in oxygen-deficient environments trace metals are enriched due to their lower solubility (Driskill et al., 2018). The influx of nutrient-rich waters (enriched in elements such as phosphorous and copper) promotes primary production, while subsequent anoxia encourages the preservation of organic matter (Brumsack, 1989). Furthermore, correlations have been established between certain trace metals, such as Ni, As, Co, Cu, Fe, Mo, Ni, S, Se, and Zn, with total organic carbon (TOC) in the Wolfcamp and Bone Spring formations (Driskill et al., 2018). From Driskill et al.'s work, uranium does not correlate well with TOC in these formations, which is often the case with "typical" organic rich shales such as the Devonian Marcellus Shale (Driskill et al., 2018). This can lead to inaccurate TOC estimations from the spectral gamma ray or traditional gamma ray logs. Overall, these fundamental principles of chemical elements as proxies for understanding evolving geologic conditions can be used to determine event extent , timing and spatial extent to expand upon a generalized model for basin mudstone deposition (Cortez, 2012).

Elemental data is used to understand depositional cyclicity (sea level changes), terrigenous influence, grain size, mineralogy, and rock mechanical properties. The work of Driskell et al. (2018) and Peng et al. (2022) utilizing core data illustrates the potential insights that can be obtained. Driskill et al. (2018) used core, log, and elemental data obtained via X-ray fluorescence (XRF) to demonstrate how silica/aluminum (Si/Al),

zirconium/aluminum (Zr/Al), and titanium/aluminum (Ti/Al) ratios identified fining upwards Bouma turbidite sequences in the 3rd Bone Spring and Wolfcamp A formations. Si is a proxy for quartz and Al is a proxy for clay mineral content. A decrease in the Si/Al ratio occurs in upward fining sequences, indicating a turbidite sequence. Their work was able to determine grain size using these elemental proxies, showcasing the heterogeneity of these formations throughout the region. Zr, Hf, Ti, Ta, Nb, Cr, Y, Th are considered high field strength detrital elements, their distributions being largely unaffected by post depositional weathering/diagenesis. For this reasonalone, they tend to be utilized in isolation, or in the form of ratios, to place chemostratigraphic boundaries (Craigie, 2018).

Elemental data derived from core have been used to establish relationships with lithological facies as well (Larson, 2022). Principal Component Analysis and K Means Clustering were employed on the Wolfcamp Formation to develop statistical chemical facies that were then correlated with lithofacies to better predict reservoir quality. Stolz et al. (2015) also demonstrated a relationship between petrophysical properties and lithofacies in the bone spring and avalon formations overlying the Wolfcamp. Carbonate facies were determined by Ca and Mg concentrations, which negatively correlated with porosity and permeability measurements. The Ca and Mg concentrations could be taken as proxies for porosity and permeability rather than taking time consuming and expensive measurements. Ca and Mg, therefore, can be used to predict reservoir quality in these formations (Figure 3.). Walker (2021) worked on outcrops in the Guadelupe mountains and linked chemical facies to lithofacies and depositional environments using in situ XRF

measurements.

However, previous work, including that mentioned above, has primarily used core for chemostratigraphy studies (Driskill et al., 2018, Larson et al., 2021). While core can provide a complete picture of a formation in the subsurface, they are expensive, proprietary, and oftentimes widely spatially distributed. Drill cuttings and wireline logs are prolific across basins and can provide better spatial resolution across a region, although at the expense of depth resolution. Drill cuttings are often taken every 30 to 120 ft (9 to 36 m), rather than continuously, like core (Tonner, 2018). Well logs can have a depth resolution down to 2 ft (60 cm) (Nance and Rowe, 2010) sometimes even less, depending on the age and type of tool. Few chemostratigraphy studies have been conducted using cuttings because of the low depth resolution; however, the potential exists to "fill in the gaps" where cores are unavailable.

This study utilized cuttings and well logs to create a subsurface model of the Bone Spring Formation to determine depositional environmental conditions in the northern Delaware Basin. These results were then compared to results from previous core studies to determine if cuttings are a viable option for chemostratigraphy studies. This will provide a foundation for the usefulness of cuttings when core is unavailable or scarce in a region. The data sets is uded to determine sequence stratigraphy and depositional cycles, whether eustatic or tectonic, within the Bone Spring Formation in Lea County, eastern New Mexico. Establishing relationships between drill cuttings and wireline data can aid in upscaling and application of data models across many wells and thus create a

better understanding of the subsurface as it relates to depositional cyclicity, terrigenous

influence, grain size, mineralogy, and rock properties.

2. STUDY OBJECTIVES

The objectives for this study are listed below:

1. Describe the changes in depositional environments throughout the Bone Spring Formation, including the Avalon Formation and Big Lime using XRF data on cuttings in Lea County, NM.

2. Assign chemofacies to the ten wells in the study area based upon Principal Component Analysis (PCA) and Hierarchical Cluster Analysis (HCA) cluster assignments to show periods of similar depositional conditions across the region.

3. Link chemofacies to lithofacies to improve understanding of the influence of glacio-eustasy and tectonic events in the rock formation.

4. Showcase the utility of cuttings data for chemostratigraphy studies by comparing this study to previous core studies. Cuttings have a lower resolution (typically 9.1 m (30 ft) sampling intervals), compared to core or outcrop where an entire section could potentially be observed.

5. Calculate reservoir properties from the cuttings XRF data, including the Brittleness Index, Gamma Ray log, TOC and V_{clay}.

6. Compare the calculated reservoir properties to petrophysical analyses to see if correlations exist between either widely used petrophysical calculations or well logs. This would allow for easy interpretation of chemofacies once correlations are established.

7. Address if chemostratigraphy can identify formations on a well bore lateral and can be used for geosteerig purposes.

3. GEOLOGIC HISTORY

The Permian Basin, also called the West Texas Super Basin, covers more than 75,000 mi^2, spanning west Texas and southern New Mexico (U.S. Energy Information Administration, 2019). It is bounded by the Ouachita-Marathon orogenic belt to the south, the Diablo Platform to the west, the Eastern Shelf to the east, and the Northwest Shelf and Matador Arch to the north, with several sub-basins and platforms within the basin itself (Ewing, 1991; Ewing, 2014; Ewing, 2016; Ewing, 2019) (Figure 1.). The basin has produced 28.9 billion barrels (bbl.) of oil and 203 Trillion Cubic Ft (TcF) of gas since the 1920's (63 billion barrles of oil equivalent (BOE), (1920–2019). The US Geological Survey and the Texas Bureau of Economic Geology estimate that this super basin has 120–137 billion BOE in place (Fairhurst, 2021).

The West Texas Super Basin is a complex Paleozoic basin built on a varied Proterozoic crust. Initial Neoproterozoic and Cambrian rifting were followed by regional subsidence, later forming the Tabosa Basin (Figure 3.) in which deposition began in the Middle Ordovician and continued into the Devonian. Early Paleozoic Tabosa Basin subsidence terminated during the Mississippian orogenic uplift derived from the convergence of the Laurentian and Gondwanan plates. (Galley, 1958; Ewing, 2016). This is known as the Ouachcita Orogeny (Figure 4.). This event, known as the Ouchita orogeny, resulted in the closure of the Rheic Ocean, the creation of the Pangea supercontinent

(Nance, 2008), and the development of the orogen as the southern edge of the Laurentia plate was subducted beneath a northward-advancing Gondwanan (South American side) continental-margin arc. Large-scale faulting and folding accompanied later stage tectonic evolution during the Late Mississippian subsidence. Tectonic and structural development was controlled by compression related to the Ancestral Rocky Mountains and Ouachita-Marathon orogenic events. The Ouachita-Marathon tectonic event ended in the Wolfcampian (early Permian) (Figure 6.). Subsidence continued to the end of the Ochoan. Periodic subsidence during the Mesozoic was likely caused by Laramide deformation in the Rocky Mountains. Cenozoic Laramide western uplift tilted the basin towards the east (Fairhurst, 2021).

During the Wolfcampian of the Permian (299-280 Ma), shallow carbonate shelves accumulated on the edges of the basin. Late Paleozoic tectonism led to high amounts of subsidence and compressional stress uplifting the platforms, leading to increased turbidite deposition of clastic and carbonate sediment on the slope (Adams, 1965). High sedimentation rates during the Permian (265-230 Ma) filled the basin with deltaic siliciclastics and extensive reef carbonate ringed the basin and evaporite shelves (Figure 5.). Marine transgression led to massive deposits of the overlying fine-grained siliciclastics into the basin (Hill, 1972) (Figure 6.).
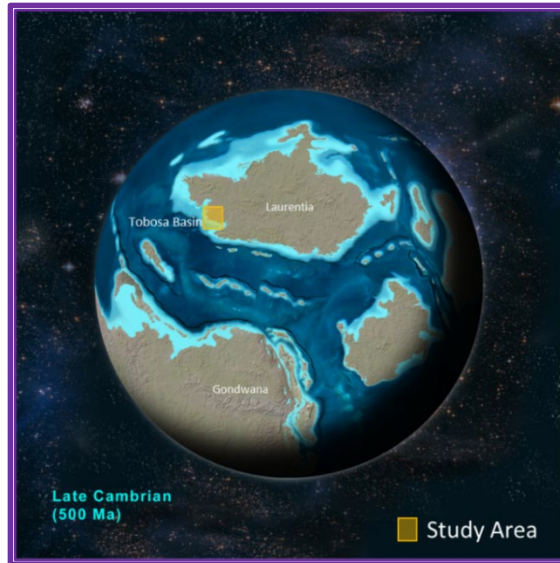
Figure 3, During the Cambrian through the Mississippian, carbonate and clastic sediments were deposited in a broad marine basin, creating the Tobosa Basin. Modified from Blakey (2016).
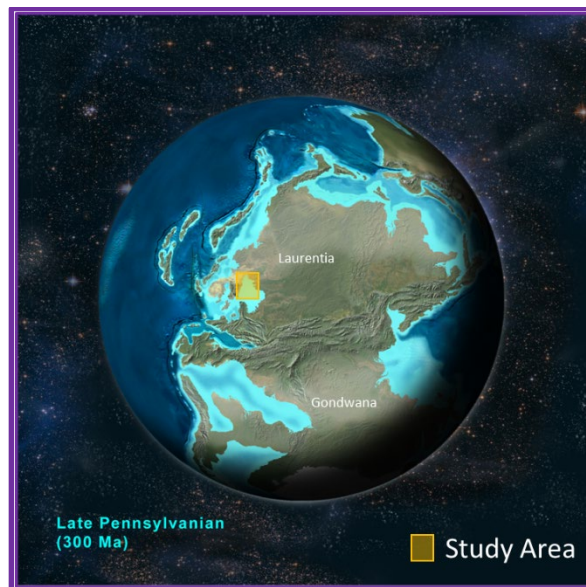
Figure 4, The Ouachita rogeny occurred as Laurentia collided with South America from the Early Pennsylvanian through the Early Permian. This orogeny caused basin differentiation into several deep basins surrounded by shallow shelves. Modified from Blakey (2016).
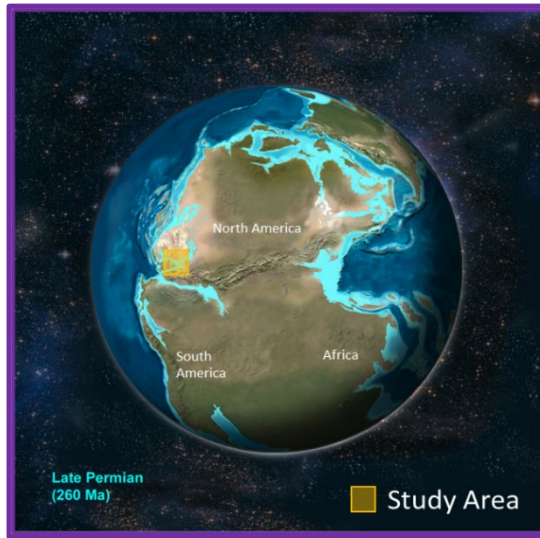
Figure 5,The collision of Laurentia and Gondwana resulted in the formation of the Pangea supercontinent. Large volume Sediment deposition was initiated when the basin became structurally stable. Large volumes of Permian clastic sediments were deposited in the deeper part of the basin and carbonates were deposited on the shelves. Modified from Blakey (2016).
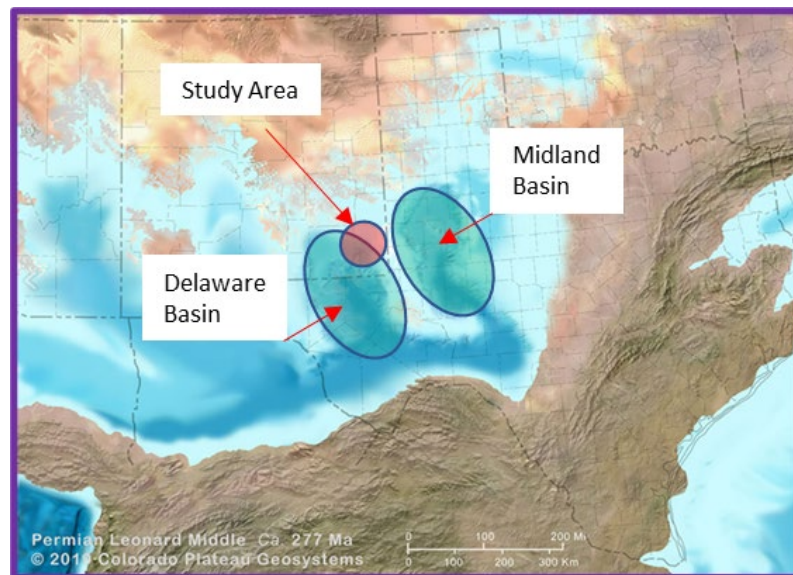
Figure 6, Leonardian depositional environments across the region. Tropical marine depositional environment existed with fluctuating sea levels. The Delaware Basin and Midland Basin are circled in blue, and the study area is highlighted in red. From Blakey (2020).

4. STRATIGRAPHIC FRAMEWORK

4.1 General Stratigraphy and Lithology

The Bone Spring Formation unconformably underlies the Brushy Canyon formation consisting of silts, carbonates, and shale that were deposited during cyclical sea level changes, with an overall gradational transgression. The Bone Spring is often informally divided into eight members, in ascending order: 3rd Bone Spring sand, 3rd Bone Spring carbonate, 2nd Bone Spring sand, 2nd Bone Spring Carbonate, 1st Bone Spring sand, 1st Bone Spring carbonate, Avalon sandstone, Bone Spring lime (Figure 7.). This Leonardian series is present throughout the Delaware Basin and is laterally equivalent to the Wichita, Abo-Yeso and Clearfork formations on the Central Basin Platform, and the Dean and Spraberry formations in the Midland Basin (EIA, 2019). Together the Bone Spring and Avalon formations average in thickness from 2,500 feet to 3,500 feet, with the thickest region occurring in the eastern portion of the Delaware Basin. The Bone Spring formation represents the downdip equivalent to thick shelf and shelf-margin carbonates that rimmed the Delaware basin during deposition of Leonardian strata (Mazzullo, 1991). Across the northern Delaware Basin, the Leonardian Bones Spring Formation represents a general shelf-to-basin relationship, (Montogmery, 1997). Although labeled as "sands," the 1st, 2nd and 3rd Bone Springs sands are mislabeled, these are mudstones with varying degrees of carbonate, siliceous and argillaceous composition.

The Bone Spring Formation is a repeated cycle of basal siliciclastics capped by carbonates (Figure 13.) (Carr, 2019; Nance and Hamlin, 2020), creating the 1st, 2nd, and 3rd Bone Spring cycles. The low stand siliciclastics were deposited in laterally continuous submarine fan systems on the basin floor (Nance and Hamlin, 2020), while the carbonate members were deposited during high stands. The carbonates consist of three types of facies. The spiculitic limestone facies consists of carbonaceous wackestone and mudstones, with sponge spicules found throughout, deposited in a deep basinal setting, and are the main carbonate in the 1st Bone Spring carbonate (Montgomery, 1997). The dolomitized breccia facies consists of several facies within the package. Varying sizes of angular grains create packstone and wackestone that have been altered. The clasts within these breccias consist of laminated siltstones, cross-bedded peloidal packstone and grainstone, bryozoan-rich bound stones, and skeletal debris. These are thought to have been derived from the shelf through upper slope, deposited during submarine debris flows that exhibit sharp erosional contacts with rip up clasts (Bienvenour, 2019). The dolomitized bioclast packstone facies consists of bioclast-pelloid packstone, with occasional wackestone and grainstone. The grains consist of skeletal debris (crinoids, bivalves, sponges, etc.). This facies is the main constituent of the 2nd Bone Spring carbonate. Generally, the carbonates are composed of dark and dense carbonaceous wackestone, and mudstone. These mudstones are an important source rock (Montgomery, 1997). Carbonate-dominated Bone Spring units are typically thickest at the basin margins, and show subtle thickening in structural lows that are located in basinal

14

positions. The very thick, basinward thinning fan pattern emanating from the southern part of the NW Shelf suggests that highstand carbonates were shed into the basin episodically due to autocyclic and catastrophic processes by sediment current flows (Carr, 2019). The 1st Bone Spring Carbonate consists of the 1st Bone Spring Lime, The Avalon, and the Big Lime. The Avalon is often divided further into three informal intervals: Lower Avalon, Middle Avalon, and Upper Avalon. The Lower and Upper Avalon are generally the mudstone-rich intervals separated by the more carbonate-rich Middle Avalon. The Avalon is a fourth low stand fan system productive in the more siliciclastic northern basin (Fairhurst, 2021). The Avalon has a thickness in excess of 150ft, porosity that ranges from 4-17%, and TOC ranging from 4-8% in the shale intervals

Siliciclastic intervals in the Bone Spring Formation consist of three general types of facies: argillaceous facies, siliceous facies and carbonate facies. Sand strata in the Bone Spring Formation were deposited as submarine fans. The sand intervals of the Bone Spring are composed of dark, thinly bedded, calcareous shales and siltstones. Overall, the Bone Spring Formation has porosities ranging from 4.5 to 16%, and an estimated TOC of 1 to 8 %.

The Big Lime overlying the Avalon is a carbonate mudstone sequence which lies unconformably beneath the Brushy Canyon clastics. As described by (Walker, 2021), the Bone Spring Fm. upper slope as composed predominantly of fine-grained carbonate hemipelagites and sediment gravity flows containing a high biogenic silica content (i.e., chert). Interbedded within the carbonate slope facies at various scales are detrital

terrigenous hemipelagic and sediment gravity flow deposits, carbonate mass-transport deposits, and carbonate submarine channel deposits.

Work done by Wiley (2021), mapped outcrops of the Bone Spring Formation in the Guadalupe Mountains of West Texas, developed an eight facies classification scheme and, in addition, mapped the facies to chemofacies using XRF measurements, (Figure 8.). The principal objective was to link geomorphology and slope to lithofacies and chemofacies. The following facies were identified:

A. Facies 1 thin-bedded laminated lime mudstone with pencil-thin marking ripples. Thin section of facies 1 is predominantly lime mudstone, but detrital quartz grains are present. (Figure 9A.)

B. Facies 2, thin to thick bedded deformed lime mudstone with lines indicating deformation. Thin section of Facies 2 with deformation-induced calcite-cemented fractures with background facies identical to Facies 1. (Figure 9B.)

C. Facies 3, thick-bedded bioclastic lime wackestone to packstone. Thin section of Facies 3 shows an increase in mud content to the top interpreted as a possible turbidity current. (Figure 9C.)

D. Facies 4, interbedded lime mudstone and bioclastic packstone with interbedded packstone indicated. Thin section shows interbedded packstone beds with calcite cementation and lenticular to continuous nature. (Figure 9D.)

E. Facies 5 thick-bedded normal-graded bioclastic lime packstone to grainstone. Normal grading shown with finger placed on basal coarse-grain deposit. Thin section

shows bryozoan (by), brachiopods (ba), and undifferentiated carbonate allochems with chert cement.(Figure 9E.)

F. Facies 6 thin-bedded laminated bioclastic quartz siltstone. Note different color and weathering patterns to Facies 1. Thin section shows noticeably higher detrital quartz present in comparison to Facies 1.(Figure 9F.)

G. Facies 7 thin-bedded laminated quartz lime mudstone. Interbedded with Facies 6 showing different weathering patterns. Note brown color in comparison to Facies 1. Thin section of Facies 7 with detrital quartz content less than Facies 6 but greater than Facies 1.(Figure 9G.)

H. Facies 8, thick bedded bioclastic lime packstone to grainstone. Thin section of Facies 8 reveals bryozoan (by), sponge spicules (sp), rugose corals (co), brachiopods (ba), and unidentified carbonate material.(Figure 9H.).

Figure 7, Generalized stratigraphic chart of the Delaware Basin. Blue color represents a limestone formation, and yellow represents sandstone formations. Modified from Rupel (2020).
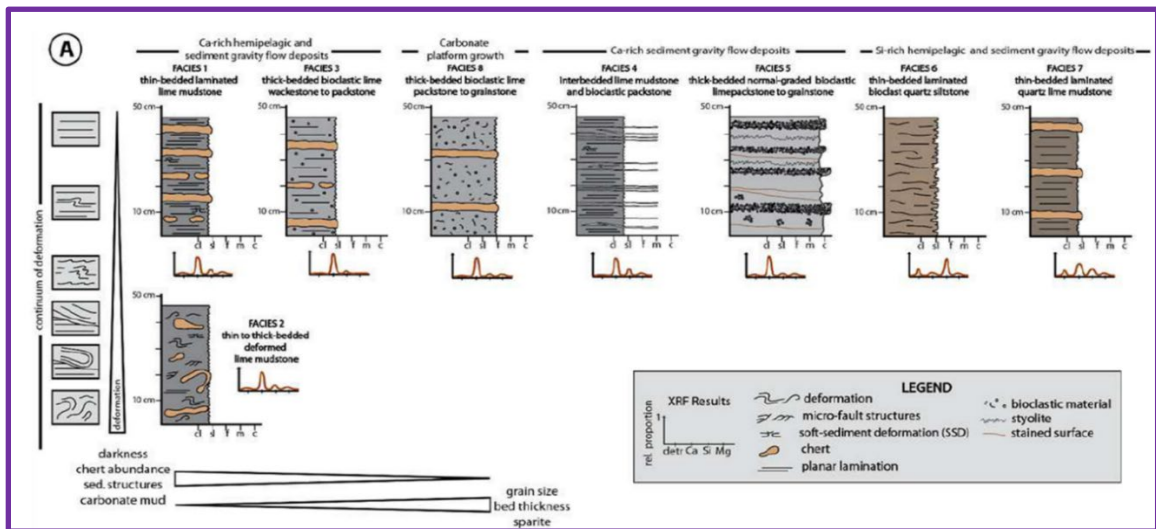
Figure 8, Facies Model based on outcrop study in the Guadalupe Mountains, West Texas. From Walker (2021).
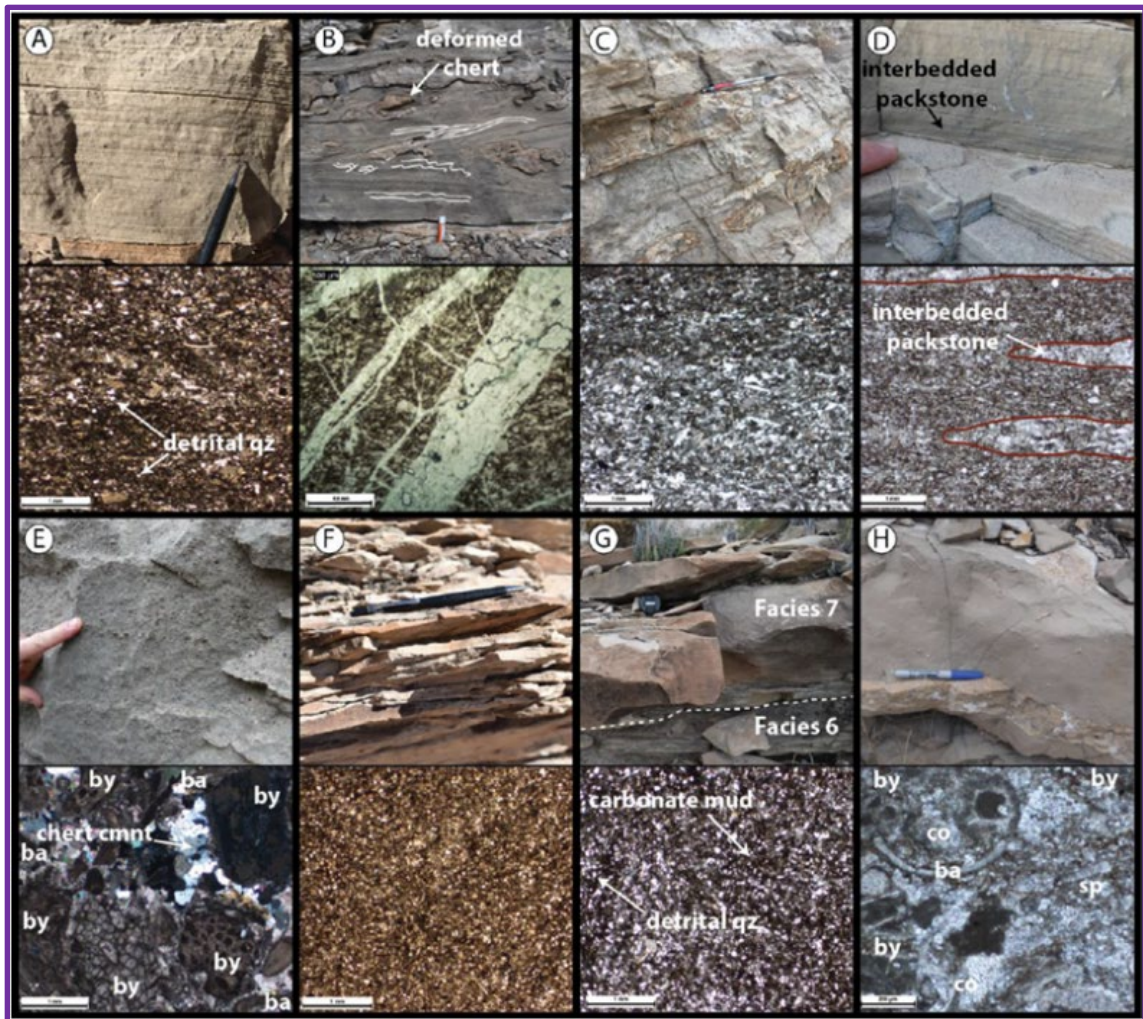
Figure 9, Photographs of outcrops and photomicrographs depicting the eight facies Facies pictures from outcrop (upper photo) and thin section (lower photo). A) Facies 1 is a thin-bedded laminated lime mudstone. The pencil is marking ripples. Detrital quartz grains are visible in thin section. B) Facies 2 is a thin to thick bedded deformed lime mudstone with form lines indicating deformation. Photomicrograph of Facies 2 with deformation-induced calcite-cemented fractures with background facies identical to Facies 1. C) Facies 3 is a thick-bedded bioclastic lime wackestone to packstone. Photomicrograph of Facies 3 shows an increase in mud content to the top interpreted as possible turbidity current. D) Facies 4 is an interbedded lime mudstone and bioclastic packstone with interbedded packstone indicated. Photomicrograph shows interbedded packstone beds with calcite cementation and lenticular to continuous nature. E) Facies 5 is a thick-bedded normal-graded bioclastic lime packstone to grainstone. Normal grading shown with finger placed on basal coarse-grain deposit. Thin section shows bryozoan (by), brachiopods (ba), and

19

undifferentiated carbonate allochems with chert cement. F) Facies 6 is a thin-bedded laminated bioclastic quartz siltstone. Note different color and weathering pattern to Facies 1. Thin section shows noticeably higher detrital quartz present in comparison to Facies. G) Facies 7 is a thin-bedded laminated quartz lime mudstone. Interbedded with Facies 6 showing different weathering pattern. Note brown color in comparison to Facies 1. Photomicrograph of Facies 7 with detrital quartz content less than Facies 6 but greater than Facies 1. H) Facies 8 is a thick bedded bioclastic lime packstone to grainstone. Photomicrograph of Facies 8 reveals bryozoan (by), sponge spicules (sp), rugose corals (co), brachiopods (ba), and unidentified carbonate material, (Walker 2021).

Bienvenour and Sonnenberg (2019) developed the following more detailed sub classifications that can be divided into nine discreet facies. Within each facies there are Argilaceous, calcareous and biogenic sub facies. Each facies has been described based on its formation. Ie turbiditic, hemipelagic and formed from debrites. Figure 10 depicts core photographs, thin section photomicrographs and XRD ternary diagrams for the Leonardian and Wolfcamp formations.

Table 1. Facies classification based on an integrated core and log study by Bienvenour and Sonnenberg (2019).

Facies #	Facies Name	Facies Group	Bulk Mineralogy	Common Facies Assemblage
1	Argillaceous Siliceous Mudstone	Siliceous Mudstone	Si > Ar > Ca	L.D. Turbidite / Hemipelagic / H.E.B.
2	Calcareous Siliceous Mudstone	Siliceous Mudstone	Si > Ca > Ar	L.D. Turbidite / H.E.B. / Hemipelagic
3	Biogenic Siliceous Mudstone	Siliceous Mudstone	Si > Ar > Ca	Hemepelagic
4	Argillaceous Siliceous Siltstone	Siltstone	Si > Ar > Ca	L.D. Turbidite
5	Calcareous Siliceous Siltstone	Siltstone	Si > Ca > Ar	H.E.B. / L.D. Turbidite
6	Siliceous Calcareous Siltstone	Siltstone	Ca > Si > Ar	H.E.B. / L.D. Turbidite / H.D. Turbidite
7	Skeletal Mud Dominated Wacke-Packstone	Carbonate	Ca > Si > Ar	Debrite / H.E.B. / H.D. Turbidite
8	Skeletal Grain Dominated Pack-Grainstone	Carbonate	Ca > Si > Ar	Debrite / H.D. Turbidite
9	Dolomitic Skeletal Packstone	Carbonate	Ca > Si > Ar	Debrite / H.D. Turbidite
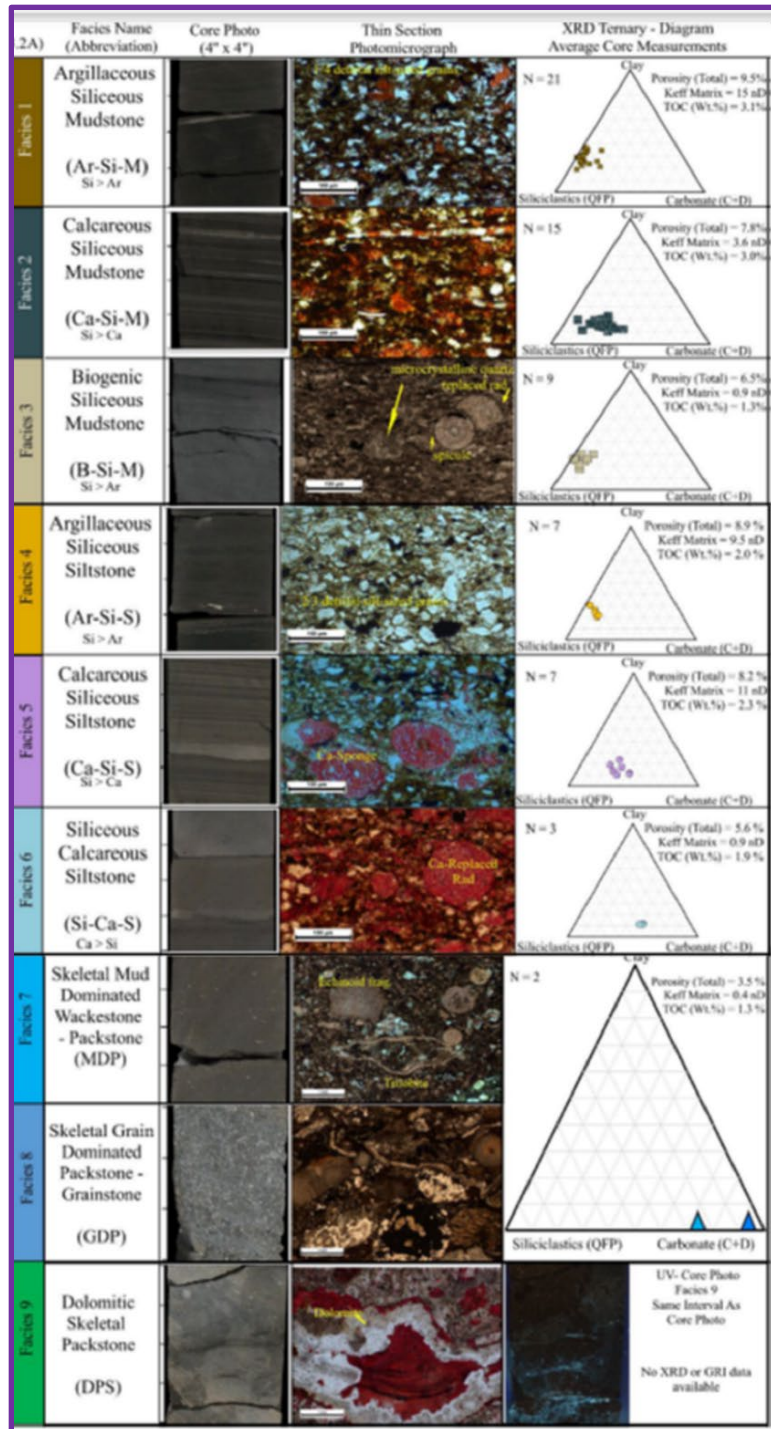
Figure 10, Core photographs, thin section photomicrographs and XRD ternary diagrams for the principal facies seen in the Leonardian Bone Spring and Wolfcamp Formations. From Bienvenour and Sonnenberg (2019).

A Depositional Model of the Delaware Basin during Leonardian Time was developed by

Loucks et al., 1985. Characteristic depositional processes of the time include carbonate

debris origination above the basin floor, and deposition of organic, pelagic siltstones and

mudstones out onto the basin floor. (Figure 11.).
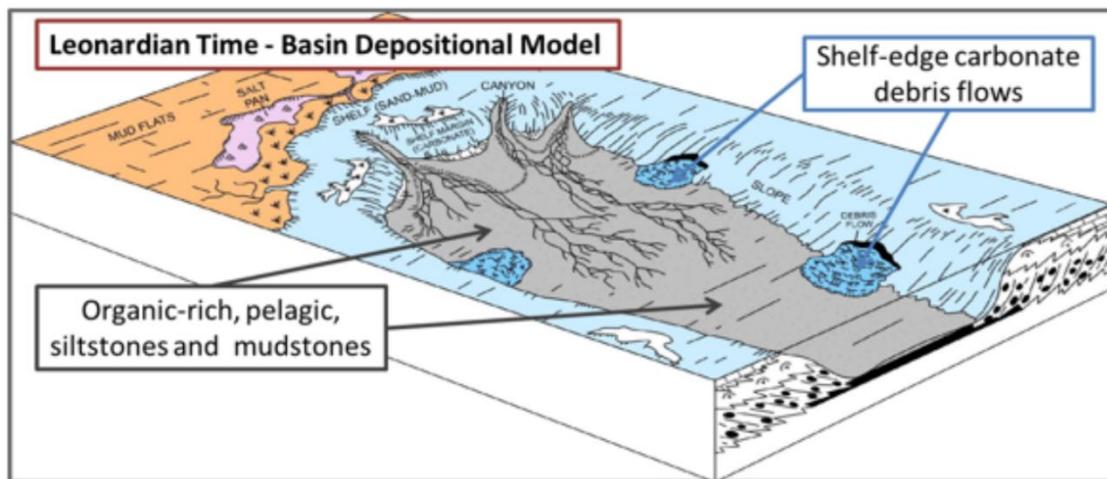
Figure 11, Depositional Model of the Delaware Basin during Leonardian Time. Characteristic depositional processes of the time include carbonate debris origination above the basin floor, and deposition of organic, pelagic siltstones and mudstones out onto the basin floor (Loucks et al., 1985).

4.2 Type Well Log

Well logs have historically identified the changes in facies in the Avalon, 1st, 2nd

and 3rd Bone Spring (Carr, 2019). The repeated cycles of carbonates, clastics, and

mudstones create cyclical patterns in well log data. The 1st Bone Spring carbonate

sequence and the Avalon carbonates are characterized by low gamma ray (< 40 API), high

photoelectric effect (PEF) (~4.7 barnes/electron) and resistivity values (~ 1000 ohm),

higher density readings (~2.65-2.8 g/cm^3), and an increase in sonic travel times (~100

usec/ft) compared to the siliciclastic intervals. In the sandstone, Hamlin and Baumgardner

(2012) utilized wireline logs to estimate the position and the contact of the facies in the

Midland Basin. Carr (2019) applied gamma ray (GR) vs. deep resistivity (Rd) cross plot

methodology to the Bone Spring BSPG in the Delaware Basin. He used a GR-Rd model and

created wireline facies curves for approximately 1800 wells where top picks and GR-Rd

log-curve suites were available. Carr observed that the base of Brushy Canyon/top of

BSPG was not difficult to pick in wireline logs, however the other boundaries of the

uppermost mapping units, "Cutoff" and "Avalon", as well as the top of the 1st Bone Spring

Lime, can be comparatively difficult to identify. Isopach maps by Carr (2019) indicate that

siliciclastic deposits are thickest in the basin center while carbonates are thickest at the

basin margins (Figure 12.).
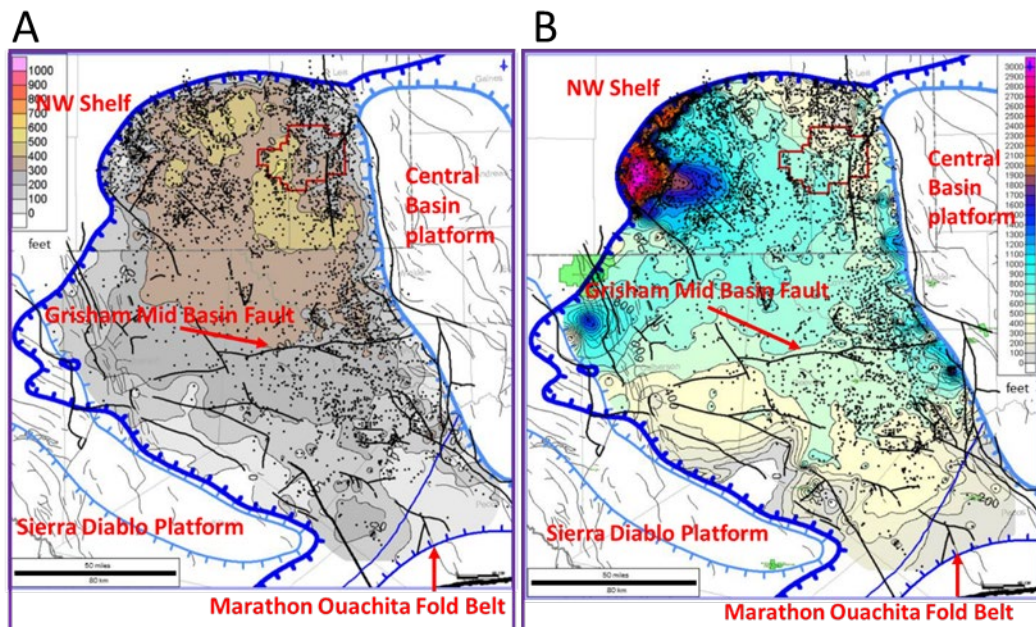
Figure 12, Gross interval isopach maps of the (A) 3rd Bone Spring sand and (B) 3rd Bone Spring carbonate with the unit basement faults in bold black from Ewing (1990). Siliciclastic-dominated Bone Spring units are typically thickest in basin-center positions with the carbonate's thickest on the rim. The thickest parts of the unit occur in the northern half of the basin, north of the east–west-striking Grisham fault (aka Mid-Basin fault), indicating that structure also influenced Bone Spring sedimentation. From Carr (2019).

Between the carbonate to the siliciclastic intervals in the study area, there is a slight increase in gamma ray (>50 API), a reduction in PEF (~2.4-2.6) and resistivity (20-200-ohm meters), and a decrease in density (2.4-2.5 g/cm^3) and sonic (~50usec/ft) values. This repeated carbonate highstand and siliciclastic lowstand sequence is important because the changes in chemical stratigraphy will be identified using XRF element geochemistry. (Figure 13 & Figure 14.).
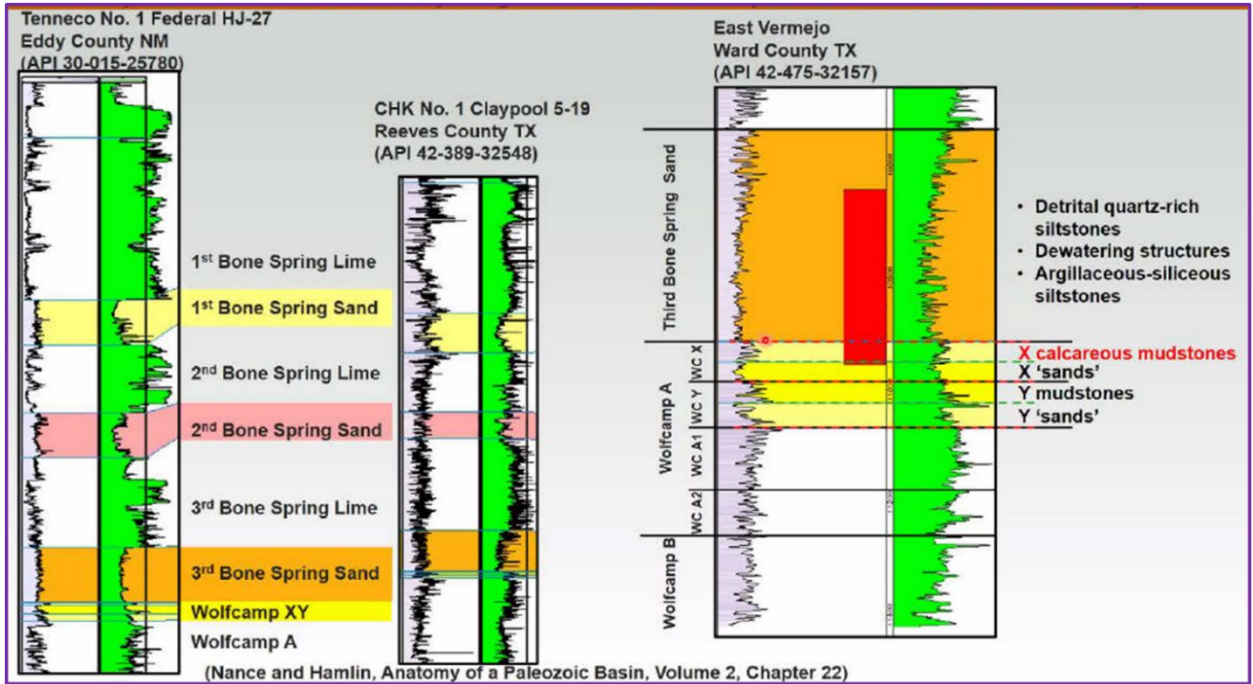
Figure 13, Repeated siliciclastics and carbonate sequences. Carbonates represent high stands and siliciclastics represent lowstands. From Nance and Hamlin (2020).

Figure 14, Type log used in this study from Big Moose Fed Com 604H well. The sequence is characterized by interbedded siliciclastic and carbonates. Type Log includes Track 1 MWD Gamma Ray and EGR (U+K+Th), Track 2 Modelled Mineralogy from XRF Elements, Track 3 Aluminum, Track 4 Silica, Track 5 Calcium and Track 6 Chemofacies. Carbonates are predominant in glacio-eustatic highstand during marine transgression. Siliciclastics are associated with lowstands.

5. METHODOLOGY

5.1 Materials and Data

Elemental data were obtained from drill cuttings care of Ascent Energy. The XRF data was measured during the drilling of the well and the cuttings were disposed. Diversified Well Logging collected the samples at an average of 30-50 ft intervals and conducted the XRF analysis on 10 wells in the Delaware Basin (Figure 15., Table 2). The average number of samples per well is 200. All wells have gamma ray (GR) well log data, azimuth, and inclination information that were recorded during drilling. One well (Big Moose 604H) has a full suite of wireline logs, including gamma ray (GR), resistivity (RES), bulk density (RHOB), neutron porosity (NPHI), and Elemental Capture Spectroscopy (ECS), which measures the dry weight % of Si, Ca, Fe, S, Ti and Gd in a formation.

Table 2. List of wells used in this study from Lea County, New Mexico, and corresponding data.

	XRF	GR	Density	Sonic	Porosity	ECS	Resistivty	API	Start Depth Ft. MD	End Depth Ft. MD	Latitude	Longitude
Big Bucks fed Com 501H	x	x						30025470640000	5,770	17,009	32.50049	-103.62113
Big Bucks fed Com 502H	x	x						30025474350000	5,865	17,150	32.50042	-103.62113
Big Stag Fed Com 503H	x	x						30025469780000	5,850	17,012	32.50070	-103.62693
Big Stag Fed Com 504H	x	x						30025470660000	5,850	17,300	32.50070	-103.62702
Big Stag Fed Com 703H	x	x						30025469790000	5,581	18,027	32.50070	-103.62685
Big Moose fed Com 506H	x	x						30025465470000	5,640	17,255	32.50152	-103.63430
Big Moose fed Com 604H	x	x	x	x	x	x	x	30025465480000	5,660	18,140	32.50152	-103.63420
Toque State Com 502H	x	x						30025447850000	5,430	17,785	32.50759	-103.61443
Toque State Com 601H	x	x						30025447870000	5,530	19,130	32.50759	-103.61404
Toque State Com 602H	x	x						30025447880000	5,680	19,179	32.50759	-103.61433
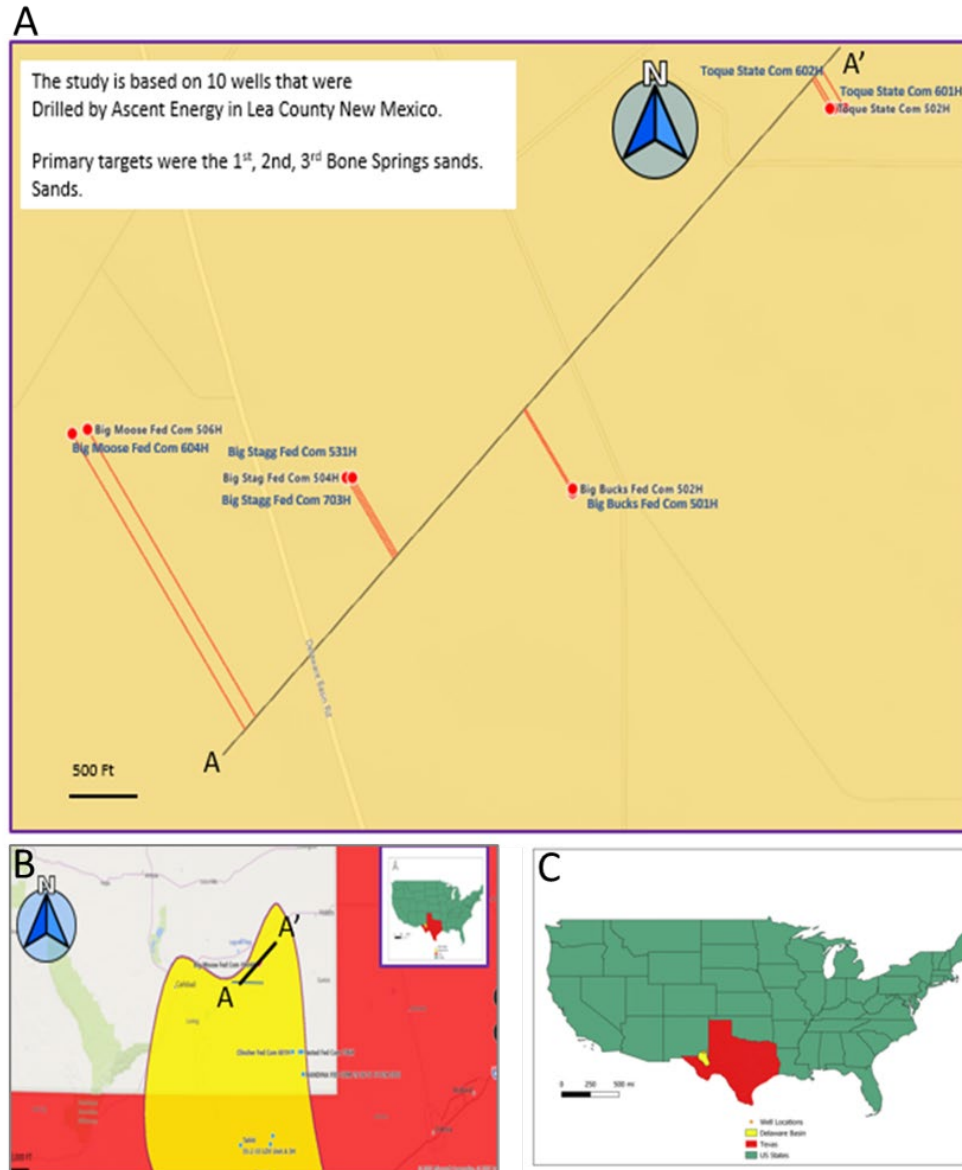
Figure 15, (A) Map of the study area and well location in Lea County, New Mexico, Delaware Basin. (B) Inset map of the Texas-New Mexico border, with Texas in red, and the Delaware Basin shaded in yellow. (C) Map of the United States, with Texas in red and the Delaware Basin in yellow. Well locations are in red. Orange lines are perpendicular to the cross section line chosen.

The workflow (Figure 16.) consisted of first gathering the XRF measurements from the drill cuttings and the wire line logs. The XRF data were processed in the JMP statistical software package after Data QAQC. The software pemits a combination of Hierarchical Cluster Analysis (HCA) and Principal Component Analysis (PCA) to characterize the data into seven chemical facies or chemofacies. Both sets of data were brought into Logscope® software for petrophysical analysis. Shapefiles were created of elements and algorithms of elements and imported into QGIS to plot concentrations across the region.
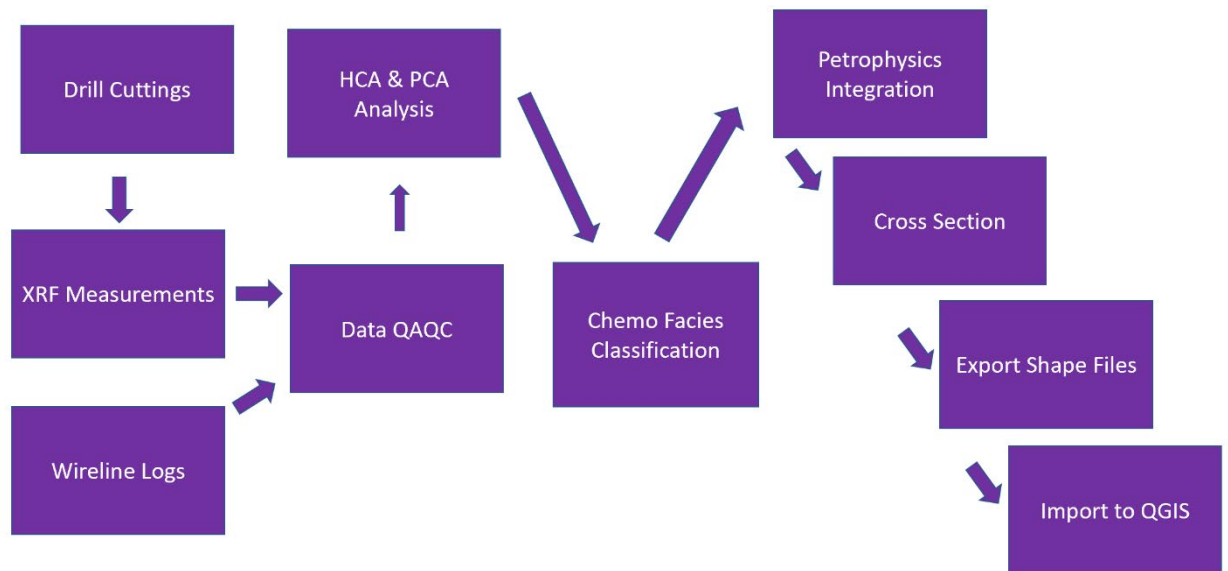
Figure 16, Drill cuttings and petrophysics workflow. XRF data from drill cuttings is merged into LogScope with downhole logs. Data is imported into an HCA/PCA analysis package and chemofacies are created. Cross sections are generated, and elemental attributes are geospatially mapped.

5.2 XRF

XRF was measured with a portable benchtop Spectro Scout at the well site while

drilling was taking place. Samples were collected during the drilling process using 10 (2mm), 80 (0.177mm) and 120 (0.125mm) mesh sieves. Mesh size refers to the number of openings per square inch. The samples were cleaned with diesel fuel and Dawn dish soap to remove oil-based mud contamination. They were then dried with a vacuum dryer (not heat). A small 5.5 g of the collected and cleaned sample was ground using a ball mill with 2 x 12 mm tungsten balls for 30 seconds. Samples were then placed into a vacuum cup and entered the XRF Portable Benchtop Spectroscout. A proprietary calibration method for mudrocks was used called "DWL Geo." The samples were calibrated against the USGS SDC (Science Data Catalog) standard every 5th sample processed to ensure calibration of the instrument. Element concentrations were determined by cooperating laboratories using a variety of analytical methods (Table 3).

Table 3, SDC standard materials for XRF machine calibration. United States Geological Survey Certificate of Analysis Mica Schist, SDC-1.

Listed in mass %	
SDC Standard	
Brammer Standard Database	
Element	Concentration
SiO_2	65.5
Al_2O_3	15.8
CaO	1.4
FeO	3.93
Fe_2O_3	6.32
K_2O	3.28
MgO	1.69
Na_2O	2.05
P_2O_5	0.16

Specific elements used for proxies consisted of: redox sensitive trace elements

(RSTE's: Ni, Zn, V, Mo, U), detrital deposition (Si, Al, Ti, Zr, Rb), carbonate deposition (Ca, Mg, Sr), phosphate enrichment (P, Y), and sulfur enrichment (S) (Baumgartner and Rowe, 2017). Si/Al, Si/Zr ratios were calculated as a proxy for grain size (Driskill, 2018). The total set of elements used are listed in (Table 4).

Table 4, List of elements measured by the XRF.

Cl	Si	Ti	Al	Fe	Mn	Mg	Ca	K	P	S	V
Cr	Ni	Cu	Zn	Rb	Sr	Y	Zr	Mo	W	Tl	Pb
Th	U										

The XRF data were used to determine mineralogy using a proprietary, forward modelling logic, stoichiometric mineral model method developed by Diversified Well Logging but based on previous work by Cohen and Ward 1991 (Figure 17.). The order of calculations is listed in Table 5. The "Limiting Element" means that all of a particular element remaining at that calculation step is used to calculate the abundance of the mineral
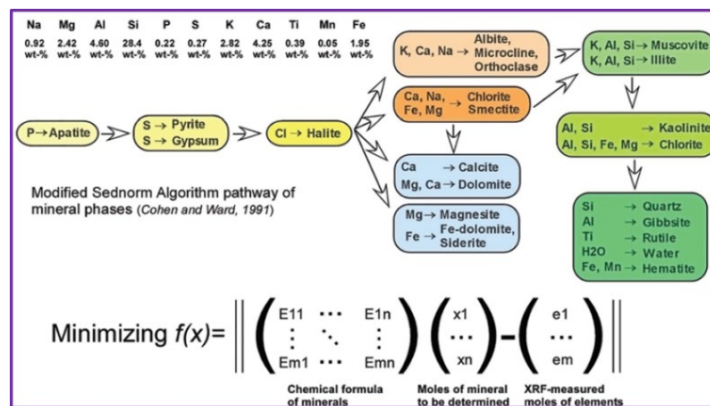
Figure 17, Sequence and algorithm for mineralogy calculation. (Cohen and Ward, 1991)

31

There are several key assumptions that were made during the mineralogy calculations. Fe and Mg are present in equal amounts in chlorite. All plagioclase is albite (sodic end member), although note Na is difficult to measure with the XRF instrument utilized. No K-feldspar is present. All K_2O present is found in illite. No mixed-layer illite/smectite is present. All K_2O is contained in illite. MnO is not significant and is not utilized in the calculation. The above assumptions are based on previous work calibrating the responses to mineralogy via X-ray diffraction in the Permian Basin.

Table 5, List of minerals and chemical formulas used in the normative calculations in this study.

Order of Calculation	Mineral Calculated	Mineral Formula	Limiting Element 1	Limiting Element 2	Limiting Element 3	Limiting Element 4
1	Rutile	TiO_2	TiO_2			
2	Fluorapatite	$Ca_5(PO_4)_3(F)$	P_2O_5	CaO		
3	Barite	$BaSO_4$	BaO	SO_3		
4	Pyrite	FeS_2	SO_3			
5	Chlorite	$Mg_3Fe_3Si_2Al_2O_{10}(OH)_8$	Fe_2O_3	MgO	Al_2O_3	SiO_2
6	Dolomite	$Ca_{0.5}Mg_{0.5}CO_3$	MgO	CaO		
7	Calcite	$CaCO_3$	CaO			
8	Halite	NaCl	Cl	Na_2O		

9	Albite	$NaAlSi_3O_8$	Na_20	Al_2O_3	SiO_2	
10	Illite	$KAl_4(Si_7AlO_{20})(OH)_4$	K_2O_4	Al_2O_3	SiO_2	
11	Kaolinite	$Al_2SI2O_5(OH)_4$	Al_2O_3	SiO_2		
12	Quartz	SiO_2	SiO_2			

5.2 XRF Analyses – PCA and Cluster Analysis

XRF measurements were grouped as chemical facies (chemofacies) using a combination of Hierarchical Cluster Analysis (HCA) and Principal Component Analysis (PCA). Cluster analysis groups the samples based on the degree of similarity to one another using Ward Euclidian distance. PCA is a statistical procedure that allows you to summarize the information content in large data tables by means of a smaller set of "summary indices" that can be more easily visualized and analyzed.

The workflow was to first upload raw XRF data files into JMP for analysis. The first step was to conduct Quality Assurance and Quality Control (QAQC) on the data set to remove outliers and missing data. Due to low or missing values, the following elements were used (Table 4). In addition, the JMP software has the option to also remove low or missing values automatically. This method was chosen, i.e., the missing or low data values were removed.

HCA was then run on the clean dataset. HCA separates the clusters using the Euclidean distance, which measures the distance between two centroids (Ward, 1963). The number of clusters chosen was based on the "Thorndike" method, which looks at the

cluster similarity at each stage based on the Euclidean distance (Thorndike, 1953). The most significant advantage of using HCA is that we can manually assign and adjust the number of final clusters based on geological background and compare clustering solutions for different values to determine an optimal number of clusters for the data sets. Seven clusters were chosen because the eigenvector results in the PCA indicated seven clusters with a number greater or close to 1 and visually allowed for reasonable cluster separation. The resultant PCA chemofacies were described based on their elemental composition using a combination of the bulk elements and the S-Core mudstone classification scheme and the trace elements.

5.4 Petrophysical Analysis

After clustering, each chemofacies was assigned a number based upon the results from the HCA and PCA and imported into Logscope petrophysical software package from Harvey Rock Geophysics along with the raw XRF and available well log data for further analyses. Logscope Software is a petrophysical software that allows for multiwell analysis of fluids and rock properties. These evaluations use well log data to analyze a formation for various reservoir characteristics, such as porosity, shale content, permeability, or clay minerals. Variables in the analyses can easily be modified to fit a region, which are then updated across the project. The evaluations are conducted through established cross plots (Schlumberger Log Interpretation Charts, 2013), that have been calibrated using laboratory measurements. Furthermore, it allows for visualization of changes across the

region. Cross sections can easily be created consisting of chemofacies, well log data, and petrophysical properties. The logs uploaded into Logscope for petrophysical evaluation include gamma ray (GR), resistivity (RES), bulk density (RHOB), neutron porosity (NPHI), and Elemental Capture Spectroscopy (ECS) (Table 1).

In Logscope, formations boundaries were determined using the gamma ray log and the type curve (Figure 14.). Next, the XRF data were used to calculate an elemental gamma ray (EGR) curve. This curve was used to compare the cuttings depth to the well log depth for proper correlation of information. The EGR was calculated using the following formula where K_2O, Th, and U were measured by the XRF. This equation was calibrated using other wells in the field and is based on the original formula after Ellis & Singer (1987):

$$\text{Equation 1 } GR = 16K2O + 8U + 4Th$$

where K is potassium in wt. %, U is uranium in ppm, and Th is thorium in ppm. The Elemental Gamma Ray logs were compared to downhole Gamma Ray logs that were acquired both while drilling (MWD) and the downhole tools ran after drilling. This helped to ensure that the cuttings were assigned the correct depth and can represent the formation when compared to the well logs.

Lithology was interpreted from the wireline log using the Big Moose fed Com 604H well, which has a full suite of well logs. This was conducted primarily using the ECS log coupled with the gamma ray and density. The combination of these three tools provided downhole lithologies that were compared directly to the modeled mineralogy from the

XRF. This was then correlated based upon the gamma ray curve. Oftentimes, the only curves measured on well logs are the gamma ray curve. Establishing a model to extrapolate data is important to create regional correlations, especially where data is scarce.

The XRF mineralogy derived from the mineral model described above was compared to the wireline mineralogy estimated from Elemental Capture Spectroscopy ECS wireline tools. A visual estimate of covariance was used.

The volume of shale was calculated from the gamma ray curve using the following formula:

Equation 2 $VCLAY = GR\text{-}GRmin/(GRmax\text{-}GRmin)$

where GR is the measured gamma ray value at a given depth, GRmin is the minimum gamma ray value for the location, interpreted as being a "clean" or shale-free zone, GRmax is the maximum gamma ray value for the location, interpreted as being 100% shale.

The XRF clay content (Equation 2) was compared to the Vshale calculated content. The petrophysical properties calculated were then compared to the elemental data to establish relationships to rock properties that could be extrapolated across the region. The GEMS Tool Total Organic Content (TOC) using the Passey Method was compared to modeled TOC from paleo redox elemental proxies in source rocks (mudstones in the Bone Spring Formation). The TOC calculation in LogScope used the Passey Method from Passey et al. (1990). They used the change in deep resistivity and porosity curves to highlight the

presence of organic-rich intervals in source rocks. In 'lean' source rocks, the curves overlie

one another. Organic-rich intervals are highlighted by curve separation, indicating a low

density and high resistivity. Using the gamma-ray curve, reservoir intervals were

identified and eliminated from the analysis, based upon the low gamma ray values (<50

API). The separation in organic-rich intervals results from two effects: the porosity curve

responds to the presence of low-density, low-velocity kerogen, and the resistivity curve

responds to the formation fluid. In an immature organic-rich rock, where no hydrocarbons

have been generated, the observed curve separation is due solely to the porosity curve

response (Passey et al., 1990). The magnitude of the separation indicates amount of TOC,

which has been calibrated from laboratory measured TOC values and maturity data.

Although ideal, it is not necessary given the amount of data available, and assumptions

which can be made based upon generalized worldwide source rock trends, which is done

by default in Logscope.

The brittleness was calculated using the XRF data in Logscope, and compared to

the Sonic log. The brittleness of a rock describes its failure behavior during exposure to

increasing stress. Rocks characterized by a high brittleness index typically have a high

Young's modulus (E) and low Poisson's ratio (P) (Rickman et al., 2008). While pressure and

temperature can affect the brittleness index, a primary controlling factor that affects it is

the composition of the material. For example, a clay or mudstone will tend to be more

malleable or ductile. Quartz and calcite on the other hand, with a higher density and

hardness, will be more brittle. Overall, in geologic materials, certain minerals are

37

mechanically more competent. Previous work by Wang and Gale (2009) used the following formulas:

Equation 3
$$BI = \frac{VQTZ}{VQTZ+VCl+VCAL}$$

Where V is the volume in weight percent of a given mineral or set of minerals. Wang and Gale (2009) also proposed a further modified version:

The equation used with the XRF elemental data was:

Equation 4
$$BI = \frac{VQTZ + VDOL}{VQTZ + VDOL + VCL + VCAL + VTOC}$$

Equation 5
$$BI = \frac{Ca}{Si + Ca + Al}$$

The brittleness was also calculated using the formula below from the modeled mineralogy:

Equation 6
$$BI = \frac{VQTZ+VCAL}{VQTZ+VCl+VCAL}$$

XRF brittleness was compared to the sonic log for geomechanical properties. Both a visual and R^2 comparison was performed. The sonic log is an important log because it can be used as a proxy for mechanical characteristics. Oftentimes, a faster travel time reflects a more competent rock because of the changes in density of the different lithologies. A mudstone or claystone is less dense and thus will have a longer travel time. A competent packstone carbonate will reflect the sonic wave very quickly because it is denser compared to mudstones or sandstones

The highest values with the coarsest grains can be found in the Toque State wells. This is also the wells with found within chemofacies 6 enriched in detrital and siliceous components Grain size can be estimated using elemental ratios such as Zr/Al (Driskill et al., 2018). There are two grain size formulas:

Equation 7 $\text{Grain Size} = \frac{Zr}{Al}$

Equation 8 $\text{Grain Size Detrital} = \frac{Zr+Ti+Rb}{Al}$

Here, I used equation 7 to calculate the relative grain size within the formations.

5.5 Mapping

Combinations of elemental measurements were mapped across the study area to assess spatial changes. Wells were first imported as CSV data files into Logscope. Using the solver feature in Logscope, derived parameters were calculated from the elemental data sets. The redox sensitive trace elements (RSTE) calculation was the average of the sum of the U, Cr, Ni, Zn elements. The grain size was estimated using the Zr/Al ratio. These data sets were averaged for each formation interval, 1st Bone Spring Lime, 1st Bone Spring Sand, 2nd Bone Spring Lime, etc., and were exported as shapefiles and imported into QGIS. The inverse distance weighting (IDW) interpolation was used to generate rasters and were contoured. IDW estimates unknown values within a specified search distance, closest points, power setting and barriers. It is mathematical (deterministic) and assumes closer

values are more related than further values with its function. Appropriate color properties were changed using the symbology and color ramps that best represented the data. Isochore and structure maps were not completed on these wells, as much of the lower section were laterals – the horizontal portion of the well.

6.   RESULTS AND INTERPRETATION

6.1 XRF Analyses

Below is a summary of the XRF analyses performed.

6.1.1 Formation Mineralogy and Distribution

Based upon the modeled mineralogy and general trace elemental composition, the Big Lime has an average composition of calcite 60%, quartz 21%, illite 11%, dolomite 4%, pyrite 1% and chlorite 1%. The redox sensitive trace element (RSTE) score is 171. The calculated Brittle Index (BI) is 19 and the grain size Zr/Al ratio is 22.

The Avalon has an average calcite composition of 62%, quartz 30%, illite 11%, dolomite 4%, pyrite 1%, and chlorite 1%. The RSTE redox sensitive trace metal score is 314, suggesting it is more organic rich than the Bone Spring Lime. The BI is 20 and the grain size Zr/Al ratio of 24.

The 1st Bone Spring Lime has an average calcite composition of 53%, quartz 30%, illite 10%, dolomite 4%, pyrite 2%, and chlorite 1%. The RSTE redox sensitive trace metal score is 229, falling in between the Bone Spring Lime and Avalon. The BI is 26 and the grain size Zr/Al is 18.

The 1st Bone Spring Sand has an average calcite composition of 41%, quartz 46%, illite 9%, dolomite 2%, pyrite 2% and chlorite 0%. The RSTE redox sensitive trace metal score is 312, indicating a relatively high organic richness, the Brittle Index is 49, i.e., much more competent than the Big Lime, Avalon, and 1st BSPG Lime, and the grain size

41

Zr/Al is 22.

The 2nd Bone Spring Lime has an average calcite composition of 42%, quartz 41%, illite 10%, dolomite 4%, pyrite 1% and chlorite 1%. The RSTE redox sensitive trace metal score is 267 the Brittle Index is 39 and the grain size Zr/Al is 31.

The 2nd Bone Spring Sand has an average calcite composition of 20%, quartz 49%, illite 21%. Dolomite 5%, Pyrite 1% and Chlorite 3%, i.e. much higher quartz content and an increase in chlorite. The RSTE redox sensitive trace metal score is 232, the Brittle Index is 49 (increasingly more competent) and the grain size Zr/Al is 52, indicating a much coarser grain size.

The 3rd Bone Spring Lime has an average calcite composition of 27%, quartz 45%, illite 18%, dolomite 4%, pyrite 2%, and chlorite 3%. The RSTE redox sensitive trace metal score is 250, the Brittle Index is 45 and the grain size Zr/Al is 49.

The 3rd Bone Spring Sand has an average calcite composition of 3%, quartz 57%, illite 27%, dolomite 6%, pyrite 0%, and chlorite 5%. The RSTE redox sensitive trace metal score is 250, the Brittle Index is 45 and the grain size Zr/Al is 49. The clay content is higher in this formation. The calcite composition is significantly lower.

The cross section (Figure 18.) shows the modelled mineralogy for all 10 wells derived from the XRF drill cuttings measurements. The Big Lime carbonate is a clear marker across the study area. This is followed by the Avalon, 1st Bone Spring Lime, 1st Bone Spring Sand, 2nd Bone Spring Lime and 2nd Bone Spring Sand can be followed with the charge in mineralogy from Calcite to Quartz across the area, indicating a change in

42

carbonate composition and facies. There is a general increase in the carbonate from the

3rd Bone Spring sand up to the Big Lime.
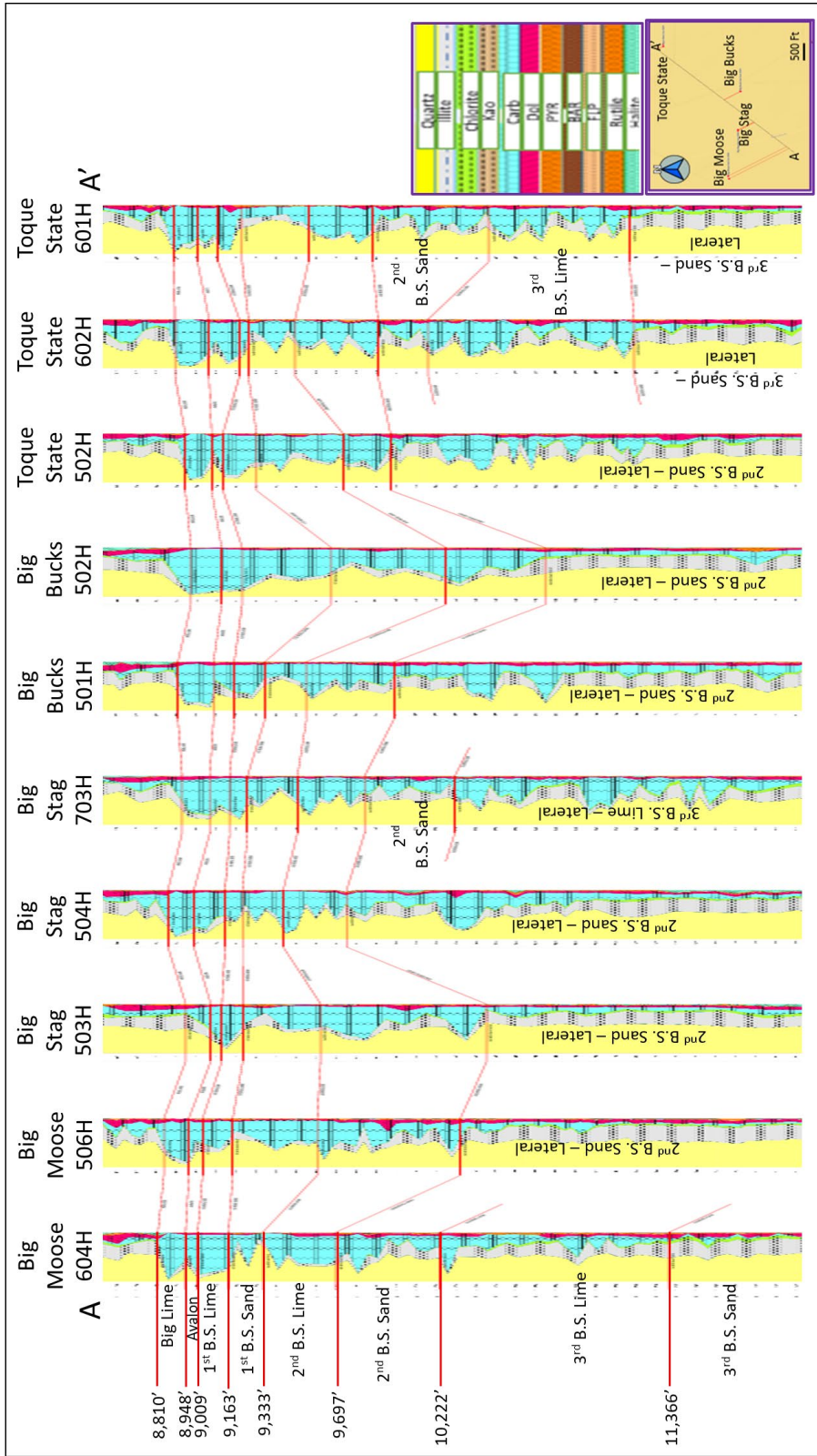
Figure 18, Plot of modelled mineralogy from XRF across the study area. The Big Stag Fed Com 703H has the highest carbonate composition in the lateral; this is a 3rd Bone Spring Lime well. Wells drilled in the Middle 2nd BSPG Lime (Big Stag Fed Com 504H and Big Bucks Fed Com 502H also have a higher carbonate composition.

6.1.2 PCA

Principal Component Analysis was run on the entire dataset after removing outliers and missing values. After removal of missing data, 26 of the elements were selected from the original 54 elements. There were seven components that had eigenvalues greater than 1, representing 80.395% of the total variance in the dataset (Table 6). This criterion also suggests that seven clusters should be used for the cluster analysis, and that seven clusters is statistically meaningful; more would create unnecessary groupings that would not be statistically different. Fewer clusters would group individual chemofacies that could be separated into meaningful geological units.

Table 6, Calculated eigenvalues for the principal components of the XRF data from all ten wells. The percent represents the amount of variance a component represents.

Eigenvalues					
Number	Eigenvalue	Percent	20 40 60 80		Cum Percent
1	8.7336	33.591			33.591
2	4.3223	16.624			50.215
3	2.2174	8.528			58.743
4	1.9456	7.483			66.226
5	1.4859	5.715			71.941
6	1.2012	4.620			76.562
7	0.9966	3.833			80.395
8	0.7371	2.835			83.230
9	0.6630	2.550			85.780
10	0.6030	2.319			88.099
11	0.5779	2.223			90.322
12	0.5188	1.996			92.317
13	0.4586	1.764			94.081
14	0.3584	1.378			95.459
15	0.3329	1.280			96.740
16	0.2732	1.051			97.791
17	0.2051	0.789			98.579
18	0.1829	0.703			99.283
19	0.1639	0.630			99.913
20	0.1301	0.500			100.414
21	0.0947	0.364			100.778
22	0.0510	0.196			100.974
23	0.0370	0.142			101.116
24	0.0202	0.078			101.194
25	0.0123	0.047			101.241

PC1 and PC2 were then used to determine the geological interpretation of the seven clusters. The Loading Scores (Table 7) indicate that Al, Rb, K, Ti, Si, Zr, Y, Fe, and Th

are strongly correlated, while negatively correlating with Tl, Sr, and Ca for PC1. This can be interpreted as the partitioning of the mineral-sensitive elements: high PC1 scores at a given depth indicates high values of Al, Rb, K, Ti, Si, Zr, Y, Fe, and Th, suggesting siliceous mudrocks, while low PC1 scores indicate high values of Tl, Sr, and Ca, suggesting carbonate lithofacies. PC 2 generally represents the enrichment of redox-sensitive Ni, U, Mo, Cu, and Cr; positive values indicate a given depth is redox-sensitive elements-rich, whereas negative values indicate that a depth is redox- sensitive element depleted (Figure 19.).

	Prin1	Prin2
Al	0.963928	-0.015009
Rb	0.957690	0.125417
K	0.954164	-0.069520
Ti	0.944007	-0.106510
Si	0.883612	-0.007982
Zr	0.872586	-0.342184
Y	0.765671	0.245099
Fe	0.739478	0.331862
Th	0.704966	0.360613
Ni	-0.089557	0.849995
U	-0.011342	0.770996
Mo	-0.270673	0.716480
Cu	0.367854	0.611510
Cr	0.113560	0.591483
P	0.104805	0.523764
V	0.234106	0.473962
Zn	0.056995	0.446189
S	-0.164408	0.208350
Cl	-0.034738	-0.194416
Mg	-0.069252	-0.344673
W	0.184233	-0.241459
Tl	-0.438539	0.343225
Pb	0.069908	0.285061
Mn	0.224889	-0.241335
Sr	-0.643383	0.308489
Ca	-0.941309	0.099390

Table 7, Loading matrix for PC1 (Prin1) and PC2 (Prin2) for the 23 elements.
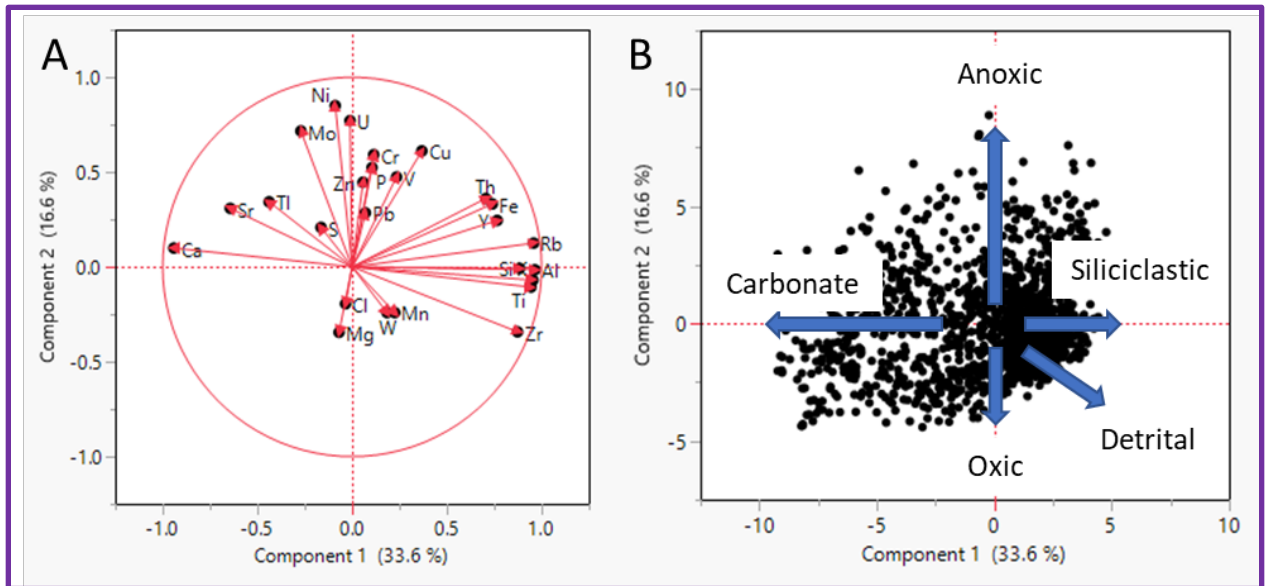
Figure 19, (A) Loading scores for Component 1 compared to the loading scores for Component 2. This shows clustering of similar elements. (B) Cross plot of component scores for Component 1 vs. Component 2 for all the downhole data, showing interpretations of the elements based upon correlations within each component where individual points down-well plot. These can be interpreted as chemofacies based upon the values in the loading matrix (Table 7).

6.1.3 Hierarchical Cluster Analysis

The HCA divided the data into seven clusters representing seven different

chemofacies (

Figure 20). The component scores generated for every data point (here, depth in

a well) by the PCA were also plotted on the PC1 vs. PC2, and color coded based upon the

HCA chemofacies classification (Figure 21.). The data was also plotted on a S-Core ternary

diagram, a mudrock classification system, to help with chemofacies interpretation.

Generally, Ca and Sr elements provide an indication of the onset for carbonate deposition.

Fe, Rb, Al, Zr, Ti all provide indication of a terrigenous input and are related to siliciclastic

deposits. These Ca and Sr elements are indicative of transgressive higher seal level

depositional settings. The terrigenous elements are indicative of sea level falls i.e., regressive systems tracts. Redox sensitive trace elements U, Cr, Ni, Zn and V elements are indicative of increasing anoxia or flow restriction. Uranium is absent during high levels of carbonate deposition. Coupled, these can aid in interpreting depositional conditions for chemofacies.

B

1. Chemofacies 1 is a carbonate siliceous mudstone. It falls on the Negative side of PC1 indicating enrichment of Ca and Sr but not As enriched as Chemofacies 2 and 3. It is on the positive side of 2 indicative of slightly dysoxic to anoxic conditions with some Enrichment in S and Zn.

2. Chemofacies 2 is a silica rich carbonate mudstone. It falls on the far Negative side of PC1 with enrichment in Ca and Sr . It is on the negative side of PC2 indicative of oxic conditions of deposition.

3. Chemofacies 3 is a mixed carbonate mudstone. It falls on the Negative side of PC1 with enrichment in Ca and Sr . It is on the negative side of PC2 indicative of oxic conditions of deposition. Other element association is magnesium potentially indicating dolomitization.

4. Chemofacies 4 is a mixed siliceous carbonate mudstone. It falls in the middle of PC1 and PC2 indicating a mixed system deposited in oxic/dysoxic conditions. Here we have equal distribution of siliceous and carbonate elements.

5. Chemofacies 5 is a mixed carbonate siliceous mudstone. It falls in the middle of PC1 and slightly negative in PC2 indicating a mixed system deposited in oxic conditions. It has a slightly more calcareous composition. .

6. Chemofacies 6 is a clay rich mixed siliceous mudstone. It falls in the positive side of PC1 and slightly negative in PC2 indicating a detrital composition enriched in Zr and Ti deposited in oxic conditions.

7. Chemofacies 7 is a clay rich mixed siliceous mudstone. It falls in the positive side of PC1 and positive in PC2 indicating a siliceous composition enriched in RSTE's U, Cr, Ni, Zn and V deposited in anoxic conditions. .

Figure 20, (A) Dendrogram from the Hierarchal Cluster Analysis showing seven groupings of rocks with similar elemental chemical composition and (B) corresponding chemofacies described from the PCA results and correlations of elements.
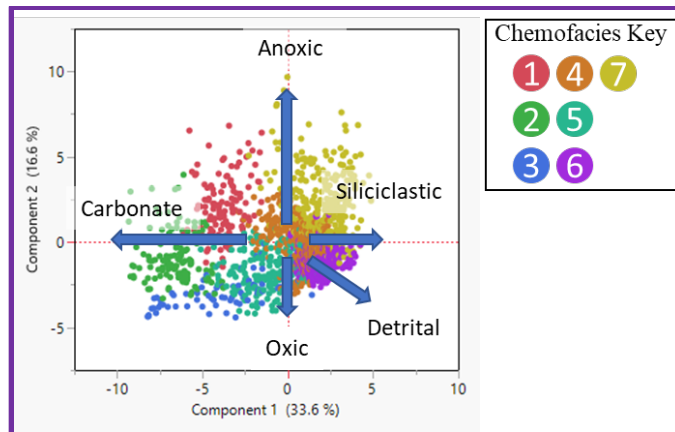
Figure 21, Loading scores for all data across the ten wells generated by the PCA and color coded based upon the seven chemofacies classification generated by the HCA. Chemofacies interpretation (lithofacies + redox conditions) are based upon the general bulk elemental composition (PC1) coupled with redox sensitive element enrichment or depletion (PC2).

Chemofacies 1 (CF1) is a carbonate-siliceous mixed mudstone. According to the modelled mineralogy, chemofacies 1 has an average of 44% quartz, 11% illite, 40% calicte, 3% dolomite and 2% pyrite. It falls on the negative side of PC1 indicating enrichment of Ca and Sr but not as enriched as Chemofacies 2 and 3 (Figure 19.). It is on the positive side of Chemofacies 2, indicative of slightly dysoxic to anoxic conditions with some enrichment in S and Zn (Figure 19.). This suggests a deeper water environment of deposition influenced by periodic siliceous sediment pulses.

Chemofacies 2 (CF2) is a silica rich carbonate mudstone coupled with carbonate dominated lithotype. CF2 has an average composition of 23% quartz, 6% illite, 66% calicte, 5% dolomite and 1% pyrite. It falls on the far negative side of PC1, with enrichment in Ca and Sr. It is on the negative side of PC2, indicative of oxic conditions of deposition (Figure 21.).

This suggests shallower water conditions with primarily carbonate deposition with a periodic influx of terrigenous sediments.

Chemofacies 3 (CF3) is predominantly a combination of mixed carbonate mudstone through carbonate-dominated lithotypes, although with some mixed siliceous mudstone. It falls on the negative side of PC1 with enrichment in Ca and Sr. It is on the negative side of PC2, indicative of oxic conditions of deposition. Magnesium is also associated with chemofacies 3, potentially indicating dolomitization. CF3 has an average composition of 24% quartz, 13% illite, 12% calcite, 47% dolomite and 2% pyrite. This chemofacies suggests shallower water conditions with primarily carbonate deposition, with a periodic influx of terrigenous sediments. It could potentially be "transitional facies" – a coupling between chemofacies 2 and chemofacies 4, with constant interbedding and mixing. Enrichment in dolomite could have been related to higher ambient temperatures during deposition or could also indicate higher levels of diagenesis with mg replacing calcite.

Chemofacies 4 (CF4) is a mixed siliceous carbonate mudstone. It falls in the middle of PC1 and PC2, indicating a mixed system deposited in oxic/dysoxic conditions. Here we have equal distribution of siliceous and carbonate elements. It has an average composition of 53% quartz, 27% illite, 12% calcite, 5% dolomite and 2% pyrite. This suggests also transitional facies between regressive and transgressive sea level with period tectonically induced gravity flows coupled with hemipelagic sedimentation.

Chemofacies 5 (CF5) is a mixed carbonate siliceous mudstone. It falls in the middle

50

of PC1 and slightly negative in PC2, indicating a mixed system deposited in oxic conditions. It has an average composition of 47% quartz, 20% illite, 22% calcite, 8% dolomite and 1% pyrite slightly more calcareous composition indicative of higher sea levels.
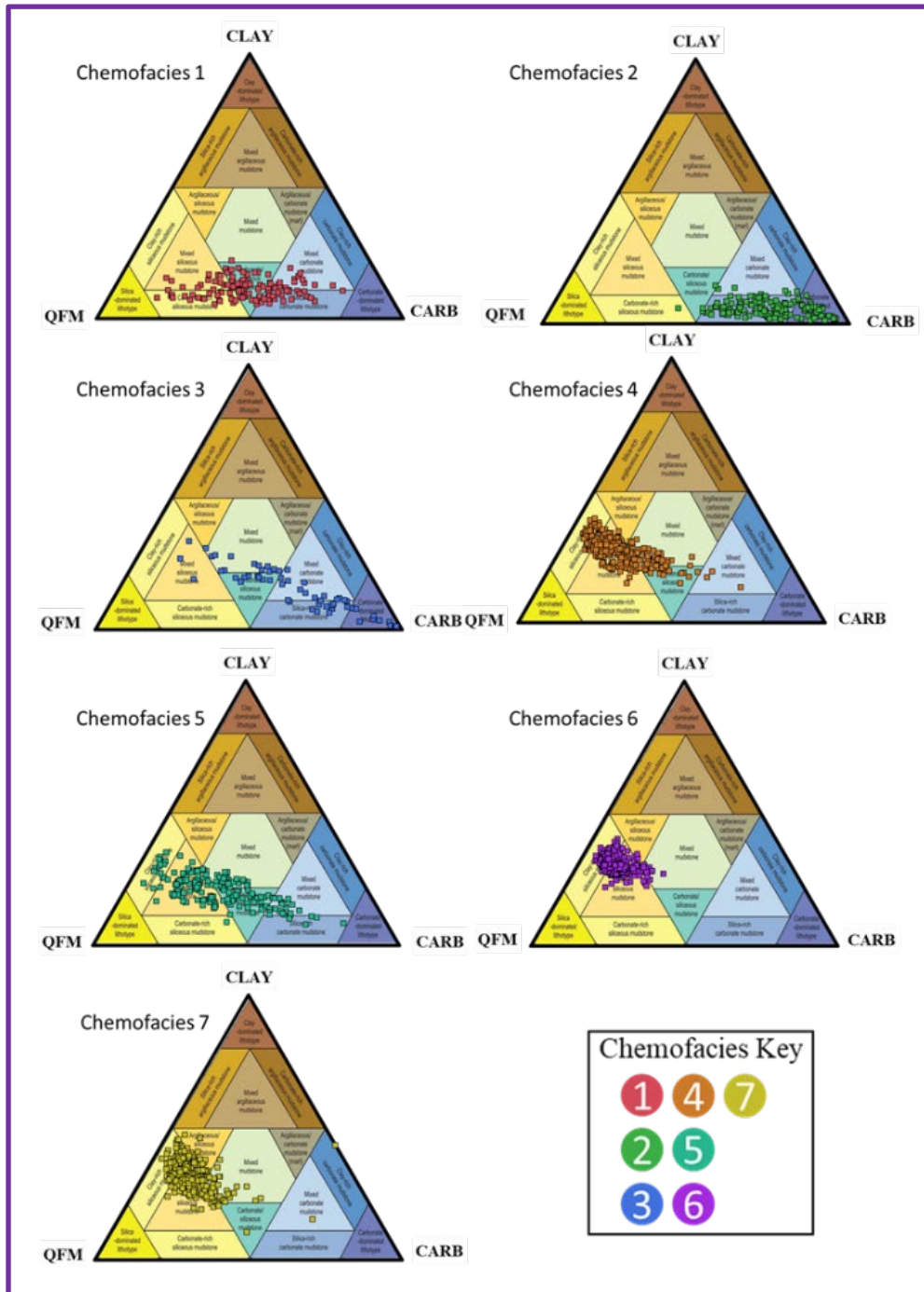
Figure 22, Ternary diagrams of each chemofacies linking the chemical composition with lithofacies.
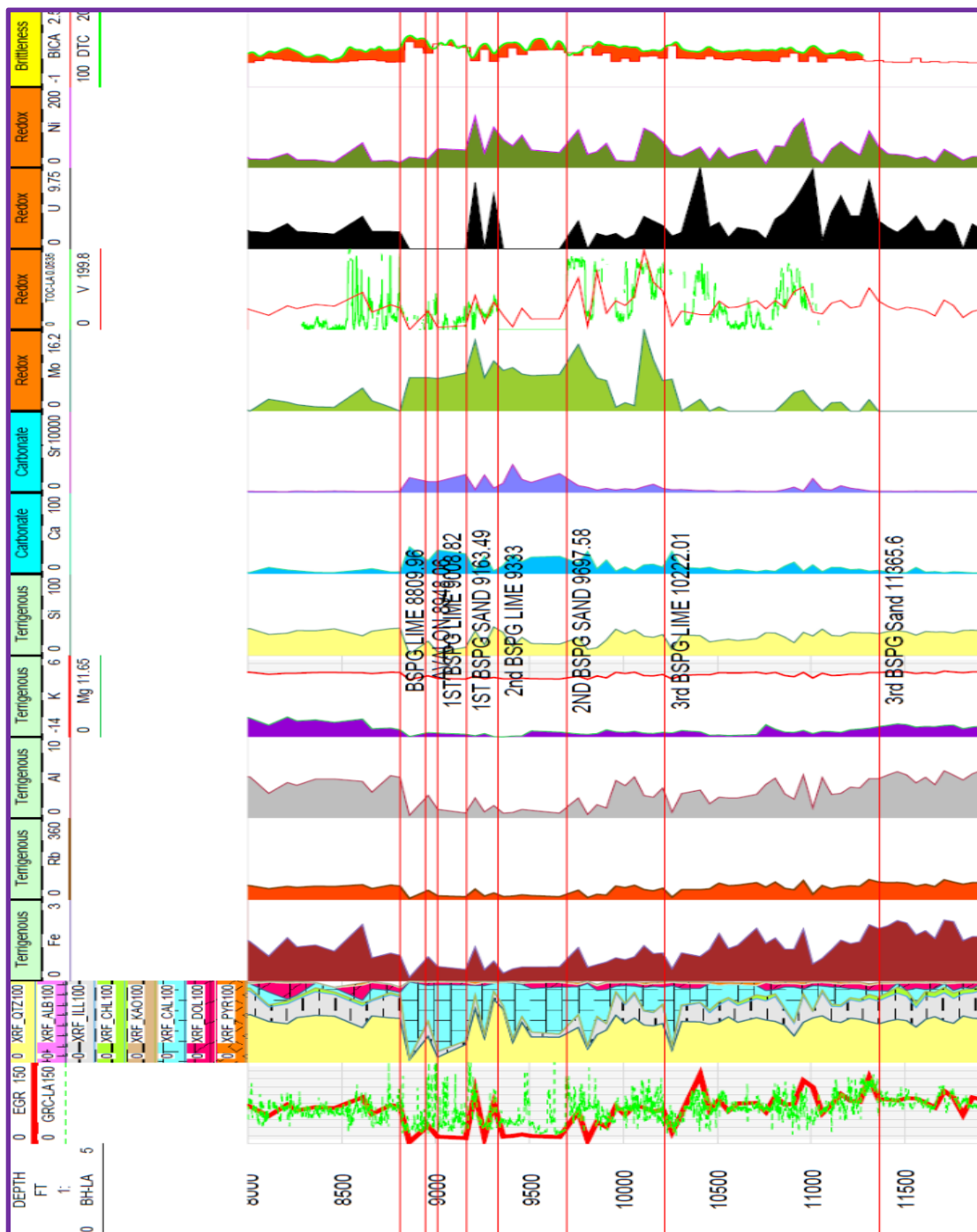
Figure 23, An example well showing, from left to right, depth, elemental gamma ray (EGR) (U+K+Th), mineralogy, terrigenous Input (Fe, Rb, Al, K Si), carbonate (Ca, Sr), paleoredox indicators (Mo, V, U, Ni), and brittleness index (BI). This is from the Well Big Moose Fed

Com 604H. These enrichments or depletions in elements aid in interpretation of depositional conditions.

Chemofacies 6 (CF6) is a clay rich mixed siliceous mudstone. It falls in the positive side of PC1 and slightly negative in PC2 indicating a detrital composition enriched in Zr and Ti deposited in oxic conditions. It has an average composition of 56% quartz, 30% illite, 6% calcite, 6% dolomite and 1% pyrite. This would be indicative of lower sea levels, a regressive system with an increase in terrigenous detrital material. This has the highest quartz composition at 56%. These could be associated with silica-rich hemi-pelagic sediment gravity flows.

Chemofacies 7 (CF7) is a clay rich mixed siliceous mudstone. It falls in the positive side of PC1 and positive in PC2 indicating a siliceous composition enriched in RSTE's U, Cr, Ni, Zn and V deposited in anoxic conditions. It has an average composition of 50% quartz, 31% illite, 11% calcite, 5% dolomite and 2% pyrite. This would indicate a regressive sea level environment with sediment accumulating in a stagnant, lower energy and lower circulation environment. For a summary of the rock compositions for each chemofacies see (Table 8). , An example well showing, from left to right, depth, elemental gamma ray (EGR) (U+K+Th), mineralogy, terrigenous Input (Fe, Rb, Al, K Si), carbonate (Ca, Sr), paleoredox indicators (Mo, V, U, Ni), and brittleness index (BI). This is from the Well Big Moose Fed Com 604H. These enrichments or depletions in elements aid in interpretation of depositional conditions (Figure 23.).

		XRF_QTZ	XRF_ALB	XRF_ILL	XRF_CHL	XRF_KAO	XRF_CAL	XRF_DOL	XRF_PYR	XRF_BAR	XRF_FLP	XRF_RUT	XRF_HAL	
Chemofacies	1	44	0	10	1	0	40	3	2	0	0	0	0	100
Chemofacies	2	23	0	5	1	0	66	5	1	0	0	0	0	100
Chemofacies	3	24	0	13	0	0	12	47	2	0	0	0	0	100
Chemofacies	4	53	0	24	3	0	12	5	1	0	0	0	2	100
Chemofacies	5	47	0	18	2	0	22	8	1	0	0	0	1	100
Chemofacies	6	56	0	26	4	0	6	6	1	0	0	1	0	100
Chemofacies	7	50	0	27	4	0	11	5	2	0	0	1	0	100

Table 8, Summary of rock composition by chemofacies

6.1.4 Chemofacies Distribution

When compared to the general lithologies noted based upon elemental data, chemofacies can further subdivide the formation and show variations in depositional conditions across the study area (Figure 26.). The 3rd Bone Spring Sand is only located in three wells (Big Moose Fed Com 604H in the SW, and Toque State Com 602H and 601H in the northeast). Also, these were the "target" formation in horizontal wells, where these sections are horizontal. They represent spatial changes rather than changes through time. In the southwest (well Big Moose Fed Com 604H), chemofacies 4 is dominant, indicating a mixed siliceous mudstone deposited in fluctuating oxic to dysoxic conditions. In the northeast (wells Toque State Com 602H and 601H), the 3rd Bone Spring is dominated by chemofacies 6 and 7, indicating a mixed siliceous mudstone (chemofacies 6) deposited during oxic conditions with increasing clay content (chemofacies 7) deposited during fluctuations of anoxia.

The average RSTEs (U, Cr, Ni, Zi, V) increase in the Avalon, 2nd and 3rd Bone Spring Sand in the Big Stag Fed Com 503H, Big Stag Fed Com 703H, Big Bucks Fed Com 501H and the Toque State Com 601H. The relative increase can be seen in both map and cross section view. RSTE's correlate with higher TOC. The increase in the RSTE's indicative of higher TOC would also correlate well with the Mo/Ni plots shown previously where the wells with more restriction correlate with those with potentially higher TOC .

Given that there is a large potential for biogenic silica in the basin because of the

56

settling of sponge spicules it is important to review the Si/Zr ratio to gain insights into the source of silica. From work by Ratcliffe et al. (2012), biogenic and detrital silica can be differentiated using this Si/Zr ratio. For the Muskwa Formation in Canada a cross-plot of SiO_2 and Zr indicate a terrestrial trend of increasing SiO_2 with increasing Zr, and a biogenic trend with decreasing Zr with increasing SiO_2. The negative correlation is caused by an excess of Si due to an influx from biogenic sources. Parts of chemofacies 7, 4 and 6 exhibit some of this excess silica. In addition, the Zr/Al ratio is at its highest in the older 3rd Bone Springs sand sequence and then becomes increasingly lower i.e., finer grained up sequence to the Big Lime.
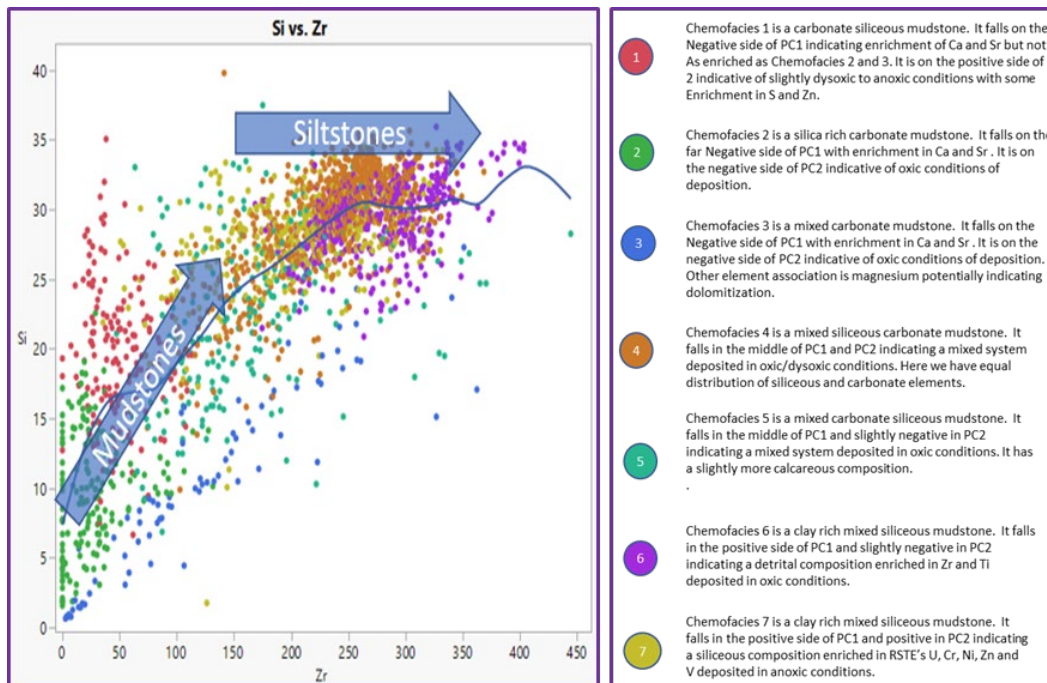
Figure 24, Biogenic silica proxies using the Si/Zr cross-plot coupled with Si/Al ratio to determine dstones and siltstones. Datapoints are color coded based upon chemofacies classification.
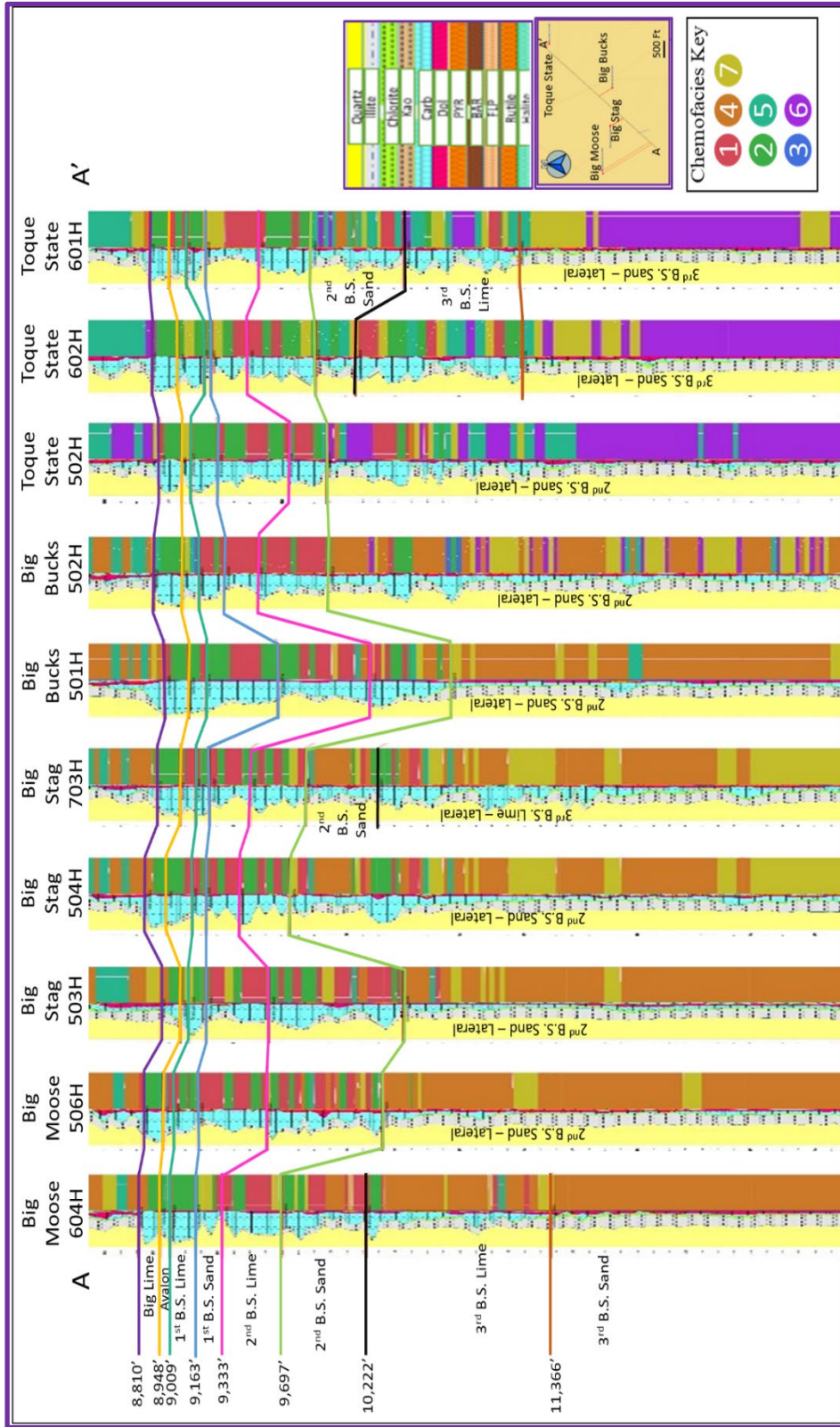
Figure 25, Cross Section Indicating change in chemofacies across the study area. Notable is the increase in detrital elements in the Toque State wells and the increase in Redox sensitive elements in the 2nd Bone Spring Sand members. Colors on right track of each log represent the chemofacies clusters coloring (see Fig 16). Middle track on each well represents changes from carbonate (blue) to siliciclastics (yellow) derived from Si and Ca compositions. The overlying Delaware group, Brushy and Cherry Canyon. Chemofacies 2,3 and 5 (Carbonate mudstones) are intercalated with chemofacies 4 (mixed siliceous mudstones) in these upper sequences.

58

The 3rd Bone Spring Lime is only found in the center of the study area (Big Stag Fed Com 703H). It too was the target formation, and this section is a lateral (horizontal well) representing horizontal changes in the vicinity. It consists of predominantly of chemofacies 4 and 7. There is slightly more argillaceous material and fluctuations of anoxia during time of deposition compared to the underlying 3rd Bone Spring Sand. This may indicate an increase in water depth to allow for increased clay deposition and anoxia.

6.1.5 Grain size

Zr/Al can be used to estimate grain size (Driskill et al., 2018), as Al is a proxy for clay in this system. Within the 3rd Bone Spring Sand, there are generally high Zr/Al ratios (Figure 28.), indicating coarser grain sizes. Up-section, the Zr/Al ratios continue to decrease, suggesting a grain size and composition decrease. The Avalon is an exception, with a slightly coarser grain size than the overlying Big Lime and underlying 1st Bone Spring Lime. Overall, the coarsest relative grains can be seen in the 3rd BSPG Lime and Sand. This would indicate an increasingly higher energy environment of deposition and shallower water conditions compared to the finer-grained sediments. The association with higher Ti would also indicate a detrital source. The Zr/Al ratio for the 3rd Bone Spring Sand is 56. Zr/Al ratio for the 3rd Bone Spring Lime is 55. Zr/Al ratio for the 2nd Bone Spring Sand is 44. Zr/Al ratio for the 2nd Bone Spring Lime is 26. Zr/Al ratio for the 1st Bone Spring Sand is 29. Zr/Al ratio for the 3rd Bone Spring Lime is 28. Zr/Al ratio for the Avalon is 35. Zr/Al ratio for the Big Lime is 28.

Figure 26, An example well showing Zr/Al and (Zr+Rb+Ti)/Al ratios indicative of relative change in grain size. Note a general coarsening in grain size with depth from the BSPG Lime through to the 3rd BSPG Sand. Generally, this is the trend within all the wells.

Geospatial maps of the RSTE's in ppm reveal an organic richness high in the Avalon in the northeast (Figure 28.). There is also relatively high organic richness in the 2nd BSPG sand in the southeast and in the 3rd BSPG Lime in the center west part of the study area. This is an indicator changing environments of deposition over time. The Avalon Northeast

would have had more stagnant lower circulation conditions which would have led to organic enrichment. Coupled with the Zr/Al maps, we can see a relative negative correlation between RSTE and grain size. The RSTE's are higher in the finer grained rocks and the RSTE's are lower in the coarser grained rocks. This would make sense geologically since the conditions of stagnant water with low circulation would be conducive to the deposition of fine-grained sediments. Coarser material requires higher energy and would not have the stagnant conditions conducive to organic enrichment. environment.
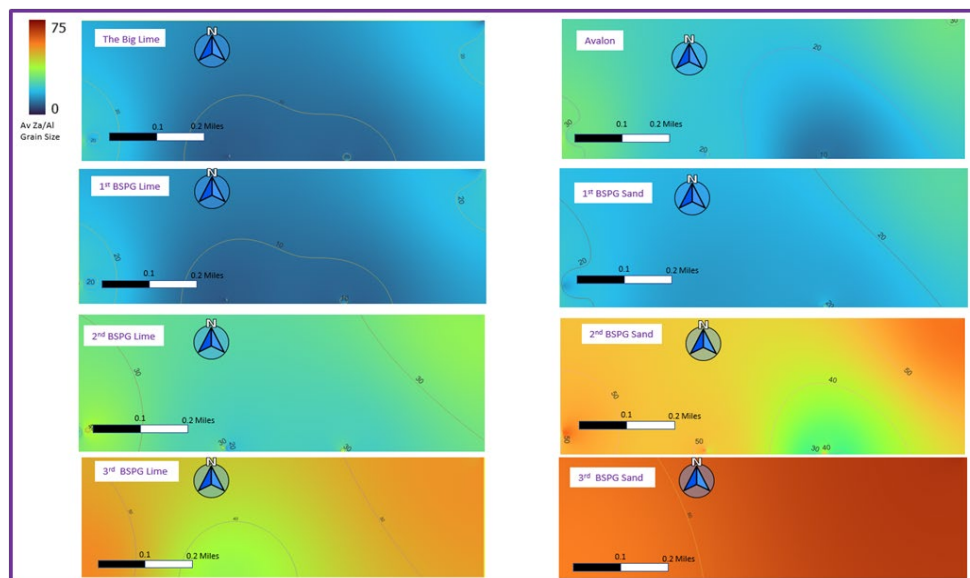
Figure 27, Average Zr/Al ratios (Grain size proxy) for the study area. Zr/Al ratios decrease from the 3rd Bone Spring Sand through the Big Lime, indicating a potential grain size decrease and or change in lithology. Also, the Zr/Alratios generally decrease towards the center of the study area for all formations, indicating reduction in detrital material through that area. This could indicate lower energy flow environment.
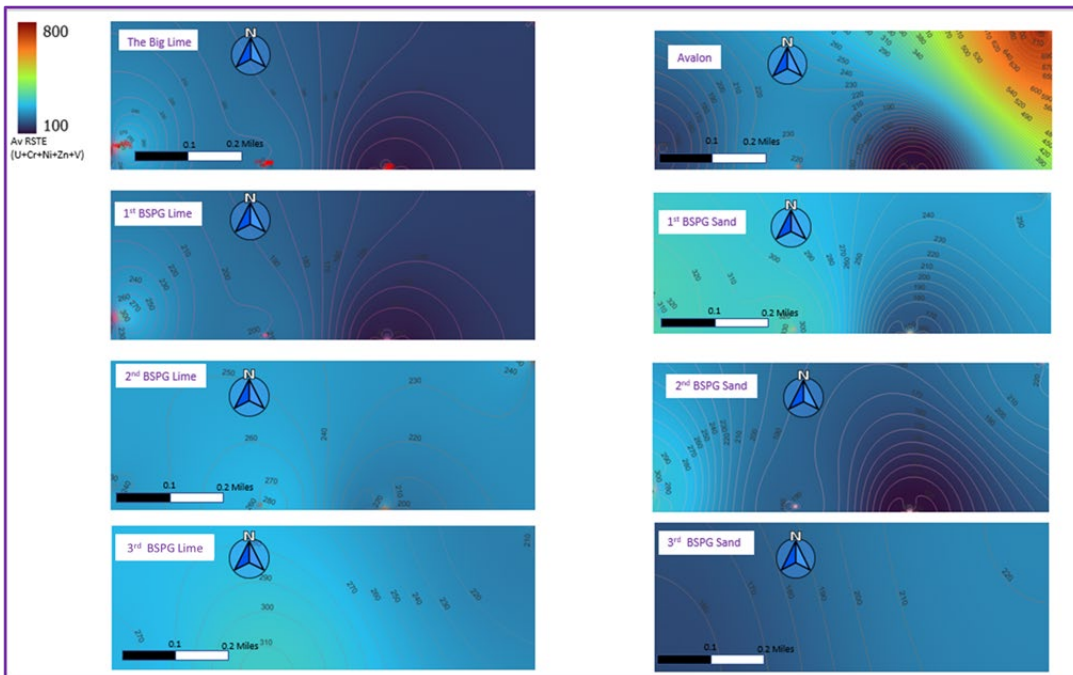
Figure 28, Map of Average RSTE's Redox Sensitive Trace Elements, (U, Cr, Ni, Zi, V) is highest in the Avalon in the northeast. RSTE's typically correlate with higher TOC

6.2 Petrophysical Analysis and Cuttings Comparison
6.2.1 Drill Cuttings depth QA/QC

Elemental gamma ray (EGR) from the drill cuttings were calculated from the addition of U+K+Th and compared to the MWD gamma ray. R^2 correlations between the EGR and MWD GR for Toque State 602H is 0.72 (Figure 30.). Overall, the Gamma Ray has a 0.3 m (1 ft) resolution and is much higher than drill cuttings, which are at an average of 18.2 m (60 ft), or 200 samples per 3,048 m (10,000 ft) of section compared to 1ft on downhole Gamma Ray. When a Gaussian smoothing of 18.3 m (60 ft) is applied an R^2 of 0.94 for 1st BSGP Sand can be observed. Elemental Gamma Ray correlates reasonably well with the MWD gamma ray providing indication that the cuttings collected are both representative of the section drilled at that measured depth.
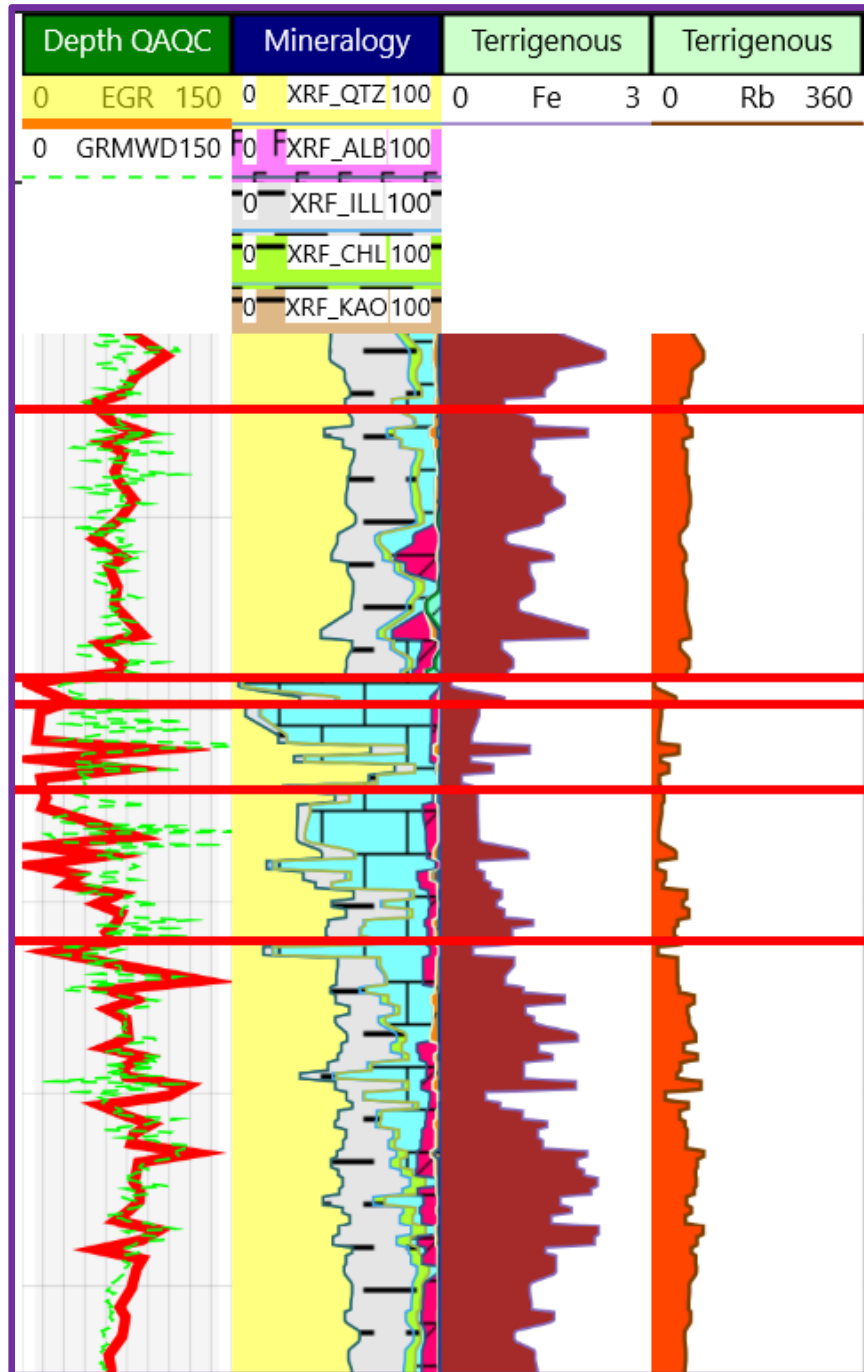
Figure 29, Example well of the calculated gamma ray curve in the Big Moose 604H well. Overall, there is good agreement with the cuttings data and well log data.

While the EGR is a combination of U, K, and Th, each element has insight into depositional and diagenetic conditions, and can dominate the EGR at various locations in a well. Uranium from wireline logs on the Big Moose 604H well compared to U measured on XRF drill cuttings for the section from the Big Lime down to the 3rd Bone Spring Sand returned R^2 of 0.36. Potassium from wireline logs compared to the K on XRF drill cuttings returned a regression of 0.45 for the section from the Big Lime down to the 3rd Bone Spring Sand. Thorium from wireline logs compared to Thorium on drill cuttings returned an R^2 of 0.46 for the section from the Big Lime down to the 3rd Bone Spring Sand (Figure 31 & Figure 32.).
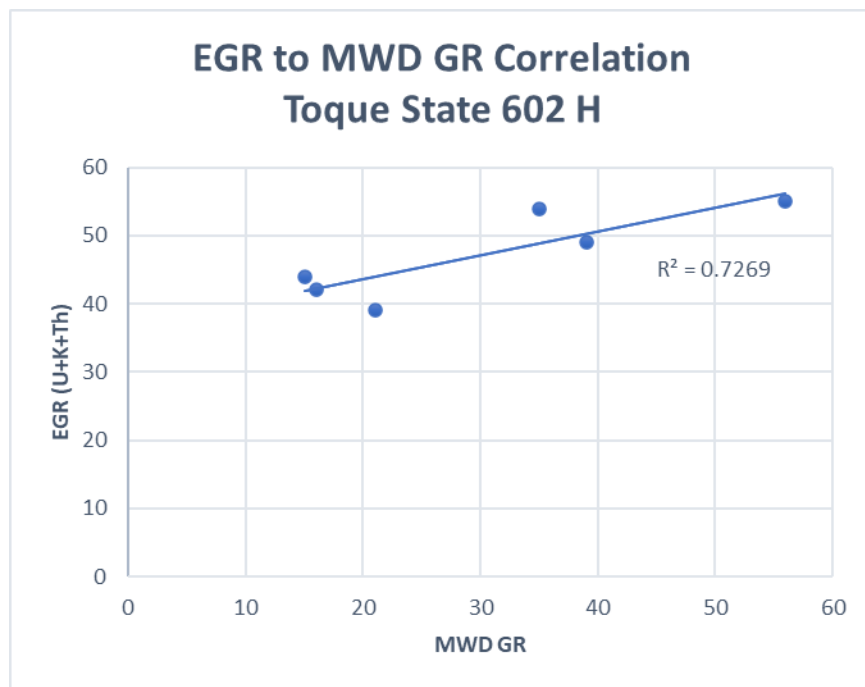
Figure 30, Average GR values vs MWD for Toque State 602H.
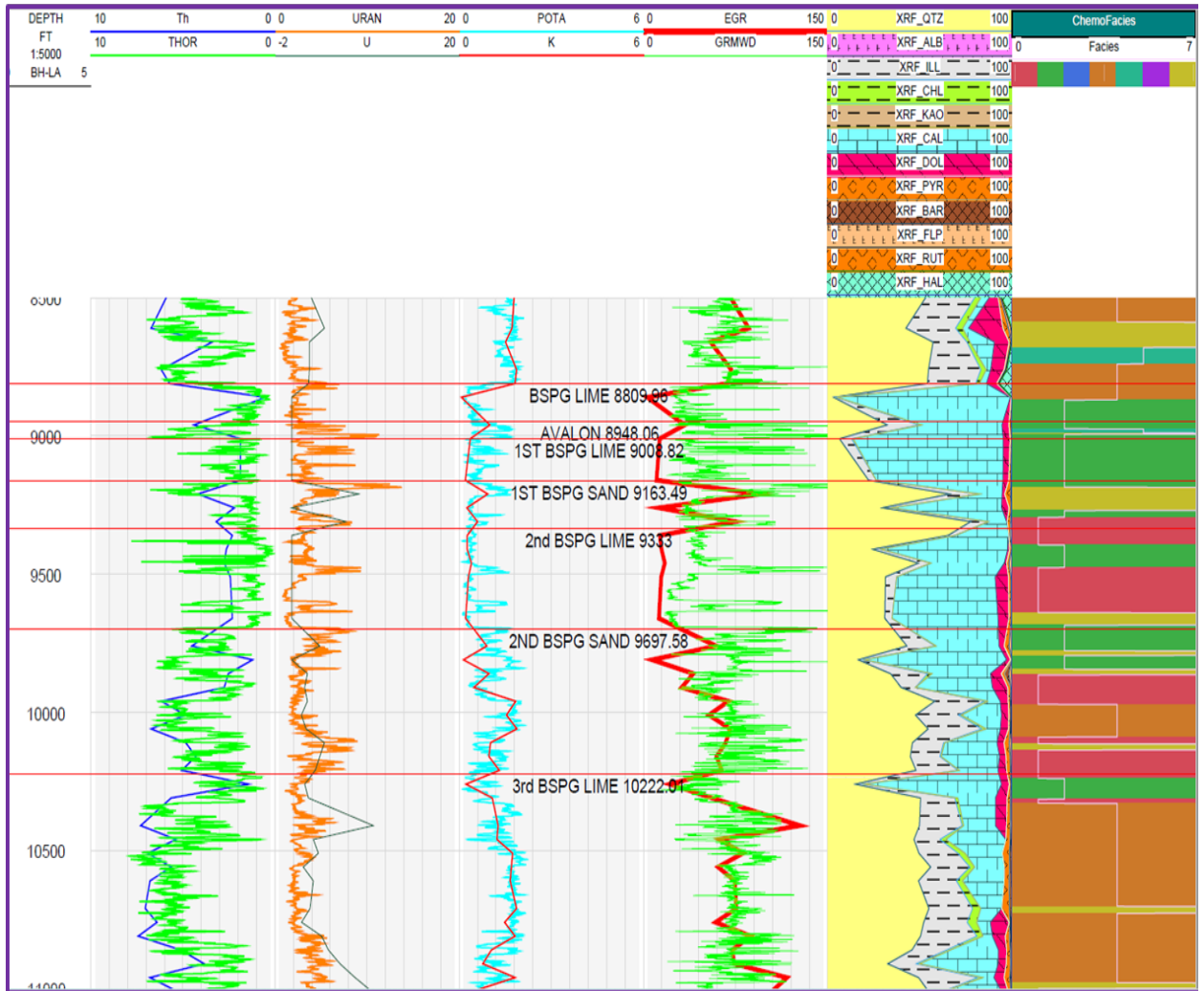
Figure 31, Comparison of the Uranium, Potassium, and Thorium wireline Logs to the U, K, and Th from The elements from XRF drill cuttings. Overall good visual correlation between the elements. Big Moose 604H well. The Th and the K from the XRF elemental data exhibit a good match throughout the sequence. The correlation improves in the siliclastics compared to the carbonates. The Uranium does not correlate well in the carbonates.
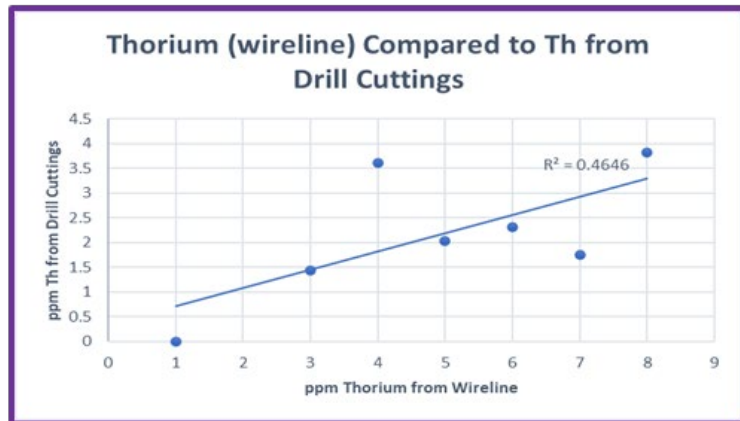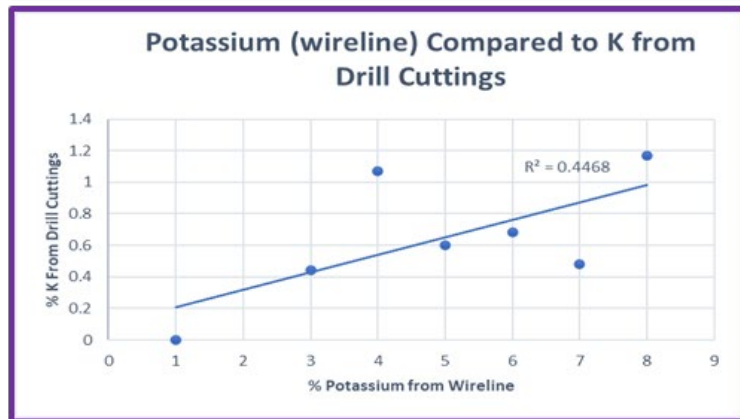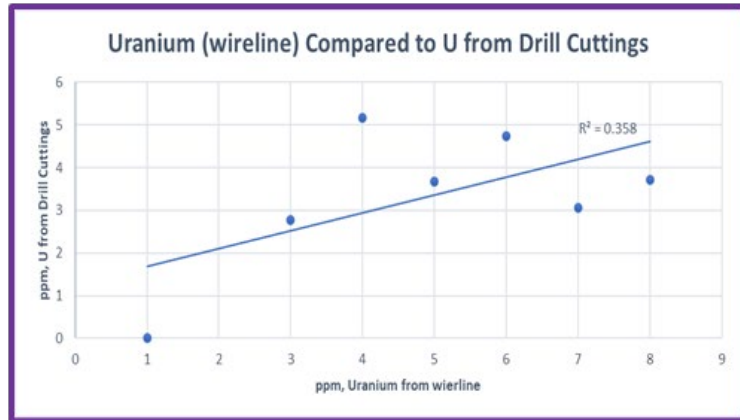
Figure 32, R^2 for U, K, and Th compared to wireline logs.

Visually the correlation appears better than the statistical R^2 for each element. The

reduction in correlation can be largely attributed to the difference in sample depth

density. The lower correlation from the Uranium can be attributed to low U readings in

the carbonate sections from the drill cuttings.

6.2.2 Mineralogy

The mineralogy derived from the XRF elemental mineral model was compared with the mineralogy generated by the Haliburton GEMS wireline logging tool. This was only done for the Big Moose Fed Com 604H well because it was the only well with a full suite of wireline logs provided (Figure 33.). The petrophysical mineralogy model is based upon known responses of the well logs, coupled with user inputs based upon the local geological formations. Overall, the two models can adequately determine similar ratios of clastics (sand) to clay content to carbonates. Note that both models exhibit highest levels of carbonate in the Big Lime and 1st Bone Spring Lime. As depth increases the carbonate composition reduces as the sand and clay contents increase. There are sections in the 2nd Bone Spring Sand and Lime where the well log mineralogy models greater amounts of dolomite. This could imply the XRF mineral model is apportioning too much magnesium to the clay. The XRF mineralogy model agrees with the petrophysical model in the Bone Spring Formation. Ca is normally concentrated in carbonate minerals, particularly calcite. Si may be linked with a variety of minerals but is most associated with quartz. Based on this, the silica and calcium ratios have been used in this study to understand the principal changes from siliciclastics deposits to carbonate deposition. The cyclicity which has been observed on well logs from previous studies (Carr, 2019) can be seen in this study. The carbonate deposition has been linked to transgressive high stand depositional environments and the siliciclastics linked to low stand regressive sea, level depositional environments. Stepping through the section we can see siliciclastics

67

predominate in the 3rd Bone Spring Sand. Carbonates predominate in the 3rd Bone Springs Lime. Siliciclastics are higher in the 2nd Bone Springs 2nd and the carbonate increases in the 2nd Bone Spring Lime. The siliciclastics reappear in the 1st Bone spring sand and the carbonates in the 1st Bone Spring Lime. The Avalon is both silica and carbonate rich and the Big Lime has higher carbonate composition. There is a general increase in Ca/Si ratio from oldest to youngest in the sequence.

Figure 33, Mineralogy derived from an Elemental Capture Spectroscopy wireline tool compared to mineralogy derived from XRF elements measured on drill cuttings at an average 50 Ft. interval for the Big Moose Fed Com 604H well.

6.2.3 Geomechanical Properties Comparison with Sonic Logs

The Brittleness Index (BI) was calculated in the Big Moose Fed Come 604H using

the XRF data and compared to the sonic log (Figure 36.). Again, this was the only well that had a full suite of wireline data. Regression for the sonic log comparison to the XRF Brittleness Index returned a value of 0.59 (Figure 38.). There is a very good correlation in the carbonate rich sections. In the siliciclastics, there appears to be an underestimation of the competence compared to the sonic. This may indicate that the estimation of the quartz in the XRF mineral model could be slightly underestimated also. This BI was then applied to all the wells. The BI was highest in the older rocks in the sequence i.e., highest in the 3rd Bone Spring sand and becoming increasingly more ductile up to the Big Lime. In general, the siliciclastic-rich sequences exhibit the highest BI and therefore geomechanical competence.

BI for the 3rd Bone Spring Sand averaged 57, 3rd Bone Spring Lime averaged 45, 2nd Bone Spring Sand averaged 49, 2nd Bone Spring Lime averaged 39. The Brittleness Index BI for the 1st Bone Spring Sand averaged 49, 1st Bone Spring Lime averaged 26, 2nd Avalon averaged 22, and Big Lime averaged 17. Overall, the rock competence increases with depth and is geomechanically more competent in the siliciclastics rocks compared to the rocks with higher carbonate content. This seems to be linked to the quartz content throughout the formations, rather than the calcite content.

The BI is also reflected in the chemofacies. Chemofacies 2 appears to consistently have higher sonic values and BI, indicating that it is a more brittle rock compared to other chemofacies. It consists primarily of 65% calcite, 22% quartz 5.5% Illite and 4.5% dolomite. Conversely, chemofacies 4 appears to consistently have lower sonic values and BI,

indicating a more ductile formation, consisting of 27% Illite, 52% Quartz, 12% Calcite and

4.75% Dolomite and 1% Pyrite.
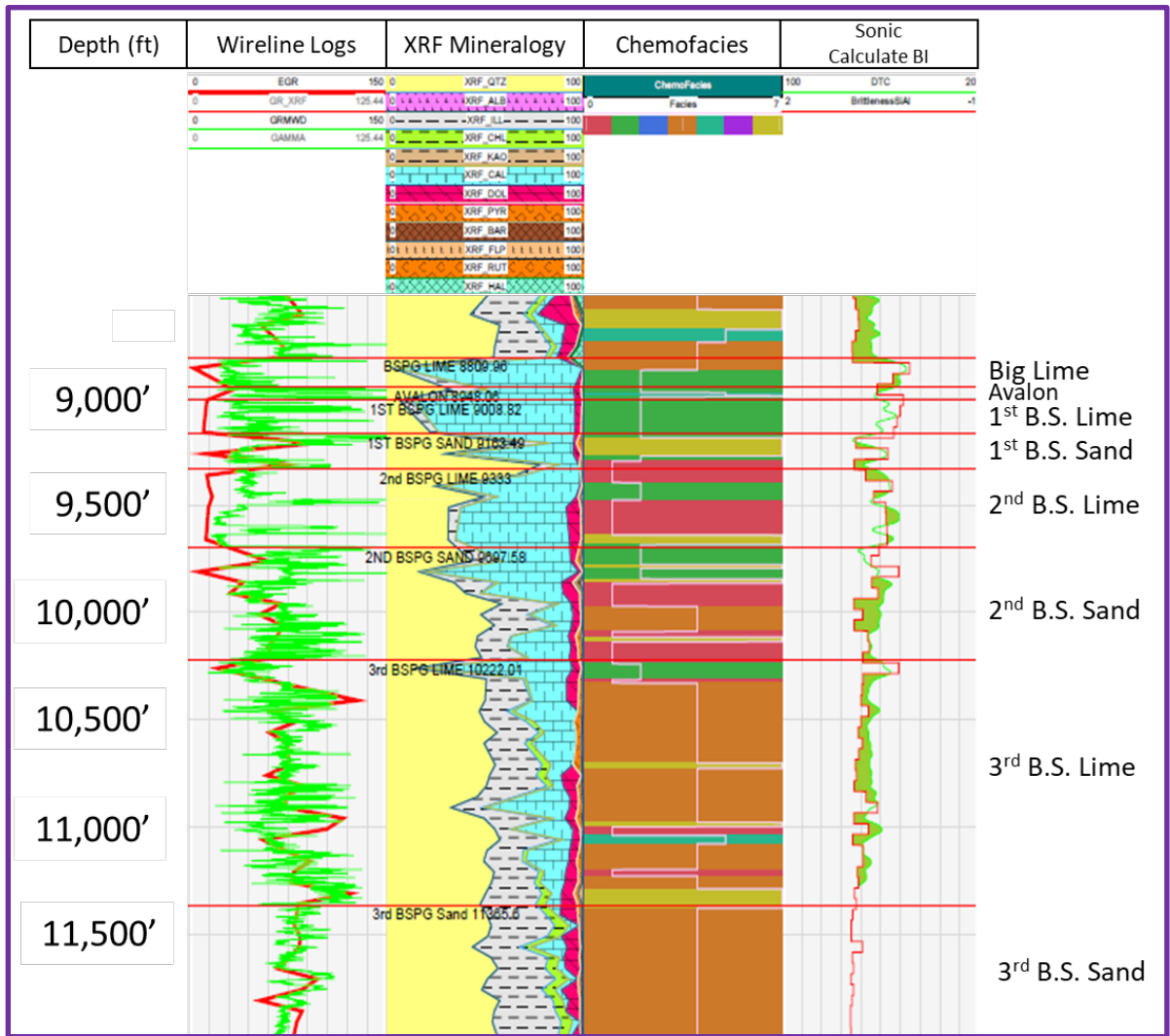
Figure 34, Example of the comparison of DTC sonic Log and Brittleness Index from XRF elemental data in well Big Moose Fed Com 604H (Track 5). The green filled in area shows the difference between the Sonic Log and calculated BI.
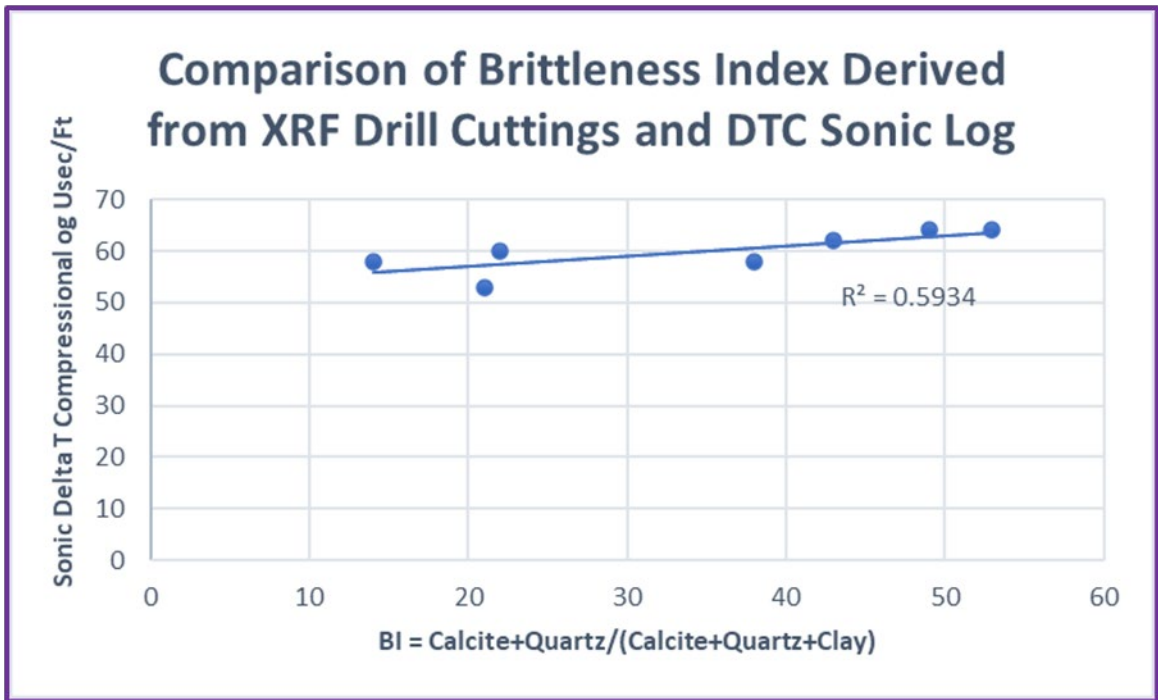
Figure 35, Cross plot of the BI vs Sonic Log (DTC

6.2.4 XRF Mineralogy Comparison with Volume of Clay (V_{clay})

V_{clay} calculated from the Gamma Ray was compared with the Elemental Gamma Ray (U+K+Th) from the cuttings (Figure 36.). Given overall good correlation between the MWD GR and EGR, the Vclay follows similar positive correlation trends. There is greater offset in the carbonate rich sequences. There is the greatest positive correlation in the siliciclastic sequences, in particular, the 2nd and 3rd Bone Spring Sands. This could be due to mineralogy effects on the downhole tool response. For example, potassium-rich sand would have a high GR and lead to perhaps misinterpretation using a standard Vshale cut

off, resulting in bypassed pay. It may also be an artifact of drilling, drill rates and sample resolution. On the K, U and Th plots there appears to be an underestimation in Uranium from the XRF data, particularly in the carbonates, or overestimation on the downhole logs.
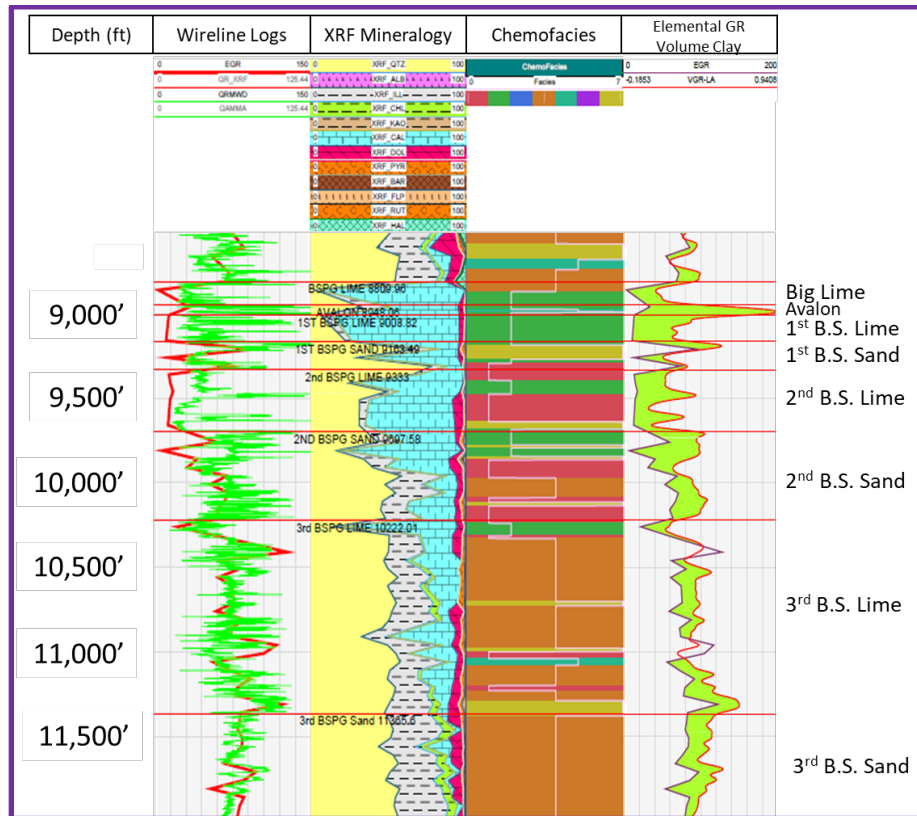
Figure 36, Example of the clay volume calculated from GR and compared to EGR (U+K+T). The area highlighted in green shows the difference between the XRF clay calculation and the Vclay calculation from the gamma ray. Well Log from Big Moose 604H.

6.2.5 Comparison with TOC from Logs

TOC was calculated from the resistivity and density logs using the Passey method, and compared the redox sensitive elements (Ni, V, U) (Figure 37.). This was only

completed on the Big Moose Fed Com 604H well because it was the only well with a full suite of well log data. Overall, all the three paleo-redox proxies exhibit positive correlation with the wireline log derived TOC. Figure 38 indicates an R^2 of 0.29 for the RSTE's compared to Log derived TOC using Resistivity and Density using the Passey method. The low correlation R^2 between the paleoredox proxies and the log dervied TOC can be attributed to the differences in depth resolution nevertheless the low correlation should result in using these proxies with some caution.

The RSTE's were calculated for the other nine wells to show TOC variations across the study area and compared to the chemofacies. Note the increase in chemofacies seven (anoxic to sub-oxic siliciclastics enriched in RSTE's (U, Cr, Ni, Zn and V) in the 2nd Bone Spring Lime and 2nd Bone Spring Sand.
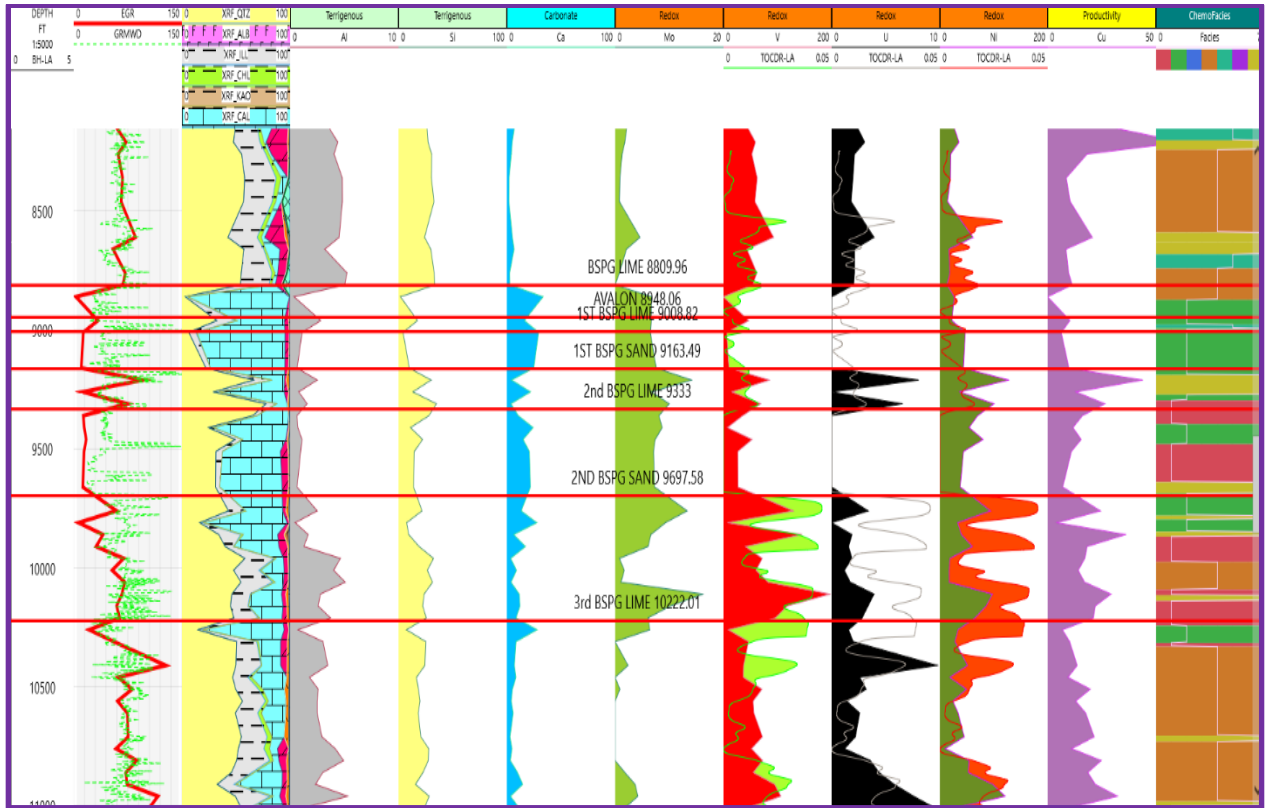
Figure 37, Comparison of log derived TOC from Resistivity and Density Logs and compared to drill cuttings XRF Paleo redox proxies of V, U and Ni for the Big Moose Fed Com 604H well.
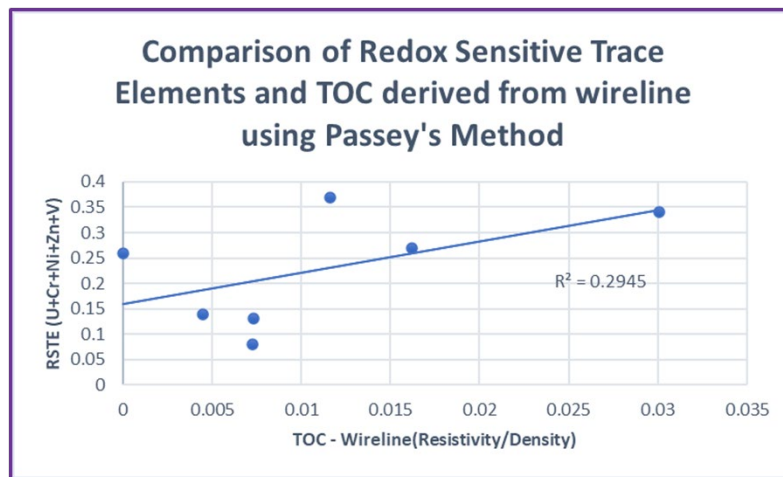
Figure 38, TOC Comparison of TOC calculated from the resistivity/Density logs (Passey Method) compared to the TOC using (U+Cr+Ni+Zn+V) (Paleo-redox Proxy). R^2 of 0.29.

The RSTE for the 3rd Bone Spring Sand is 199. The RSTE for the 3rd Bone Spring Lime is 250. The RSTE for the 2nd Bone Spring Sand is 232. The RSTE for the 2nd Bone Spring Lime is 267. The RSTE for the 1st Bone Spring Sand is 312. The RSTE for the 1st Bone Spring Lime is 229. The RSTE for the Avalon is 343. The RSTE for the Big Lime is 142. The most organic rich zone is the Avalon, followed by 1st Bone Spring Sand. The leanest formation in organic richness is the Big Lime. In the Avalon, the Toque State wells in the northeast have the highest RSTE values of Toque State 502 (RSTE 789), Toque State 601 (RSTE 621) and Toque State 602 (RSTE 504).

7. DISCUSSION

7.1 Chemofacies to Lithofacies Comparison

Cuttings-based XRF measurements have been able to determine variations in the trace element composition across the study area. Within the Bone Spring Formation, seven chemofacies were determined using the cuttings, which described not only the basic lithology, but also gave indication into the depositional environment. For example, chemofacies 4, 6, and 7 have similar lithologies on the S-Core ternary diagrams (Figure 22.), suggesting clay-rich siliceous mudstones through mixed siliceous mudstones. However, these three chemofacies have varying RSTE's (Table 9). These variations in the average RSTE's indicate variations in redox conditions. Chemofacies 4, although very similar in average bulk element composition to chemofacies 6 and 7, is depleted in V and Ni, has average Zn and Mo, and slightly elevated U values compared to standard shale values as per (Wedepohl, 1971; Tribovillard et al., 2006) (Table 9).

The relative depletion of vanadium could be attributed to strongly reducing or euxinic environments of deposition. The presence of free H_2S produced by bacterial sulfate reduction causes V to be further reduced to V^{3+} which can be absorbed by geoporphyrins or precipitated as the solid oxide V_2O_3 or hydroxide $V(OH)_3$ phase (Craigie, 2018).

The relative enrichment of uranium occurs within the sediment, not the water column, so the oxygen penetration depth and the sedimentation rate may be significant.

77

A slower sedimentation rate, for instance, may enable more time for the diffusion of uranyl ions from the water column into the sediment (Crusius and Thompson 2000).

Craigie (2018) describes that the release of Zn to pore waters and the overlying water column may take place upon organic matter decay. The element may be incorporated as sphalerite ZnS as a solid solution phase in pyrite or, to a lesser degree, it may form its own sulfides, these processes occurring under anoxic conditions (Tribovillard et al., 2006). Molybdenum enrichment most probably occurs in association with a concentration in pyrite sediments deposited in anoxic environments, though the possibility of some being associated with organic matter should not be ignored (Craigie, 2018). The exact origin of molybdenum can be difficult to determine, however the association between this element and anoxic paleoenvironments has been observed in many studies (Craigie, 2018; Algeo and Tribovillard, 2009; Driskill et al., 2018).

Table 9, Average bulk and RSTE's for chemofacies 4, 6, and 7 compared to the average shale values.

Average	Si (%)	Ca (%)	Al (%)	V (ppm)	Ni (ppm)	Zn (ppm)	Mo (ppm)	U (ppm)
Chemofacies 4	29.4	4.52	4.36	40.5	23.1	62.5	3.26	3.37
Chemofacies 6	29.6	3.13	4.43	74.4	22.1	40.5	0.15	1.85
Chemofacies 7	27.8	4.95	4.59	85.3	54.1	156.7	6.74	4.27
Average Shale*	27.5	1.6	8.8	130	68	95	1.3	3
* From Wedepohl (1971) and Tribovillard et al. (2006)								

7.2 Chemofacies and depositional environment

Under oxic conditions, organic matter is broken down by methanogenic bacteria via an oxidative-reductive disproportionation of carbon (Tribovillard et al., 2006). Oxygen depleted conditions, and ultimately anoxia, may occur at the sediment-water interface or within sediments when the oxygen demand exceeds the supply. Anoxia may also develop in the water column of stagnant or confined water masses where there is a lack of circulation, or in places where intense organic matter degradation consumes O_2 faster than it is replenished, even in open-marine conditions. High levels of Mo, Cu, Co, Ni, Zn, Cr, U and V are often associated with anoxic paleoenvironments, and it may be possible to identify sediments deposited under these conditions where values of these elements exceed their average (Craigie 2018).

It has previously been shown that the RSTE's in the Bone Spring Formation can be directly linked to TOC (Driskill et al., 2018). Mo to Ni ratios can indicate a more restrictive flow environment based on work conducted by Algeo and Lyons (2006). Ni as a proxy for TOC and plotted against Mo. The 3rd Bone Springs Sand is predominantly more siliceous material (Chemofacies 4), indicating a low stand regressive sea-level depositional environment.

Notwithstanding, there are changes across the study area. The southeast area (Big Moose) has less detrital Zr and Ti than the northeast area (Toque State), which has more of chemofacies 6. This could indicate some localized silica-rich hemi-pelagic terrigenous

gravity flows. Fault orientation in the area primarily is in a NW-SE direction,(Figure 39.),

and this could also be influencing the change across the area, which is abrupt given the

small distance. It could also be a localized channel flow. The 3rd Bone Spring Lime in the

northeast section of the study area indicates a mixed system with chemofacies 1,2,5 and

7 which are an indication of higher levels of carbonate deposition and oxygenation. This

could be indicative of a calcium-rich hemipelagic sediment gravity flow.

The 3rd Bone Spring Lime in the southeast study area contains less carbonate and

is more silica rich. This is more indicative of a silica rich hemipelagic sediment gravity flow.

The 2nd Bone Spring Sand in Big Moose in the southeast is enriched in chemofacies 4 and

7 and increases in chemofacies 7 towards the center of the study area (Big Stag and Big

Bucks). This would indicate an increase in anoxia towards the center, indicating a more

stagnant, lower circulation depositional environment. The Bone Spring Sand towards the

NE becomes more "limey". This would indicate a potential carbonate-rich sediment

gravity flow coming into this area.

The 2nd Bone Spring Lime is enriched in chemofacies 2, 1, and 7 interbedded, with

increased 2 towards the NE again indicating a more carbonate-rich influence in this area

also indicating potential carbonate gravity flow input. There are fluxes and pulses of

interchanging chemofacies 2 and 7, indicating changes from siliciclastics to carbonates

over time. The 1st Bone Spring Sand is interbedded with chemofacies 1, 3 with some 7 –

carbonates with periods of anoxia with increased anoxic siliciclastic input. There is a slight increase in anoxia chemofacies 7 to the northeast.

The 1st Bone Spring Lime is enriched with chemofacies 2 and 3, i.e., predominantly carbonate with periods of anoxia represented by chemofacies 7. The Avalon formation is a mixed system with chemofacies 1 and 2, carbonate floating between oxic to anoxic conditions, and siliciclastic input towards the northeast. This siliciclastic input is also anoxic chemofacies 7 in the Toque State 602H, which drives up the average RSTE's in this area. The Big Lime is predominantly chemofacies 2, calcite rich and deposited in an oxygenated, higher circulation depositional environment. This would correlate to chemofacies 1,3 or 8 in Walkers (2021) study, i.e. a calcium-rich hemipelagic gravity flow lime mudstone to packstone.(Figure 43.).
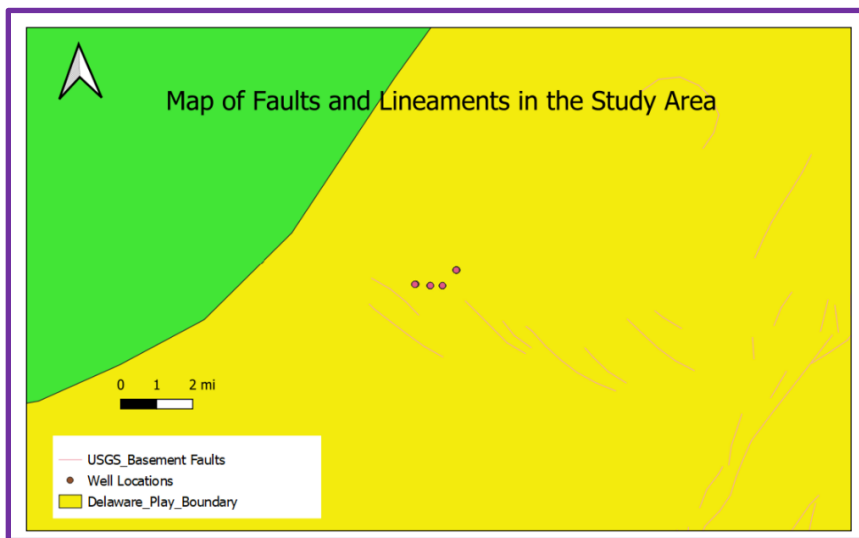
Figure 39, Map of Study area with basement lineament faults care of USGS.
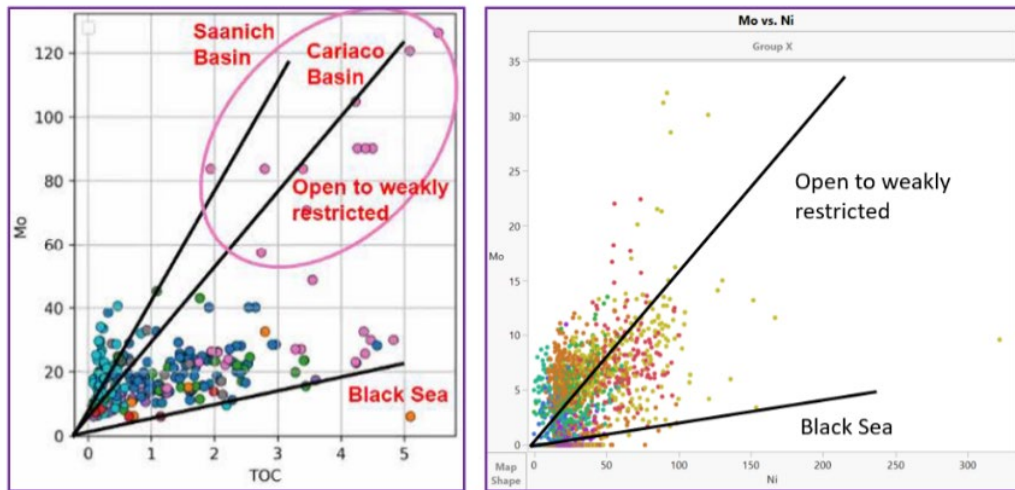
Figure 40, Molybdenum over TOC has been used to estimate depositional environment (Algeo and Lyons, 2006). The scatter plot to the left is from modern day analogs including the Black Sea, the Cariaco and Saanich basins. The scatter plot to the right is the data from the study area. Most of the data points fall within the open to weakly restricted area. With it being a mixed system it is difficult to resolve the depositional environents using these plots. Nevertheless chemofacies 5 does appear to be indicative of a more open circulatory environment compared to the other facies.

7.3 Core Studies vs. Cuttings Analyses.

Unfortunately, this study could not directly describe the cuttings to obtain general

lithologies across the study area, which would have aided in lithofacies interpretation,

this due to the cuttings being unavailable. Previous work done by Walker (2021) in the

Bone Spring Formation based on measurements of outcrops in the Guadalupe

mountains revealed a direct relationship between chemofacies and lithofacies related to

the change in depositional setting. The same ratio plots have been applied to the data

set in this study to draw potential parallels to this ground truth data set.

 Lithofacies 6 from (Walker, 2021)(Figure 41.) indicates deposition of a silica-rich

mudstone as a hemipelagic sediment gravity flow. This lithofacies appears to be similar

to chemofacies 4,6 and 7 based on the Ca/(Si+Ti) plots (Figure 44.). Lithofacies 1 and 2

from Walker (2021), which are Ca-rich hemipelagic sediment gravity flow deposits,

correlate well with chemofacies 1,2 and 3 in this study. Facies 6 and 7 from (Walker,

2021) correlate with facies 4,6 and 7 from this study. This lithofacies is a thinly bedded

laminated bioclastic quartz siltstone and thinly bedded quartz lime mudstone. These are

therefore interpreted to be silica-rich hemipelagic sediment gravity flows. The changes

in chemical facies and their associations thus provide evidence of relative seal level

change and glacio-eustasy as we move from carbonate rich (Ca, Sr) elements to

siliciclastics (Si, Rb, Ti, Al, Zr).
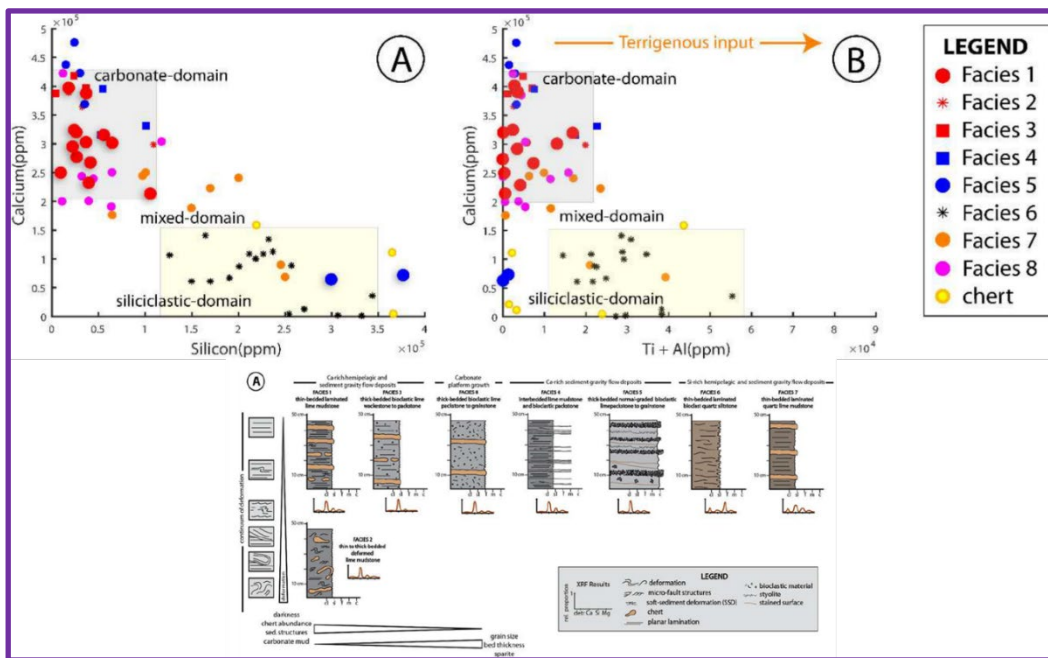
Figure 41, This is a figure from Wylie 2021 in which you can see the relationship between XRF data obtained from Outcrop in the Gudaloupe mountains. He has identified 8 facies and compared the XRF signatiures to those facies. He chose 4 main XRF data groupings, detrital, si, al and mg.
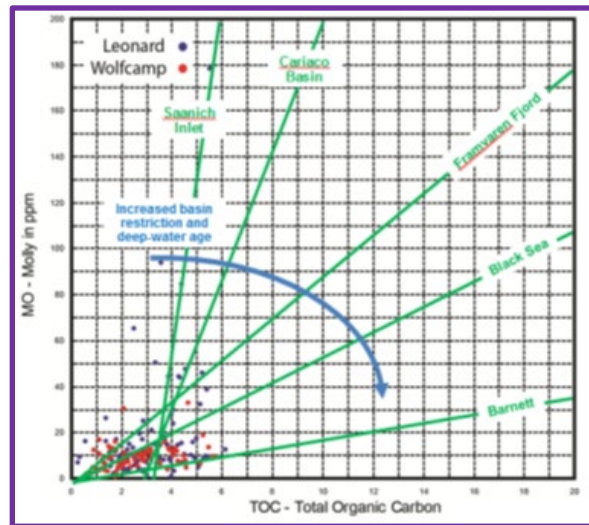
Figure 42, Molybdenum versus TOC cross-plot showing Wolfcamp and Leonard samples from the Greer 1 core in relation to several analogs. Blue arrow depicts an increase in basin restriction and deep-water age. From Cortez (2012).

Overall, using cuttings to determine chemofacies provided an adequate evaluation of the chemostratigraphy of the area. The limitation of drill cuttings analysis is primarily related to low depth resolution of sampling (on average 50 ft/17m). The implications of this are the inability to see fine scale changes in lithologies and facies. By studying outcrop, core and logs, we can see changes over cm scales;thus, cuttings-based studies can miss large sequences of important information. An additional challenge in this study area is the mixed nature of the lithofacies. A combination of sea level change, tectonism, and extraterrestrial influences (Milankovitch cycles) make this system complex and difficult to interpret. Nevertheless, broad changes in facies carbonate, siliciclastics, and argillaceous changes can be seen using chemofacies interpreted from XRF analysis of drill cuttings. The carbonate facies is characterized by high levels of Ca, Sr and Mg. The argillaceoud facies

is enriched in Si and Al. The Siliceous facies is enriched with Si and Al with higher levels of Si than the argillaceous facies. Detrital facies are characterized by an increase in Zr and Ti. Subdivision of these facies when linked to core and outcrop studies can lead to further estimations of changes in depositional environments and gravity flows (Stolz et al., 2015). Figure 43 represents a depositional Model of the Delaware Basin during Leonardian Time. The Toque State 3rd Bone Spring Sand is enriched In detrital elements namely Zr, also with increased Si, Al, Rb, indicative of being derived from a Si rich hemipelagic sediment gravity flow. This would match with (Walker's 2021) chemofacies 6. The Big Moose 3rd Bone Spring Sand laterals by contrast is a thin bedded laminated bioclast quart siltstone derived from a Ca rich hemipelagic sediment gravity flow as can be seen represented as a debrite flow. The Big Stag and Big Bucks 2nd Bone Spring laterals have higher RSTEs indicative of anoxic low energy depositional environments. They are enriched in (Walker's 2021) chemofacies 7. 1st , 2nd & 3rd BSPG Lime depositional environment would have been on the carbonate fringe of the basin during highstands. 1st , 2nd & 3rd BSPG sands would have been deposited in the organic, pelagic, siltstone, mudstone setting. The Avalon with enriched organic content and clay would have been a lower energy and potentially more distal setting.
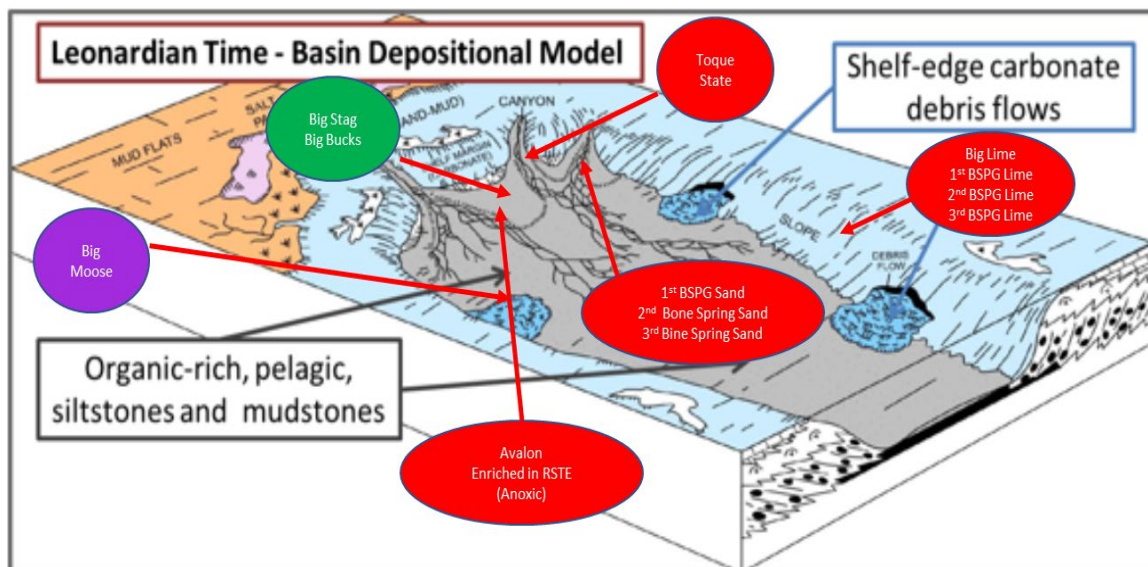
Figure 43, Depositional Model of the Delaware Basin during Leonardian Time. Characteristic depositional processes of the time include carbonate debris origination above the basin floor, and deposition of organic, pelagic siltstones and mudstones out onto the basin floor (modified from Loucks et al., 1985).

Ultimately, although inorganic elemental analysis is a powerful tool, the analysis itself is highly interpretive and, if used as the sole dataset, it can be highly subjective (Ratcliffe et al., 2004), (Craigie, 2018). Additional and preferred data sets would be core data, wireline log data on all wells, special core analysis, petrography and seismic.

Figure 44, Ca/Si and Ca/(Si+Ti) plots, associations exist between Walker 2021's chemofacies from outcrop and chemofacies derived from drill cuttings.

7.3 Practical implications

Chert zones can result in hard drilling, bit wear, tool failure, and non-productive drilling time. Identification of excess silica could provide input and assistance to improve drilling efficiency and performance. Near real time data being delivered within 2-30 minutes arriving at the surface could provide this drilling advisor input. Elemental chemostratigraphy can be used as an independent stratigraphic positioning tool and

therefore could be used for GeoSteering purposes. Scripts or formulas of these facies could be used and programmed into real-time GeoSteering software to predict wellbore position. In addition, the geomechanical data from the brittleness index BI and the chemofacies could be used to optimize completion design where stages can be linked to chemofacies, and this produces a frac recipe that is appropriate for each rock type. Big Stage Fed Com 703H for example, was initially classified as a Wolfcamp A well, but later review recategorized the well as a Lower 3rd Bone Spring Lime well. Using an extensive elemental data set can reduce the geological uncertainty and ensure that wells are drilled and geosteered in their target. Many have written that the key to unlocking unconventional resource plays is encountering the so-called Goldilocks rocks,the rocks that are just right. The combination of geomechanical competence (frackability) (BI), the organic richness indicative of the presence of hydrocarbons in the rock (RSTE), and the rock composition tied to core-based porosity and permeability (chemofacies) from drill cuttings can lead to this understanding. The author is deploying a patented robotic logging system that can analyze the elemental rock composition every 2minutes while drilling to further push this envelope and explore the boundaries of possibilities.

8. CONCLUSIONS

Drill cuttings provide an important source of information for the geoscientist. XRF elemental data is a robust data set that can be collected relatively inexpensively and efficiently in the field while drilling or post well in the lab. The use of calibration rock standards (SDC) and comparing EGR to MWD GR at frequent intervals is an important part of the QA/QC process. Overall, the following can be concluded from this study:

Geospatial mapping of the chemofacies can lead to a greater understanding of changes in facies both laterally and over time. Here, they were able to showcase where increased RSTE enrichment or depletion occurred, and increased grain sizes are distributed across the region. In this study area the northeast corner had enrichment in RSTE in the northeast during the Avalon formation deposition. Through time the Zr/Al and BI index increased from the Big Lime through to the 3rd Bone Springs sand. The detrital elements Zr and Rb were increased in the northeast in the Toque state wells in the 3rd Bone Spring Sand.

Calibration to wireline logs, XRD, pyrolysis and other reservoir quality indicators are an important part of the model building process. The more rigorous this stage of the work, the better the modeled interpretation. The calculated reservoir properties were compared to petrophysical analyses to see if correlations exist between either widely used petrophysical calculations or well logs. This study has demonstrated some of the

relationships that exist between wireline log property measurements and that which can be derived from drill cuttings with XRF measurements.

Geochemical elements can be used to understand changes in lithology and the environment of deposition. The volume of clays can be loosely estimated using Illite composition. TOC can be estimated utilizing paleo redox proxies, although more calibration is required through direct pyrolysis measurements. Geomechanical rock properties can be estimated using a brittleness index derived from elemental rock compositions. Mineralogy can be estimated using stochiometric mineral models.

Seven chemofacies were assigned to elemental cuttings data from ten study wells based on Principal Component Analysis (PCA) and Hierarchical Cluster Analysis (HCA) cluster assignments to show periods of similar depositional conditions across the region. The chemofacies were linked to lithofacies to improve understanding of the influence of glacio-eustasy and tectonic events in the rock formation. This has been achieved by working on the assumption that siliciclastics (Si, Al, Rb) predominate in lowstands and carbonates (Ca, Sr and Mg) in highstands. Linking outcrop studies chemofacies with XRF drill cuttings chemofacies provides further insights into carbonate and siliciclastic hemipelagic sediment gravity flow conditions.

The utility of cuttings data for chemostratigraphy studies by comparing this study to previous core and outcrop studies has been outlined Cuttings have a lower resolution (typically 18.2 m (60 ft) sampling intervals), compared to core or outcrop where an entire section could be observed. The extrapolation of findings from core-based studies to this

drill cuttings study, particularly regarding the prediction of reservoir quality requires further work.

Future work could include more integration of cuttings, core data and petrology (thin sections and SEM work) with porosity and permeability measurements to utilize the chemofacies as a predictor of reservoir quality and to improve the correlations with lithofacies. In addition integration with seismic.

9. REFERENCES

Blakey, R., Deep time maps™ paleogeography, 2016.

Blakey, R., 2020, Deep Time Maps. https://deeptimemaps.com/greater-permian-basin/.

Baumgarder, R.W., and Rowe, H.D., 2017, Using Hierarchical Cluster Analysis to Improve Facies Definitions in Permian Mudrocks (Wolfcamp and Lower Leonard), Midland Basin, Texas. Search and Discovery Article #41986. Adapted from poster presentation give at AAPG 2016 Annual Convention and Exhibition. Calgary, Alberta, Canada. June 19-22, 2016.

Bievenour, A., and Sonnenberg, S., (2019), "Reservoir Characterization of the Bone Spring and Wolfcamp Formations, Delaware Basin, Ward County, West Texas," SEG Global Meeting Abstracts : 891-906.https://doi.org/10.15530/urtec-2019-633

Carr, D. L., 2019, Stratigraphic Architecture of the Bone Spring Formation (Leonardian), Delaware Basin, New Mexico and Texas: An Interim Report." Paper presented at the SPE/AAPG/SEG Unconventional Resources Technology Conference, Denver, Colorado, USA, July 2019. doi: https://doi.org/10.15530/urtec-2019-645

Cohen, D. and C.R. Ward, 1991. Sednorm – a program to calculate a normative mineralogy for sedimentary rocks based on chemical analyses. Computers and Geosciences, 17(9):1235-1253.

Crusius, J., & Thompson, J. (2000). Comparative behaviour of authigenic Re, Mo and U during reoxidation and subsequent long-term burial in marine sediments. Geochimica et Cosmochimica Acta, 64, 2233–2243.

Dalziel, I.W.D., 2006, The Making of Texas. University of Texas Institute for Geophysics Technical Report No. 234, 1p.

Dix, M., D. Spain, C. Walling, J. Sano, N. Casarta, and A. Richardson, 2010, Stratigraphy and depositional dynamics of the Hayneville-Bossier sequence: Inferences from whole-rock elemental data: AAPG, Annual Convention & Exhibition, April 11–14, New Orleans, Louisiana, 2010.

Driskill, B., Pickering, J., Rowe, H., 2018, Interpretation of High Resolution XRF data from the Bone Spring and Upper Wolfcamp, Delaware Basin, USA. 10.15530/urtec-2018-2901968.

Ellis, D.V. and Singer, J.M, 2007, Well Logging for Earth Scientists. Springer Netherlands. 708 p. (Originally published by Elsevier, 1987.

Ewing, T. E., 1991, The tectonic framework of Texas: Text to accompany "The Tectonic Map of Texas": Austin, Texas, The University of Texas at Austin, Bureau of Economic Geology, 36 p.

Ewing T.E., 2014, A new look at southern Laurentia in the Late Paleozoic; rifting of Cuyania and Sabinia, and the Ouachita 'soft closure' (abs): Geological Society of America Abstracts with Programs, Paper 146-6.

Ewing T.E., 2016, Texas through time: Lone Star geology, landscapes, and resources, The University of Texas at Austin, Bureau of Economic Geology Udden Series Number 6, 431p.

Ewing, T. E., 2019, Tectonics of the West Texas (Permian) Basin–Origins, structural geology, subsidence, and later modification, in S. C. Ruppel, ed., Anatomy of a Paleozoic basin: The Permian Basin, USA: Austin, Texas, The University of Texas at Austin, Bureau of Economic Geology Report of Investigations 285 and AAPG Memoir 118, v. 1, p. 63–96, doi:10.23867/RI0285-1.

Ewing, T. E., M. A. Barnes, and R. E. Denison, 2019, Proterozoic foundations of the Permian Basin, west Texas and southeastern NewMexico – A review, in S. C. Ruppel, ed., Anatomy of a Paleozoic basin: The Permian Basin, USA: Austin, Texas, The University of Texas at Austin, Bureau of Economic Geology Report of Investigations 285 and AAPG Memoir 118, v. 1, p. 43–61, doi:10.23867 /RI0285-1.

Fairhurst, B., Ewing, T.E., Lindsay, R., 2021, West Texas (Permian) Super Basin, United States: Tectonics, structural development, sedimentation, petroleum systems, and hydrocarbon reserves. AAPG Bulletin; 105 (6): 1099–1147. doi: https://doi.org/10.1306/03042120130

Hurd, G. S., C. Kerans, E. L. Frost, J. A. Simo, and X. Janson, in press, Sediment gravity-flow deposits and three-dimensional stratigraphic architectures of the linked Cutoff, upper Bone Spring, and upper Avalon system, Delaware Basin, (preliminary version published online Ahead of Print 20 February 2018): AAPG Bulletin, doi: 10.1306/02061817121.

Hamlin, H.S. and Baumgardner, R.W., 2012, Wolfberry (Wolfcampian-Leonardian) Deep-water depositional systems in the Midland Basin: Stratigraphy, lithofacies, reservoirs, and source rocks; University of Texas at Austin, Bureau of Economic Geology Report of Investigations No. 277, 62 p.

Hamlin, H. S., and Baumgardner, R. W., Jr., 2020, Lower Permian (Leonardian) deepwater successions in the Midland Basin: lithofacies, stratigraphy, reservoirs, and source rocks, in Ruppel, S. C., ed., Anatomy of a Paleozoic basin: the Permian Basin, USA (vol. 2, ch. 21): The University of Texas at Austin, Bureau of Economic Geology Report of Investigations 285; AAPG Memoir 118, p. 283–320.

Hatcher R.D., Jr., Thomas W., Geiser P., Snoke A., Mosher S., and Wiltschko D., 1989, Alleghanian orogen, in Hatcher R.D. Jr., Thomas W.A., and Viele G.W. (eds), The Appalachian-Ouachita Orogen in the United States, Geological Society of America, Decade of North American Geology, v F-2, p. 233–318, doi: 10 .1130 /DNAG -GNA -F2 .233.

Institute for Geophysics Jackson School of Geosciences The University of Texas at Austin 2006, Paleogeography Maps.

Jarvie, D. M., Hill, R. J., Ruble, T. E., Pallastro, R. M., 2007, Unconventional shale-gas systems: The Mississippian Barnett Shale of north-central Texas as one model for thermogenic shale-gas assessment: AAPG Bulletin, 91, no. 4, 475–499, 2007

Larson, T., 2022. Core-based machine learning characterization of Wolfcamp XY and Third Bone Spring Formation across the Delaware Basin, Texas, Bureau of Economic Geology, Webinar series 2022.

Meyers, M., Pope, M., Donovan A., 2019, Chemostratigraphy of the Woodbine and Eagle Ford Groups, Brazos Basin, Texas. Search and Discovery Article #11237

Montgomery, S., 1997, Permian Bone Spring Formation: Sandstone Play in the Delaware Basin Part ISlope, American Association of Petroleum Geologists Bulletin, V. 81, No. 8, P. 1239–1258.

Nance D.R., Linneman U., 2008, The Rheic Ocean: Origin, Evolution, and Significance. GSA Today, v. 18, no. 12, doi: 10.1130/GSATG24A.1

Nance, H. S., and Hamlin, H. S., 2020, The Bone Spring Formation (Leonardian) of the Delaware Basin: deepwater lithofacies and stratigraphy, in Ruppel, S. C., ed., Anatomy of a Paleozoic basin: the Permian Basin, USA (vol. 2, ch. 22): The University of Texas at Austin, Bureau of Economic Geology Report of Investigations 285; AAPG Memoir 118, p. 321–348.

Pearce, T. J., Beasly B. M., Wray D. S., Wright, D. K., 1999, Chemostratigraphy: a method to improve interwell correlation in barren sequences a case study using onshore, Duckmantian Stephanian sequences. Sedimentary Geology 124 (1999) 197–220.

Peng, P., Larson, T.E., A novel integrated approach for chemofacies characterization of organic-rich mudrocks. AAPG Bulletin, v. 106, no. 2 (February 2022), pp. 437–460.

Passey Q. R., Creaney S., Kulla J.B., Moretti F. J. And Strouds J. D. 1990. A Practical Model for Organic Richness from Porosity and Resistivity Logs. The American Association of Petroleum Geologists Bulletin V. 7-4, No. 12.

Pioneer Natural Resources, 2013, Investor Presentation January 2013. Accessed February 25, 2022 at https://www.sec.gov/Archives/edgar/data/1038357/000119312513004399/d462372de x991.htm.

Popova O.,2019 Permian Basin Wolfcamp and Bone Spring Shale Plays Geology review. U.S. Energy Information Administration. www.eia.gov.

Ratcliffe K.T., Wright A.M., Hallsworth C., Morton A., Zaitlin B.A., Potocki D., and Wray D.S., 2004, An example of alternative correlation techniques in a low-accommodation setting, nonmarine hydrocarbon system: the (Lower Cretaceous) Mannville Basal Quartz succession of southern Alberta, American Association of Petroleum Geologists Bulletin, v 88, no 10, pp 1419-1432.

Ratcliffe K.T., Wright A.M., and Spain D., 2012a, Unconventional methods for unconventional plays: using elemental data to understand shale resource plays, part 1, Petroleum Exploration Society of Australia (PESA) New Resources, February/March, pp 89-93.

Ratcliffe K., Wright M., and Spain D., 2012b, Unconventional methods for unconventional plays: using elemental data to understand shale resource plays, part 2, Petroleum Exploration Society of Australia (PESA) New Resources, April/May. pp 55-60.

Rickman R., Mullen, M. J., Petre, J. E., Grieser, W. V., Kundert, D., 2008, A practical use of shale petrophysics for stimulation design optimization: All shale plays are not clones of the Barnett Shale. SPE 115258, Proc. Ann. Tech. Conf., Denver, Co. September 2008.

Rowe H., 2008, Mississippian Barnett Formation, Fort Worth Basin, Texas: Bulk geochemical inferences and Mo–TOC constraints on the severity of hydrographic restriction. Chemical Geology 257 (2008) 16-25.

Ruppel, S., 2019, Introduction, Overview, and Evolution. Anatomy of a Paleozoic basin: the Permian Basin, USA (vol. 1, Ch. 1): The University of Texas at Austin, Bureau of Economic Geology Report of Investigations 285; AAPG Memoir. ISBN 9781970007404.

Schlumberger Log Interpretation Charts, 2013.

Tonner D., Swanson, A., Hollingshead, R., Hughes, S., Seacrest, S., McDaniel, B., Leeper, J., 2018, Automation Provides Unique Insights of The Rock Record and Subsurface Through the Delivery of a Robotic Sample Collection and Analysis Device. AAPG ACE 2018, Control ID Number: 2833118.

Tribovillard, N., T. Algeo, T.W. Lyons, and A. Riboulleau, 2006, Trace metals as paleoredox and paleoproductivity proxies; an update 2006: Chemical Geology, Vol. 232, Issue 1–2, p. 12–32.

Tribovillard, N., V.Bout-Roumazeilles, T. Algeo, T.W. Lyons, T. Sionneau, J.C. Montero-Serrano, A. Riboulleau, and F. Baudin, 2008. Paleodepositional conditions in the Orca Basin as inferred from organic matter and trace metal contents: Marine Geology, Vol. 254, Issue 1–2, p. 62–72.

Tribovillard, N., Algeo, T., Lyons, T.W., and Riboulleau, A., 2006, Trace metals as paleoredox and paleoproductivity proxies; an update 2006: Chemical Geology, Vol. 232, Issue 1–2, p. 12–32.

Ward, R F, Kendall, C G.S.C., and Harris, P M., 1986, Upper Permian (Guadalupian) facies and their association with hydrocarbons - Permian basin, west Texas and New Mexico. United States: N. p., Web.

Walker, W., Jobe, Z.R., Sarg, J.F., and Wood, L., 2021, Progradational slope architecture and sediment distribution in outcrops of the mixed carbonate-siliciclastic Bone Spring Formation, Permian Basin,west Texas: Geosphere, v. 17, no. 4, p. 1268– 1293,https://doi.org /10.1130 /GES02355.1.

Wang F.P., Gale, J. F., 2009, Screening criteria for shale-gas systems: GCAGS Transactions, 59, 779 – 793, 2009.

Wedepohl, K.H., 1971, Environmental influences on the chemical composition of shales and clays. In: Ahrens, L.H., Press, F., Runcorn, S.K., Urey, H.C. (Eds.), Physics and Chemistry of the Earth, vol. 8. Pergamon, Oxford, pp. 307e331.

Yang, K., Dorobek, S., 1995, The Permian basin of West Texas and New Mexico: Tectonic history of "composite" foreland basin and its effects of stratigraphic development, p. 149-174, 10.2110/pec.95.52.0149.

Appendix 1 Data Tables

Well Name	Name	XRF_QTZ %	XRF_ILL %	XRF_CAL %	XRF_DOL %	XRF_PYR %	XRF_CHL %	RSTE	BIMIN	GrainSize
Big Moose Fed Com #604H	AVALON	19	11	65	3	1	1	129	22	35
Big Moose Fed Com #604H	BSPG LIME	32	16	42	4	1	2	84	21	28
Big Moose Fed Com #604H	1ST BSPG LIME	26	9	59	3	1	1	137	14	28
Big Moose Fed Com #604H	1ST BSPG SAND	52	8	36	2	2	-	374	53	29
Big Moose Fed Com #604H	2nd BSPG LIME	42	6	46	4	1	0	263	38	26
Big Moose Fed Com #604H	2ND BSPG SAND	40	15	37	4	2	1	340	43	44
Big Moose Fed Com #604H	3rd BSPG LIME	49	22	19	5	2	3	268	49	55
Big Moose Fed Com #604H	3rd BSPG Sand	57	28	2	6	0	5	155	57	56
Big Moose Fed Com 506H	AVALON	23	13	56	5	1	1	153	26	28
Big Moose Fed Com 506H	BSPG LIME	23	13	54	6	1	1	84	13	16
Big Moose Fed Com 506H	1ST BSPG LIME	38	13	41	4	2	0	333	35	18
Big Moose Fed Com 506H	1ST BSPG SAND	45	7	44	3	1	0	300	47	15
Big Moose Fed Com 506H	2nd BSPG LIME	41	15	33	7	2	1	228	39	41
Big Moose Fed Com 506H	2ND BSPG SAND	55	27	6	6	1	3	268	55	58

Data Table Big Moose Fed Com Wells

97

Well Name	Name	XRF_QTZ %	XRF_ILL %	XRF_CAL %	XRF_DOL %	XRF_PYR %	XRF_CHL %	RSTE	BIMIN	GrainSize
Big Stagg Fed Com 503H	AVALON	20	10	63	4	1	2	277	20	28
Big Stagg Fed Com 503H	BSPG LIME	14	8	70	6	1	2	148	10	8
Big Stagg Fed Com 503H	1ST BSPG LIME	39	10	44	4	2	1	282	38	12
Big Stagg Fed Com 503H	1ST BSPG SAND	39	6	50	3	1	-	314	45	14
Big Stagg Fed Com 503H	2nd BSPG LIME	42	8	45	2	1	0	301	42	16
Big Stagg Fed Com 503H	2nd BSPG SAND	50	22	16	4	2	3	269	50	50
Big Stagg Fed Com 504H	AVALON	22	12	59	3	1	2	236	21	17
Big Stagg Fed Com 504H	BSPG LIME	35	20	34	6	1	3	335	42	40
Big Stagg Fed Com 504H	1ST BSPG LIME	31	12	50	3	2	1	178	22	6
Big Stagg Fed Com 504H	1ST BSPG SAND	42	10	43	2	2	0	376	48	15
Big Stagg Fed Com 504H	2nd BSPG LIME	45	13	35	4	1	1	224	42	39
Big Stagg Fed Com 504H	2ND BSPG SAND	55	24	9	4	1	3	140	55	55
Big Stagg Fed Com 703H	AVALON	22	7	64	4	1	1	186	24	19
Big Stagg Fed Com 703H	BSPG LIME	21	11	59	6	1	2	71	15	25
Big Stagg Fed Com 703H	1ST BSPG LIME	27	8	58	4	1	1	146	19	7
Big Stagg Fed Com 703H	1ST BSPG SAND	44	7	44	3	1	0	257	51	15
Big Stagg Fed Com 703H	2nd BSPG LIME	44	8	43	3	1	1	289	42	16
Big Stagg Fed Com 703H	2nd BSPG SAND	49	17	25	4	1	2	152	50	41
Big Stagg Fed Com 703H	3rd BSPG LIME	49	21	19	4	1	5	313	49	36

Data Tables Big Stag Wells

Well Name	Name	XRF_QTZ %	XRF_ILL %	XRF_CAL %	XRF_DOL %	XRF_PYR %	XRF_CHL %	RSTE	BIMIN	GrainSize
Toque State Com 502H	AVALON	24	15	55	3	2	1	789	31	31
Toque State Com 502H	BSPG LIME	18	10	67	2	1	1	246	13	19
Toque State Com 502H	1ST BSPG LIME	21	8	66	3	1	0	138	17	11
Toque State Com 502H	1ST BSPG SAND	39	7	49	2	2	0	222	39	28
Toque State Com 502H	2ND BSPG LIME	36	11	46	4	1	1	321	31	36
Toque State Com 502H	2ND BSPG SAND	52	24	13	6	1	3	179	52	55
Toque State Com 602H	Avalon	18	10	65	4	1	1	504	18	20
Toque State Com 602H	BSPG LIME	22	11	62	3	1	1	88	22	20
Toque State Com 602H	1ST BSPG LIME	27	12	55	4	2	0	291	27	26
Toque State Com 602H	1st BSPG SAND	44	10	41	2	2	0	314	44	23
Toque State Com 602H	2nd BSPG LIME	43	11	40	3	2	0	237	43	30
Toque State Com 602H	2nd BSPG SAND	38	18	34	5	2	2	213	38	59
Toque State Com 602H	3rd BSPG LIME	41	15	36	4	2	2	223	41	51
Toque State Com 602H	3rd BSPG SAND	57	25	5	6	0	5	223	57	70
Toque State Com #601H	Avalon	15	9	69	4	1	1	621	18	24
Toque State Com #601H	BSPG LIME	18	10	65	4	1	2	148	13	24
Toque State Com #601H	1st BSPG LIME	29	12	51	6	2	0	123	22	40
Toque State Com #601H	1st BSPG SAND	60	12	24	1	2	0	291	62	30
Toque State Com #601H	2nd BSPG LIME	37	6	53	3	1	0	139	34	40
Toque State Com #601H	2nd BSPG SAND	45	16	30	5	2	2	316	46	55
Toque State Com #601H	3rd BSPG LIME	42	16	32	5	2	3	196	41	57
Toque State Com #601H	3rd BSPG Sand	57	27	3	6	0	5	219	57	64

Data Tables Toque State wells

Well Name	Name	XRF_QTZ %	XRF_ILL %	XRF_CAL %	XRF_DOL %	XRF_PYR %	XRF_CHL %	RSTE	BIMIN	GrainSize
Big Bucks Fed Com 501H	BSPG LIME	17	10	65	5	1	1	399	31	28
Big Bucks Fed Com 501H	1ST BSPG LIME	31	11	51	4	2	1	450	31	15
Big Bucks Fed Com 501H	1ST BSPG SAND	52	10	33	3	2	0	371	55	19
Big Bucks Fed Com 501H	2nd BSPG LIME	40	8	47	3	1	0	323	39	20
Big Bucks Fed Com 501H	2nd BSPG SAND	49	24	16	5	1	3	267	49	46
Big Bucks fed Com 502H	AVALON	10	4	82	3	1	1	138	10	20
Big Bucks fed Com 502H	BSPG LIME	8	3	85	3	1	1	110	8	13
Big Bucks fed Com 502H	1ST BSPG LIME	32	6	58	3	1	0	210	32	17
Big Bucks fed Com 502H	1ST BSPG SAND	41	9	44	3	1	1	306	41	31
Big Bucks fed Com 502H	2ND BSPG LIME	40	17	35	4	1	2	348	40	46
Big Bucks fed Com 502H	2ND BSPG SAND	55	25	8	5	1	3	173	55	57

Data Tables Big Bucks wells

Well	Zone	Start	End	Gross	BIMIN	EGR	Zr/Al	RSTE
Name	Name	Depth	Depth	Interval	BIMIN	EGR	GrainSize	RSTE
		FT	FT	FT	Units	API	Units	Units
Big Bucks Fed Com 501H	BSPG LIME	8,910	9,088	178	13	46	19	103
Big Bucks Fed Com 501H	AVALON	9,088	9,192	104	31	93	28	399
Big Bucks Fed Com 501H	1ST BSPG LIME	9,192	9,346	154	31	113	15	450
Big Bucks Fed Com 501H	1ST BSPG SAND	9,346	9,553	208	55	103	19	371
Big Bucks Fed Com 501H	2nd BSPG LIME	9,553	9,992	439	39	92	20	323
Big Bucks Fed Com 501H	2nd BSPG SAND	9,992	17,025	7,033	49	84	46	267
Big Bucks fed Com 502H	BSPG LIME	8,976	9,129	153	8	85	13	110
Big Bucks fed Com 502H	AVALON	9,129	9,232	103	10	76	20	138
Big Bucks fed Com 502H	1ST BSPG LIME	9,232	9,677	446	32	71	17	210
Big Bucks fed Com 502H	1ST BSPG SAND	9,677	10,252	574	41	72	31	306
Big Bucks fed Com 502H	2ND BSPG LIME	10,252	10,747	496	40	82	46	348
Big Bucks fed Com 502H	2ND BSPG SAND	10,747	17,340	6,593	55	79	57	173
Big Moose Fed Com 506H	BSPG LIME	8,840	8,965	125	13	53	16	84
Big Moose Fed Com 506H	AVALON	8,965	9,033	69	26	68	28	153
Big Moose Fed Com 506H	1ST BSPG LIME	9,033	9,184	150	35	107	18	333
Big Moose Fed Com 506H	1ST BSPG SAND	9,184	9,607	423	47	82	15	300
Big Moose Fed Com 506H	2nd BSPG LIME	9,607	10,323	716	39	76	41	228
Big Moose Fed Com 506H	2ND BSPG SAND	10,323	17,255	6,932	55	74	58	268
Big Moose Fed Com #604H	BSPG LIME	8,810	8,948	138	21	39	28	84
Big Moose Fed Com #604H	AVALON	8,948	9,009	61	22	22	35	129
Big Moose Fed Com #604H	1ST BSPG LIME	9,009	9,163	155	14	29	28	137
Big Moose Fed Com #604H	1ST BSPG SAND	9,163	9,333	170	53	41	29	374
Big Moose Fed Com #604H	2nd BSPG LIME	9,333	9,698	365	38	23	26	263
Big Moose Fed Com #604H	2ND BSPG SAND	9,698	10,222	524	43	46	44	340
Big Moose Fed Com #604H	3rd BSPG LIME	10,222	11,366	1,144	49	79	55	268
Big Moose Fed Com #604H	3rd BSPG Sand	11,366	18,145	6,779	57	70	56	155
Big Stagg Fed Com 503H	BSPG LIME	8,860	8,990	129	10	59	8	148
Big Stagg Fed Com 503H	AVALON	8,990	9,145	156	20	73	28	277
Big Stagg Fed Com 503H	1ST BSPG LIME	9,145	9,233	88	38	87	12	282
Big Stagg Fed Com 503H	1ST BSPG SAND	9,233	9,437	204	45	81	14	314
Big Stagg Fed Com 503H	2nd BSPG LIME	9,437	9,754	317	42	80	16	301
Big Stagg Fed Com 503H	2nd BSPG SAND	9,754	17,030	7,276	50	80	50	269
Big Stagg Fed Com 504H	BSPG LIME	8,949	9,074	125	42	64	40	335
Big Stagg Fed Com 504H	AVALON	9,074	9,130	56	21	90	17	236
Big Stagg Fed Com 504H	1ST BSPG LIME	9,130	9,235	104	22	64	6	178
Big Stagg Fed Com 504H	1ST BSPG SAND	9,235	9,625	390	48	95	15	376
Big Stagg Fed Com 504H	2nd BSPG LIME	9,625	10,455	830	42	69	39	224
Big Stagg Fed Com 504H	2ND BSPG SAND	10,455	17,326	6,871	55	81	55	140
Big Stagg Fed Com 703H	BSPG LIME	8,931	9,070	139	15	83	25	71
Big Stagg Fed Com 703H	AVALON	9,070	9,169	99	24	91	19	186
Big Stagg Fed Com 703H	1ST BSPG LIME	9,169	9,259	89	19	100	7	146
Big Stagg Fed Com 703H	1ST BSPG SAND	9,259	9,508	250	51	104	15	257
Big Stagg Fed Com 703H	2nd BSPG LIME	9,508	9,845	336	42	82	16	289
Big Stagg Fed Com 703H	2nd BSPG SAND	9,845	10,296	451	50	84	41	152
Big Stagg Fed Com 703H	3rd BSPG LIME	10,296	18,028	7,732	49	95	36	313
Toque State Com 502H	BSPG LIME	8,946	9,079	132	13	44	19	246
Toque State Com 502H	AVALON	9,079	9,135	56	31	68	31	789
Toque State Com 502H	1ST BSPG LIME	9,135	9,303	168	17	24	11	138
Toque State Com 502H	1ST BSPG SAND	9,303	9,736	433	39	18	28	222
Toque State Com 502H	2ND BSPG LIME	9,736	9,974	238	31	28	36	321
Toque State Com 502H	2ND BSPG SAND	9,974	17,765	7,791	52	58	55	179
Toque State Com #601H	BSPG Lime	8,888	9,008	120	13	28	24	148
Toque State Com #601H	Avalon	9,008	9,112	104	18	22	24	621
Toque State Com #601H	1st BSPG LIME	9,112	9,231	119	22	34	40	123
Toque State Com #601H	1st BSPG SAND	9,231	9,563	332	62	44	30	291
Toque State Com #601H	2nd BSPG LIME	9,563	9,884	322	34	13	40	139
Toque State Com #601H	2nd BSPG SAND	9,884	10,464	579	46	48	55	316
Toque State Com #601H	3rd BSPG LIME	10,464	11,170	706	41	47	57	196
Toque State Com #601H	3rd BSPG Sand	11,170	19,132	7,962	57	71	64	219
Toque State Com 602H	BSPG Lime	8,895	9,066	170	22	16	20	88
Toque State Com 602H	Avalon	9,066	9,218	152	18	35	20	504
Toque State Com 602H	1ST BSPG LIME	9,218	9,263	45	27	15	26	291
Toque State Com 602H	1st BSPG SAND	9,263	9,496	233	44	39	23	314
Toque State Com 602H	2nd BSPG LIME	9,496	9,910	414	43	21	30	237
Toque State Com 602H	2nd BSPG SAND	9,910	10,162	252	38	56	59	213
Toque State Com 602H	3rd BSPG LIME	10,162	11,192	1,030	41	50	51	223
Toque State Com 602H	3rd BSPG SAND	11,192	19,179	7,987	57	56	70	223

Data Tables of Average BI, EGR, Zr/Al and RSTE's for all wells in the study area.

BSPG LIME		EGR	GR
BSPG LIME	Big Bucks Fed Com 501H	46	63
BSPG LIME	Big Bucks fed Com 502H	80	45
BSPG LIME	Big Moose Fed Com 506H	43	42
BSPG LIME	Big Moose Fed Com #604H	25	42
BSPG LIME	Big Stagg Fed Com 503H	53	41
BSPG LIME	Big Stagg Fed Com 504H	64	39
BSPG LIME	Big Stagg Fed Com 703H	81	44
BSPG LIME	Toque State Com 502H	19	39
BSPG Lime	Toque State Com #601H	18	42
BSPG Lime	Toque State Com 602H	16	42
Average		45	44

1ST BSPG LIME		EGR	GR
1ST BSPG LIME	Big Bucks Fed Com 501H	113	68
1ST BSPG LIME	Big Bucks fed Com 502H	67	66
1ST BSPG LIME	Big Moose Fed Com 506H	106	55
1ST BSPG LIME	Big Moose Fed Com #604H	20	54
1ST BSPG LIME	Big Stagg Fed Com 503H	82	67
1ST BSPG LIME	Big Stagg Fed Com 504H	64	58
1ST BSPG LIME	Big Stagg Fed Com 703H	34	43
1ST BSPG LIME	Toque State Com 502H	20	58
1ST BSPG LIME	Toque State Com #601H	17	48
1ST BSPG LIME	Toque State Com 602H	15	44
Average		60	56

2nd BSPG Lime		EGR	GR
2nd BSPG Lime	Big Bucks Fed Com 501H	92	66
2nd BSPG Lime	Big Bucks fed Com 502H	78	78
2nd BSPG Lime	Big Moose Fed Com 506H	71	64
2nd BSPG Lime	Big Moose Fed Com #604H	19	46
2nd BSPG Lime	Big Stagg Fed Com 503H	76	44
2nd BSPG Lime	Big Stagg Fed Com 504H	69	69
2nd BSPG Lime	Big Stagg Fed Com 703H	75	47
2nd BSPG Lime	Toque State Com 502H	23	69
2nd BSPG Lime	Toque State Com #601H	12	40
2nd BSPG Lime	Toque State Com 602H	21	39
Average		54	56

3rd BSPG Lime		EGR	GR
3rd BSPG Lime	Big Bucks Fed Com 501H		
3rd BSPG Lime	Big Bucks fed Com 502H		
3rd BSPG Lime	Big Moose Fed Com 506H		
3rd BSPG Lime	Big Moose Fed Com #604H	75	75
3rd BSPG Lime	Big Stagg Fed Com 503H		
3rd BSPG Lime	Big Stagg Fed Com 504H		
3rd BSPG Lime	Big Stagg Fed Com 703H	93	105
3rd BSPG Lime	Toque State Com 502H		
3rd BSPG Lime	Toque State Com #601H	41	66
3rd BSPG Lime	Toque State Com 602H		
Average		70	82

AVALON		EGR	GR
AVALON	Big Bucks Fed Com 501H	93	32
AVALON	Big Bucks fed Com 502H	71	90
AVALON	Big Moose Fed Com 506H	44	80
AVALON	Big Moose Fed Com #604H	20	83
AVALON	Big Stagg Fed Com 503H	71	88
AVALON	Big Stagg Fed Com 504H	90	88
AVALON	Big Stagg Fed Com 703H	83	88
AVALON	Toque State Com 502H	52	85
AVALON	Toque State Com #601H	19	71
AVALON	Toque State Com 602H	35	54
Average		53	80

1st BSPG Sand		EGR	GR
1st BSPG Sand	Big Bucks Fed Com 501H	103	73
1st BSPG Sand	Big Bucks fed Com 502H	67	69
1st BSPG Sand	Big Moose Fed Com 506H	77	53
1st BSPG Sand	Big Moose Fed Com #604H	26	66
1st BSPG Sand	Big Stagg Fed Com 503H	78	82
1st BSPG Sand	Big Stagg Fed Com 504H	95	66
1st BSPG Sand	Big Stagg Fed Com 703H	100	72
1st BSPG Sand	Toque State Com 502H	17	66
1st BSPG Sand	Toque State Com #601H	40	57
1st BSPG Sand	Toque State Com 602H	39	49
Average		64	63

2nd BSPG Sand		EGR	GR
2nd BSPG Sand	Big Bucks Fed Com 501H	84	99
2nd BSPG Sand	Big Bucks fed Com 502H	78	89
2nd BSPG Sand	Big Moose Fed Com 506H	73	57
2nd BSPG Sand	Big Moose Fed Com #604H	38	74
2nd BSPG Sand	Big Stagg Fed Com 503H	79	94
2nd BSPG Sand	Big Stagg Fed Com 504H	81	90
2nd BSPG Sand	Big Stagg Fed Com 703H	80	72
2nd BSPG Sand	Toque State Com 502H	56	89
2nd BSPG Sand	Toque State Com #601H	42	64
2nd BSPG Sand	Toque State Com 602H	56	55
Average		67	78

3rd BSPG Sand		EGR	GR
3rd BSPG Sand	Big Bucks Fed Com 501H		
3rd BSPG Sand	Big Bucks fed Com 502H		
3rd BSPG Sand	Big Moose Fed Com 506H		
3rd BSPG Sand	Big Moose Fed Com #604H	70	66
3rd BSPG Sand	Big Stagg Fed Com 503H		
3rd BSPG Sand	Big Stagg Fed Com 504H		
3rd BSPG Sand	Big Stagg Fed Com 703H		
3rd BSPG Sand	Toque State Com 502H		
3rd BSPG Sand	Toque State Com #601H	71	76
3rd BSPG Sand	Toque State Com 602H		
Average		70	71

Data Tables of Average GR and EGR for all wells

10. VITA

After completing his work at Liverpool College in 1986, David Tonner entered Nottingham University, Nottingham, England, UK. in 1989 where he received the degree of Bachelor of Science in Geology. From 1989 to present David has held several positions within the Oilfield services sector applying Geological sciences. In 2020 he entered the Graduate School of Stephen F. Austin State University at Nacogdoches, Texas. and received the degree of Master of Science in in Geology in August 2022.

Permanent Address: 3 Clare Point Dr,

Magnolia TX 77354

Style Manual Designation: American Association of Petroleum Geologists

This thesis was typed by David J.Tonner.